Time Variations of X-rays from Cygnus X-1 and Implications for the Accretion Process

by Hitoshi Negoro

Abstract

Short-term X-ray variability of the prime stellar black hole candidate, Cygnus X-1, in its low intensity state is studied using data obtained on 1987 Aug 5–6 and 1990 May 9–11 with the large area proportional counter on board the *Ginga* satellite. Average properties of X-ray shots, or flare-like events characterizing the aperiodic X-ray time variability, were obtained by superposing a number of the X-ray shots through aligning their peaks.

Average time profiles of the shots show time symmetric rise and decay, each of which is roughly represented by a sum of two exponentials with time constants of about 0.13 and 1.2 sec in 1987, and 0.08 and 0.7 sec in 1990. The rise profiles are also roughly described by a function proportional to $1/(\tau - t)^{\alpha}$, where t (< 0) is the time relative to the intensity maximum, $\tau \sim 0.05$ sec in 1987 and 0.03 sec in 1990, and $\alpha \sim 0.7$ in both 1987 and 1990. The rise profiles are stable on time scales of a few hours, and independent of the peak intensities. The decay profiles are, however, changeable on time scales of a few hours and a day, and slightly depend on the peak intensities. The shots have a small bump-like structure near the beginning, and slight decreases in intensity both before and after each event. These decreases are related to a non-random temporal distribution of the shots. These features well explain observed time-averaged power spectra below ~ 1 Hz.

Hardness ratios of the shots before the peak intensity are softer than time averaged ratios. The ratios suddenly harden at the peak intensity, and continue hardening with the intensity decrease, but always remain slightly softer than or equal to the average ratios. The energy spectrum of the shots can be represented by a Comptonized blackbody plus power law model. Each of the components dominates the spectrum before and after the peak intensity, respectively. In addition, the existence of another hard spectral component is suggested from the softness of the energy spectrum of the shots and from the high-frequency excess seen in the power spectral densities above ~ 1 Hz. The soft energy spectrum of the shots explains the soft excess component observed at energies below a few keV from the power-law energy spectrum. This component can be interpreted as the emission from an optically thick accretion disk. The multi-component energy spectrum slightly reproduces the edge-like structure at energies 7–20 keV and the hard bump at higher energies.

The independence of the shot profile from its peak intensity rules out previous shot-occurrence models based on disk instabilities and/or magnetic field reconnections, and implies that the shots arise from density fluctuations of accretion matter drifting onto a black hole.

Contents

Chapter 1

Introduction

It has been confirmed from optical and radio observations that the masses of some stellar black hole candidates (SBHCs) are in excess of the maximum mass of the neutron star (~ 3 $M_\odot$), and that central densities of massive black hole candidates (MBHCs), active galactic nuclei (AGNs), are larger than those expected from a cluster of normal stars. However, observational evidence for the presence of black holes was yet to be found. X-rays observed from these BHCs must have some information on central compact objects, probably black holes, because they are emitted in the nearest regions to the objects. That is why, a number of observational and theoretical studies have been devoted to understanding those X-ray properties and the relation to the black holes.

SBHCs are collapsed, dense compact stars to which material accretes from a companion star. The accreting gas forms an accretion disk around the compact star, and an inner portion of the accretion disk emits X-rays by releasing gravitational energy of the accreting gas. Continuous observational studies of many X-ray binaries have revealed that some properties of X-ray time variations and energy spectra of SBHCs are common to all the SBHCs and different from those of neutron stars or white dwarfs.

SBHCs show at least two distinct states, high and low intensity (or soft and hard spectral) states. The energy spectrum in the high state is represented by a superposition of an ultra-soft thermal spectrum and a power-law spectrum. The thermal spectrum is understood as an optically thick accretion disk component, and time variability of this component is considerably low. On the other hand, the origin of the power-law component is unknown, and this component exhibits relatively large time variations.

A famous SBHC in our Galaxy, Cygnus X-1, is usually in the low state. Observed X-rays in this state exhibit a power-law energy spectrum and highly aperiodic time variability on time

scales of a few hundred seconds down to milliseconds. The power law energy spectrum has been thought to result from the unsaturated Comptonization of low energy photons. The emitting region and detailed process are, however, still open to question. Furthermore, few observational properties of the highly aperiodic time variability have been interpreted by theoretical models quantitatively.

Recent intensive observations of Seyfert galaxies, a kind of AGNs, have revealed that their X-ray properties are very similar to those of the SBHCs in the low states. This is not surprising matter because all the physical parameters can be scaled by the Schwarzshild radius ($r_s = 2GM/c^2$ where M is the mass of a central object.), and most of the physical properties should be the same if a (non-rotating) black hole is present at the center.

Thus, our understanding of black holes much progresses especially in taxonomy, but fundamental questions still remain: Why does X-ray intensity exhibit so highly aperiodic variations ? Where do X-rays come from ? What is the relationship between these X-ray properties and black holes ? Massive objects undoubtedly exist in the center of BHCs as shown from the recent observations. But do black holes we suppose really exist there ?

In this thesis, to understand X-ray properties of the BHCs in the low states in detail and to know physical situation around black holes, X-ray temporal and spectral variations in the well-known SBHC, Cyg X-1, in the low state are studied using data obtained in 1987 Aug 5–6 and in 1990 May 9–11 with the large area proportional counter (LAC) on board the *Ginga* satellite. The data obtained in the two separated observations will provide intrinsic and transient X-ray properties of this source.

A new analysis method, a superposition of X-ray shots, is introduced and mainly used in this thesis to obtain average properties of the X-ray shots. The X-ray shots are flare or burst-like events, and have been believed to be a typical time variation in the aperiodic time variations in the low state. This analysis method conserves information on amplitude and phase components of the power spectrum simultaneously, and represents true features of the X-ray shots except some systematic errors.

In chapter 2, observational properties of black holes candidates and related theoretical models are reviewed. Instruments of the *Ginga* satellite, with which the data were obtained, are summarized in chapter 3. Observations and data reductions are shown in chapter 4. In chapter 5, the method of the superposition of the X-ray shots and the systematic errors are presented. Shot properties obtained by the superposition method are fully described in chapter 6. In chapter 7, the obtained properties are examined in comparison with results of other

timing analyses. The amount of the X-ray shots to the total X-rays is estimated in chapter 8. In chapter 9, observed time averaged spectra are investigated using the results in previous chapters. Finally, the obtained properties are compared with previous reports of timing and energy spectral analyses, and physical interpretations on the X-ray shots and disk geometry are discussed in chapter 10.

Chapter 2

Review

In this chapter, previous observational and theoretical works for black hole candidates are reviewed. The first aim of this chapter is to show present observational evidence for the presence of black holes. The second one is to describe observational properties of stellar and massive black hole candidates and interpretations on them, and to explain the reason why Cygnus X-1 should be still studied.

2.1 Cygnus X-1 & Black Holes

The black holes[1] are characterized by the event horizon[2], which is defined by the Schwarzschild radius r_s,

$$r_s = \frac{2GM}{c^2} \tag{2.1}$$

where G ($= 6.67 \times 10^{-8}$ dyn cm^2 g^{-2}) is the gravitational constant, M is the mass of a black hole, and c ($= 2.998 \times 10^{10}$ cm s^{-1}) is the velocity of light. Even light can not escape from the inside of this radius due to the distortion of the spacetime geometry. Furthermore, for a distant observer, it takes infinite time for matter falling to a black hole to reach the surface of the black hole (the event horizon) (e.g., Shapiro & Teukolsky 1983). Thus, it is very difficult to find black holes observationally.

In the early of 1970s, a strange X-ray star was found which exhibited rapid time variations in X-ray intensity (Oda et al. 1971). This was Cygnus X-1 (for excellent reviews, Oda 1977; Liang & Nolan 1984, hereafter LN, and references therein). Continuous multiwave observations after this discovery revealed that Cyg X-1 was a binary system with a blue supergiant star, HDE226868, and that the orbital period was 5.6 day and the inclination angle was 27°. From

[1] Here, non-rotating (Schwarzschild) black holes are considered (c.f., Shapiro & Teukolsky 1983).
[2] For the event horizon, see Hawking (1973).

the mass of the heavy supergiant star and the binary orbital period, the mass of Cyg X-1 was estimated to be more than 3 $M_\odot$, the theoretical maximum mass of a nuetron star, probably 9–15 $M_\odot$ (Bolton 1975; Avni & Bahcall 1975). Furthermore, rapid X-ray time variations on time scales of milliseconds provided the maximum size of the emission region ($c\Delta t \sim$) 10^7–10^8 cm. To the best of our current knowledge, such a compact and heavy star can not be understood except for a black hole. From these facts, it has been widely believed that Cyg X-1 is a good black hole candidate.

Here, one question may arise. How does a black hole emit X-rays ? Lynden-Bell (1969) first pointed out that not a black hole, but accretion gas emitted electro-magnetic waves by forming an accretion disk around the black hole. Recent HST (Hupple Space Telescope) observations of M 87 (Harmes et al. 1994) and VLBA (Very Long Baseline Array) observations of M 106 (NGC 4258) (Miyoshi et al. 1995) found gases rotating near the central massive objects. From gas velocities and distances from the central objects, the central densities were found to be too dense (10^6 $M_\odot$ pc^{-3} in M 87, and $> 4 \times 10^9$ $M_\odot$ pc^{-3} in M 106) to be understood as a cluster of normal stars. They concluded that massive black holes were present at the centers.

However, to confirm the presence of the black holes we suppose and to know their physical properties, we must know physical properties of the accretion disks. There is an important radius characterizing the accretion disks, $3r_s$. Matter can not proceed Kepler (circular) motion within the radius $3r_s$ due to the strong gravitational force exceeding the inertial force (e.g., Shapiro & Teukolsky 1983), so that the accretion disk is formed at radii larger than $3r_s$. Accreting matter out of the radius transfers its gravitational energy to radiation by energy dissipation due to the viscosity. On the other hand, very little photons are expected to be radiated from inside of this radius since the matter falls onto a black hole just like a free fall (e.g., Stoeger 1980).

Thus, firm observational evidence for the presence of the black holes is to show that matter passing through the innermost radius of the accretion disk dose not emit photons. Till then, all the heavy or dense compact objects with masses over the maximum mass of the neutron star are called “black hole candidates (BHCs)”, not “black holes”.

2.1.1 Black Hole Candidates

There are several X-ray stars of which masses are found to be over the maximum mass of the neutron star. These are undoubted (S-)BHCs. There are another several stars in which X-ray properties quite resemble those in the mass-estimated BHCs, but masses of them are unknown. Those X-ray stars are also called BHCs since the X-ray properties of the BHCs are

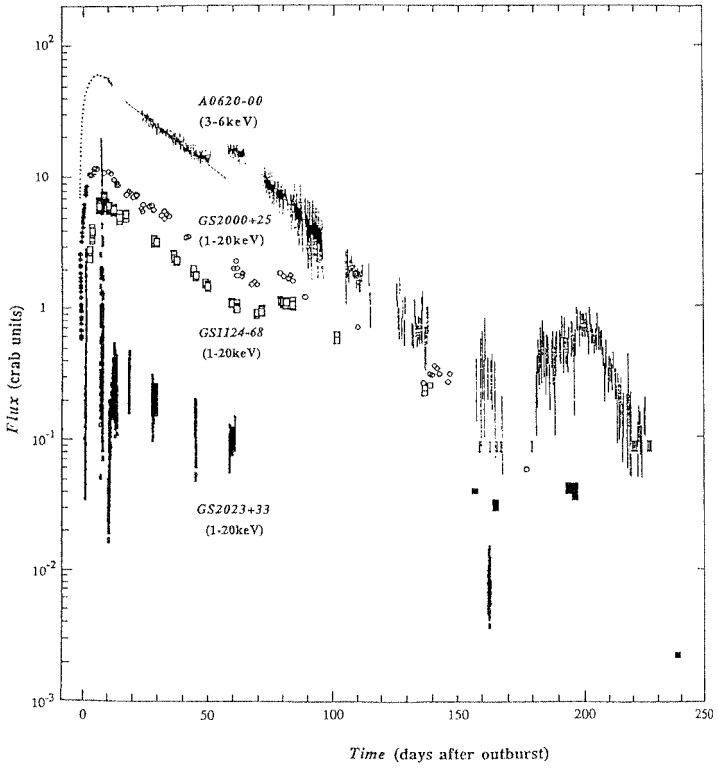

Figure 2.1: X-ray light curves of several X-ray novae (from Inoue 1993).

quite different from those of neutron stars; pulsars and low-mass-X-ray-binary (LMXB) neutron stars with some exceptions (Tanaka 1989; White 1989). These BHCs and their X-ray properties are summarized in Table 2.1 and 2.2. (For excellent reviews for BHCs, Tanaka 1992; Inoue 1992)

One of the characteristic features of BHCs is bimodal behavior in the X-ray properties; "high" and "low" intensity states. The high state is characterized by a ultra-soft thermal component and a hard power-law tail as shown in Fig. 2.2. While, the energy spectrum in the low state is roughly represented by a power law spectrum with a photon index 1.5–1.8, and X-ray intensity exhibits highly aperiodic time variations on time scales of a few hundred seconds to milliseconds.

The nature of the transition between these states has been in mystery, and though to be due to an accretion rate (e.g., Throne & Price 1975; Galeev, Rosner, & Vaiana 1979; Inoue & Hoshi 1987; Hoshi & Inoue 1988). Continuous *Ginga* observations of X-ray novae (Fig. 2.1), however, revealed complex features of the transition.

Table 2.1:
LIST OF BLACK HOLE CANDIDATES[a]

Name	Mass	Comment	Reference[b]
Cgynus X-1	9.5 $M_\odot$	Hard/Soft	(1,2)
A 0620-00	> 3.2 $M_\odot$	Nova, Soft	(3)
LMC X-3	7 $M_\odot$	Soft	(4)
LMC X-1	2.6 $M_\odot$	Soft	(5)
SS 433	> 4.3 $M_\odot$	Thermal, Relativistic Jet	(6)
GS 2023+338 (V404 Cyg)	> 6 $M_\odot$	Nova, Hard	(7,8)
GS 1124-683 (Nova Musca)	> 3.1 $M_\odot$	Nova, Soft/Hard	(9,10)
4U 1543-47		Nova, Soft	(11)
GX 339-4		Hard/Soft	(12, 13)
GS 2000+25		Nova, Soft/Hard	(14,15)
GS 1354-64		Nova, Soft	(16)
GS 1826-24		Nova, Hard	(17)
GS 1734-275		Nova, Soft	(18)
1E 1740.7-2942		Hard	(19)

a. From Kitamoto 1993, Tanaka 1989
b. (1) Oda (1977) (2) Liang & Nolan (1984) (3) McClintock & Remilard (1986) (4) Cowly et al. (1983) (5) Hutching et al. (1983) (6) Leibwitz (1984) (7) Kitamoto et al. (1989b) (8) Casares et al. (1992) (9) Kitamoto et al. (1992) (10) Remillard, R. A. et al. (1992) (11) Kitamoto et al. (1984) (12) Makishima et al. (1986) (13) Miyamoto et al. (1991) (14) Tsunemi et al. (1989b) (15) Terada (1994) (16) Kitamoto et al. (1990) (17) Tanaka (1989) (18) Makino et al. (1988) (19) Sunyaev et al. (1990)

Table 2.2:
X-RAY PROPERTIES OF COMPACT OBJECTS

	Black Hole Candidates		Neutron Stars		White Dwarfs
			X-ray Pulsars	LMXBs	(CVs)
	(Soft State)	(Hard State)			
Energy Spectrum[a]	DBB (0.3–1 keV) + PL (2.1–3)	PL (1.5–1.8)	PL (0–0.5)[b]	DBB (1–1.5 keV) + BB ($\sim$ 2 keV)	Thermal Brems. ($\sim$ 20 keV)
Time Variations[c]	Quiet (1/f) + Rapid Var.	Flickering	Pulsation	Quiet (1/f) + Rapid Var.	Cataclysmic (Pulsation)
Remarks	QPO			Burster, QPO	

a. DBB = disk blackbody (disk temperature in keV), BB = blackbody (blackbody temperature in keV), PL = power law (photon index)
b. The power law has an exponential cut off around 20 keV.
c. Comparisons at Fourier frequencies 0.1–10 Hz (see text).

In fact, two X-ray novae, GS 2000+25 and GS 1124-684, discovered by the ASM on board *Ginga* (GS 2000+25, Tsunemi et al. 1989b; GS 1124-684, Kitamoto et al. 1992), had remained in the high states until the intensities decreased to about 1/100 of the maxima, and transited to the low states (Miyamoto et al. 1993, 1994; Terada 1994). While, GS 2023+338 was always in the low state even near the maximum intensity (Kitamoto et al. 1989b; Tanaka 1989; in't Zand et al. 1992).

Taking account of these facts, the low state has also been called the "hard" spectral state, and the high state is the "soft" spectral state (Tanaka 1989). Recently, Miyamoto et al. (1995) also pointed out a hysteresis of the transition between these two states; in GX 339-4 and Cyg X-1, the transitions from the (power law) hard to (power law) soft states occurred just before the maximum intensities. Thus, the terms, "hard state" and "soft state", are mainly used in this thesis. However, for Cyg X-1, the hard spectral state has been called the low state so long that the term, "low state", is used.

2.2 Soft State

2.2.1 Energy Spectrum

The ultra-soft thermal component in the soft state is well represented by a disk blackbody spectrum (Mitsuda et al. 1984), which is a model spectrum expected from an optically thick accretion disk. According to the accretion disk theory (Shakura & Sunyaev 1993; Novikov & Thorne 1973), the local effective temperature of the optically thick disk, $T_e(r)$, is represented by

$$T_e(r) = \left\{ \frac{3GM\dot{m}}{8\pi\sigma r^3} \left(1 - \sqrt{\frac{r_0}{r}} \right) \right\}^{1/4}, \tag{2.2}$$

where σ is the Sephan-Boltzmann constant, $\dot{m}$ is the accretion rate, and r_0 is the radius of the inner boundary of the accretion disk. Then, the observed spectrum from the disk at radius from r_{in} to r_{out} can be shown as follows.

$$\begin{aligned} F(E) &= \frac{cos\theta}{D^2} \int_{r_{in}}^{r_{out}} 2\pi B(E, T(r)) dr \\ &\simeq \frac{8\pi r_{in}^2 cos\theta}{3D^2} \int_{T(r_{out})}^{T(r_{in})} \left(\frac{T}{T(r_{in})} \right)^{-3/11} B(E,T) \frac{dT}{T(r_{in})}, \end{aligned} \tag{2.3}$$

where D is the distance to the source, θ is the inclination angle, and $B(E,T)$ is the Planck function. In the above approximation, the term $(r_0/r)^{1/2}$ in Eq. (2.2) is ignored. Since $T(r_{out}) \ll$

$T(r_{in})$ for $r_{out} \gg r_{in}$, one can find from the above equation that the spectrum can be expressed by only the inner radius of the disk and the temperature at that radius.

Makishima et al. (1986) found in GX 339-4 spectra (Fig. 2.2) that the inner radii of the disk blackbody model were almost constant in spite of large variations in the other fitting parameters, and explained it in terms of the innermost radius of the accretion disk around a black hole. They also noted that obtained temperatures of this component were lower than those in LMXBs, which supported their interpretation because we found $T_e \propto M^{-1/4}$ from $r, \dot{m} \propto M$ in Eq. (2.2) (cf., Eq. (10.1)). From fits to spectra of LMC X-3, LMC X-1, GS 2000+25, and GX 339-4 with a modified disk blackbody model taking account of relativistic effects, Ebisawa (1991) interpreted obtained inner radii of that component to be $3r_s$, and showed that masses of these BHCs were systematically larger than those of LMXBs, and in excess of 3 $M_\odot$. While, the origin of the power law spectral component is unknown at all.

2.2.2 Time Variation

X-ray intensities of the disk (thermal) and power-law components in the soft state vary independently on time scales of days and months (e.g., GX 339-4, Makishima et al. 1986; Miyamoto et al. 1991; GS 1124-683, Miyamoto et al. 1993).

To investigate relative amplitudes of short-term variations of these components, a normalized power spectral density (NPSD) has been introduced, which is defined as the square of the Fourier amplitude (a_f^2) Hz^{-1} divided by that of the average source intensity (a_0^2) (e.g., Miyamoto et al. 1991).

Miyamoto et al. (1993) and Terada (1994) found in time variations of GS 1124-683, GX 339-4, and GS 2000+23 that when the disk components dominated over the power law components, NPSDs of the BHCs showed 1/f–like spectra as indicated by the circles with errors in Fig. 2.3. On the other hand, when the power law energy spectral components was dominant, NPSDs became flat-top spectra (shown by points with errors in Fig. 2.3).

Miyamoto et al. (1993) also pointed out that these NPSD were similar to those of a LMXB source, GX 5-1, not only in shape but also in its relative (squared) amplitude (right panel in Fig. 2.3). In both the PSDs, quasi-periodic oscillations (QPOs) were also observed (Dotani 1988).

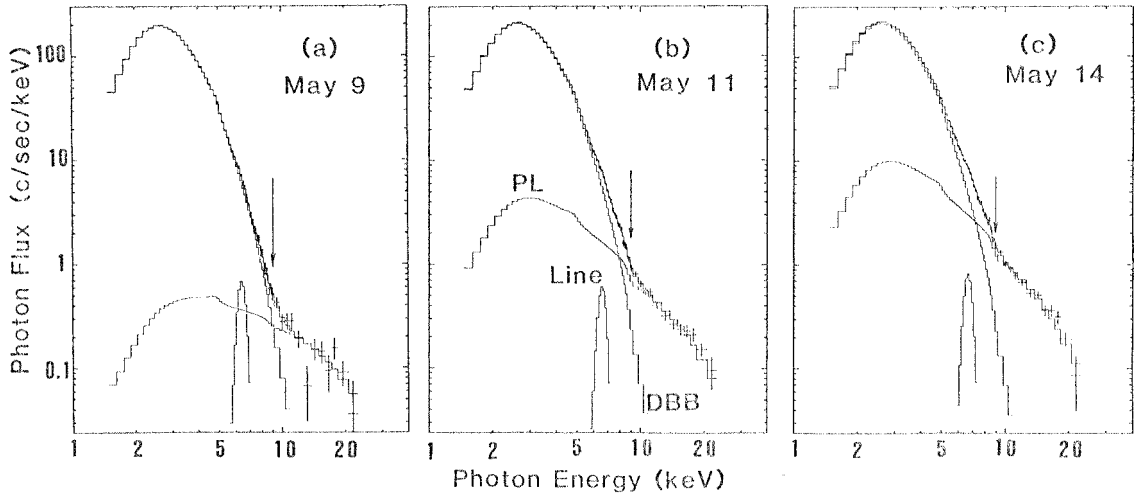

Figure 2.2: Energy spectra of GX 339-4 in the soft spectral (high intensity) state. The disk blackbody component and the power law component are also shown by the solid lines (from Makishima et al. 1986).

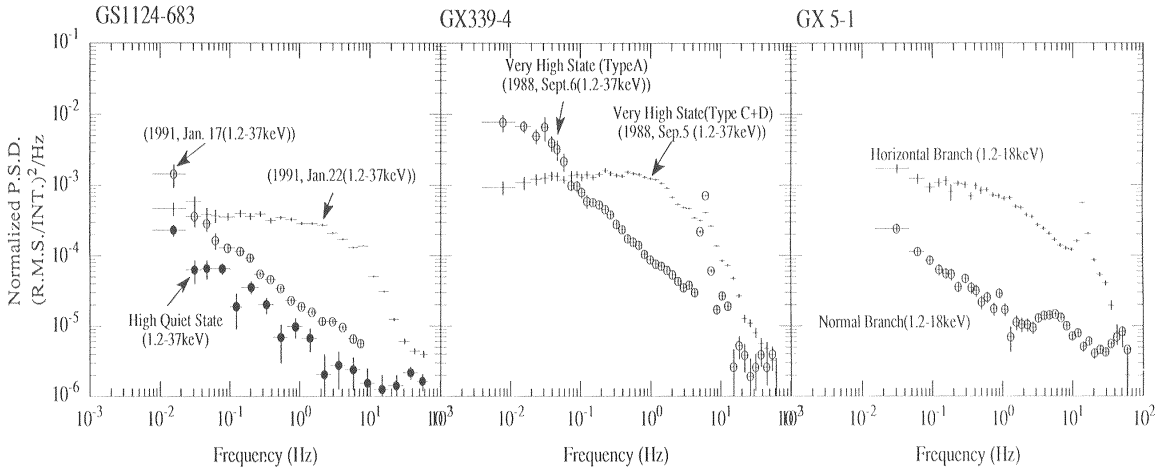

Figure 2.3: Normalized power spectral densities of GS 1124-68, GX 339-4 in the soft states and a LMXB source, GX 5-1. see text (from Miyamoto et al. 1993).

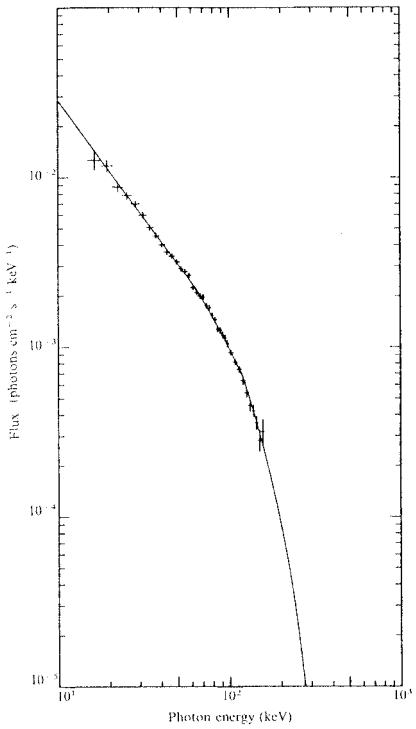

Figure 2.4: An observed energy spectrum of Cyg X-1 in the low state. The best-fitting Comptonization model is also indicated by the solid line. (from Sunyaev & Trumper 1979)

2.3 Hard State

2.3.1 Energy Spectrum

Power Law Continuum

Energy spectra of the SBHCs in the hard states are roughly represented by a single power law in the 1–100 keV range. Photon indices of the power-law spectra are 1.5–1.7 (Tanaka 1989). The spectra fall off steeply at the higher energies (e.g., LN). The γ-ray spectra reach to a few hundreds keV (e.g., Cyg X-1, Ling et al. 1987; Sunyaev et al. 1990; GX 339-4, Harmon et al. 1992; GS 1124-68, Sunyaev et al. 1992), and sometimes show γ-ray bump around 1 MeV (Cyg X-1, Ling et al. 1987) or around 500 keV suggesting a electron-positron annihilation feature (1E1740.7-2942, Sunyaev et al. 1992).

AGNs also show similar power-law energy spectra with similar photon indices to SBHCs, and called the "canonical" power-law spectra (Turner & Pounds 1989; Kruper, Urry, & Canizares 1990). Thus, the canonical power-law spectrum is common to all the SBHCs and MBHCs.

The power-law energy spectrum can be produced by nonthermal bremsstrahlung or synchrotron radiation by electrons with a power-law energy distribution (Rybicki & Lightman 1979), unsaturated Compton scattering, and other nonthermal processes (e.g., magnetic reconnections). Taking account of cooling times and radiative efficiencies of these radiative processes, the unsaturated Compton scattering process is most likely to produce the observed power law spectra (e.g., LN). In the unsaturated Compton scattering models (Eardley, Lightman, & Shapiro 1975; Shapiro, Lightman, & Eardley 1976; Sunyaev & Trumper 1979; Sunyaev & Titarchuk 1980; Nishimura, Mitsuda, & Ito 1986), low energy ($h\nu \ll m_e c^2$) photons gain energy through inverse Compton scattering off hot ($\sim$ 30–150 keV) electrons, and escape from the electron cloud by diffusion. The resultant energy spectrum well represents the observed spectra (e.g., Fig. 2.4). In this model, the hard X-ray cut off in the observed spectra is understood as a thermal cutoff due to the electron temperature.

A Comptonized blackbody model (Nishimura, Mitsuda, & Ito 1986) used in this thesis is different from a Sunyaev & Titarchuk's model often used in previous papers. In the former model, relatively thin ($\tau \lesssim 3$ where τ is Tomson optical depth.) electron cloud is considered. That is why, an initial energy distribution of input soft photons plays an important role. In their model, a blackbody spectrum is assumed as an input soft photon spectrum. The model spectra are shown in Fig. 2.5. The approximate spectral formula of this model at $E \lesssim kT_e$ ($\lesssim 150$ keV) can be obtained by Monte Carlo simulations.

A disk temperature in the standard α disk model by Shakura & Sunyaev (1973) is too cold ($\lesssim$ 1 keV) to explain the observed spectra. (That is why, the standard disk is often called "cold disk".) There are two kinds of disks to have a hot electron region to emit the power law spectrum. Shapiro et al. (1976) considered a two-temperature region in the inner region of an accretion disk (left panel of Fig. 2.6), where the disk became optically thin and geometrically thick ($h/r \sim 1$ where h and r were a half disk thickness and radial distance from the center of the source, respectively.), and the ion temperature T_i exceeded the electron temperature T_e ($T_i \sim 10^{11}$ K, $T_e \sim 10^9$ K). One of unsolved problems of this model is the origin of the copious supply of soft photons (LN).

A coronal disk model is free from the problem in the two-temperature disk model (Liang & Price 1977). In the coronal model, optically thin, hot corona analogous to the solar one is formed above and below a cold disk as shown in the right panel of Fig. 2.6, and soft photons from the cold disk are scattered in the coronal region. The model uncertainty is the formation of the hot coronal region. A possible mechanism to form the corona is a disk wind due to magnetic

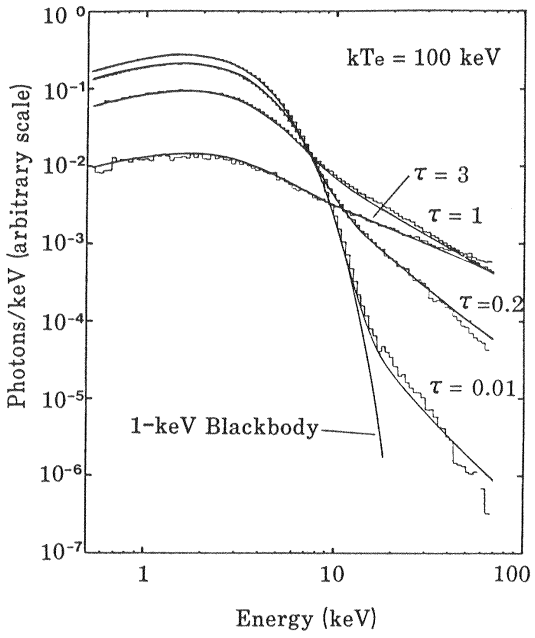

Figure 2.5: Comptonized blackbody model spectra used in this thesis. Approximate analytic solutions and results of Monte Carlo simulations for various optical depths are shown by the solid lines and the step functions, respectively (from Nishimura et al. 1986).

flares on the disk, which is also an analogy of the solar flares.

However, observed power-law spectra are not so simple because of a few remarkable structures; a soft excess component below a few keV, an iron line feature around 6.4 keV, a broad edge-like structure at energies 7–20 keV and a hard X-ray excess at higher energies. In the following paragraphs, these properties will be described.

Soft Excess

If the energy spectrum of Cyg X-1 is fitted with a power law with an interstellar absorption model, the column density of the interstellar absorption shows a much smaller value than that in Optical/UV measurements. This is thought to be due to a soft excess component. Such a soft excess component above the power law continuum at energies below a few keV has been reported from many observations (Priedhorsky et al. 1979; Balucińska & Chlebowski 1988 (*Einstein*/MPC); Barr & van der Woerd 1990 (*EXOSAT*/TGS,GSPC); Balucińska & Hasinger 1991 (*EXOSAT*/ME)). The soft excess component has been represented by a steep power law with

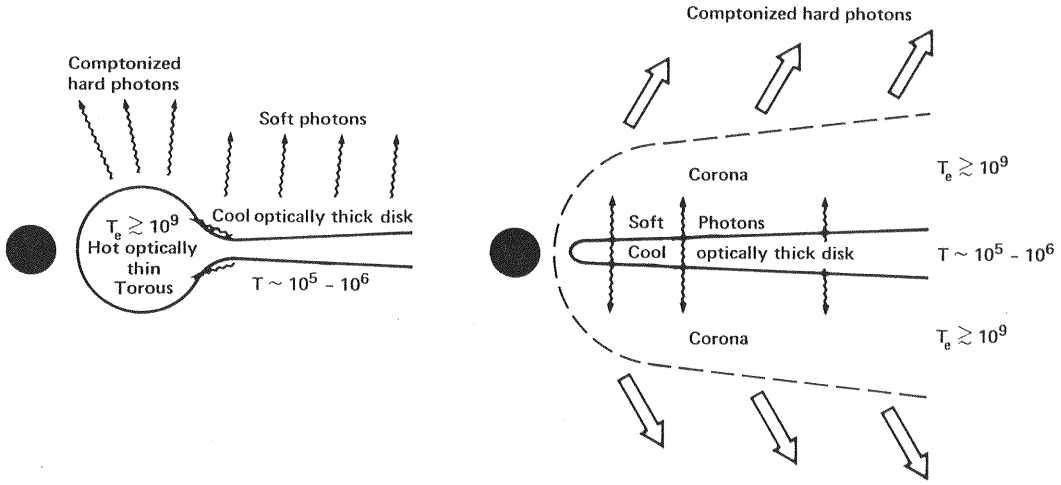

Figure 2.6: Schematic drawings of the two-temperature disk model (*left*) and the coronal disk model (*right*). Soft photons are scattered in the inner portion of the accretion disk in the former model, or above and below the disk in the latter (from Liang & Nolan 1984).

a photon index $\alpha \sim 2$–5 (Priedhorsky et al. 1979; Barr & van der Woerd 1990; Balucińska & Hasinger 1991), a blackbody or thermal bremsstrahlung with a temperature 0.2–0.3 keV (Barr & van der Woerd 1990; Balucińska & Hasinger 1991), or a broad Gaussian line near 700 eV (Barr & van der Woerd 1990).

Barr & van der Woerd (1990) and Balucińska & Hasinger (1991) argued that this soft excess component was too complicated to be understood as a thermal spectrum from a simple accretion disk. Similar soft excess components were also recognized in other BHCs (GX 339-4, Ilovaisky et al. 1986; GS 2000+25, Terada 1994).

A X-ray transient GS2023+338 showed a soft excess component which exhibited time variation on time scales of a few hours (Inoue 1992). This component is quite different from that discussed above, and may be understood in terms of the interstellar dust scattering. This component was also recognized in the system of Cyg X-1 (Kitamoto Miyamoto & Yamamoto 1989), but a large amount of the soft excess flux could not be explained if this component arose from the dust scattering (Kitamoto et al. 1989, Balucińska & Hasinger 1991).

Finally, it should be noted that, in about half of energy spectra of Seyfert galaxies, soft excess components have also been observed (Turner & Pounds 1989 and reference therein.). Some of these soft excess components showed different time variations from hard power law

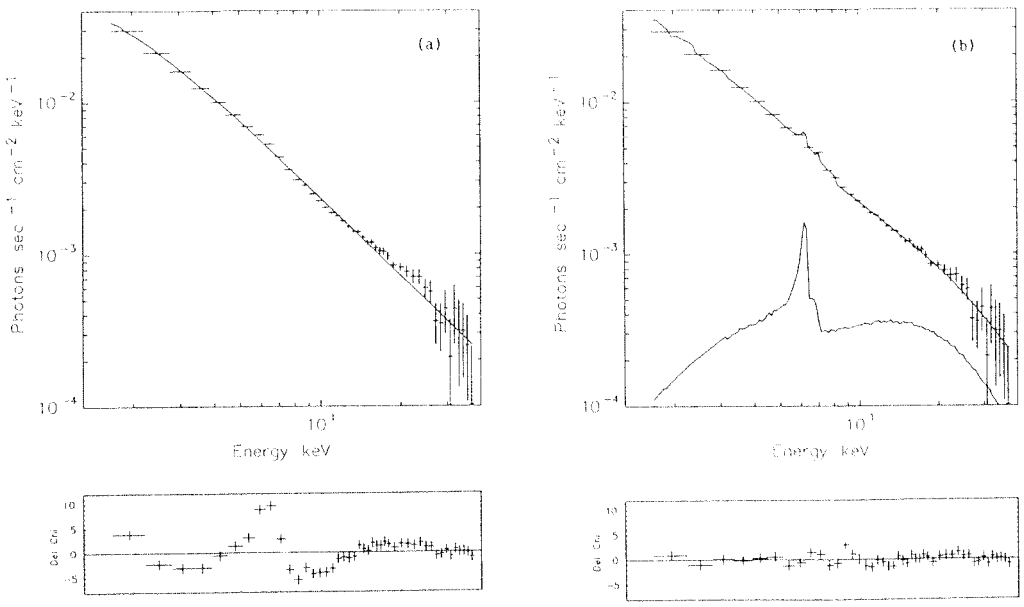

Figure 2.7: The spectra shown by the points with errors are a composite spectrum produced from 12 spectra of 8 AGNs obtained with *Ginga*. The best-fitting model spectra and their residuals for a power model (*left*) and a power law plus reflection and warm absorber model (*right*) are indicated by the solid lines in the upper panels and the points in the lower panels, respectively. The spectrum with a flat continuum and sharp peak near 6.4 keV in the right panel is the reflection component (from Pounds 1989).

components (e.g., Mkn 335, Pounds et al. 1986; Turner & Pounds 1988; Mkn 509, Morini, Lipani, & Molteni 1987; Singh et al. 1990).

Reflection

To interpret an observed broad hump between $\sim$ 10 keV and $\sim$ 300 keV in the spectra of AGNs, Lightman and White (1988) investigated reprocesses of X-rays by optically thick cold matter, and succeeded in reproducing the broad hump (see also Guilbert & Rees 1988). The cold material is thought to be an accretion disk or cold gas around the nonthermal source. As shown in Fig. 2.7, this model has successfully explained fine structures of many AGN spectra in the 2-30 keV range (Pounds et al. 1990; Matsuoka et al. 1990) just like those of Cyg X-1; an Iron K line, a broad absorption-like structure between 7 keV and $\sim$ 10 keV and a high energy excess at the higher energies (Inoue 1992).

Done et al. (1992) applied the reflection model to the spectrum of Cyg X-1, and found

that the model was more suitable to the observed spectrum than a partial covering model. Moderate-resolution X-ray spectra with *BBXRT* were also consistent with those expected from a superposition of direct power law component and its reflected component by a cold disk (Marshall et al. 1993). Spectra of GX 339-4 in the low and off states observed with *Ginga* were also found to be well represented by the reflection model, and ionization levels of the cold matter (disk) showed a positive dependence on the X-ray flux (Ueda et al. 1994; for X 1608-522, Mitsuda 1992).

George & Fabian (1991) progressed the reflection model by considering the geometry of the source and reflection material, the elemental abundance and the orientation of the system to the observer (also see Matt et al. 1989, 1991). The comparison of an observed spectrum with those results will provide information on them. From energy spectra of Seyfert galaxies obtained with *Ginga*, Nandra & Pounds (1994) concluded that the observed hard tail and iron line strongly suggested the existence of an accretion disk subtending $\sim 2\pi$ str from the power law source. (For Cyg X-1, see §10.3.3).

2.3.2 Time Variation

X-rays from BHCs in the hard states exhibit largely aperiodic time variations on time scales of a few hundred seconds to milliseconds. The time variations are sometimes called "flickering", and one of the signatures as black hole candidates. Especially, time variations of Cyg X-1 have been deeply investigated for two decades. In this subsection, previous analysis methods for these time variations and the results are shown, and attempts to interpret them are introduced.

Power Spectrum Analysis

The power spectrum is a powerful and useful method to analyze time series data. It decomposes the time series data into amplitude and phase components (e.g., van der Klis 1989). The amplitude components have been studied by means of a power spectral density (PSD), an auto-correlation function (ACF) which is a Fourier transform of the PSD, or a variability coefficient which is an integral function of the PSD. (The PSD defined here is merely denoted as the "power spectrum" in some literatures.) The phase components have been studied by means of a cross spectrum and a cross correlation which is a Fourier transform of the cross spectrum.

Nolan et al. (1981) found that the PSD of Cyg X-1 in the low state they obtained showed a power-law spectrum with a slope of about -1 in the $5 \times 10^{-2} - 3$ Hz frequency range, below which the spectrum was almost flat. Such a break frequency, however, changed from 4×10^{-2} Hz to

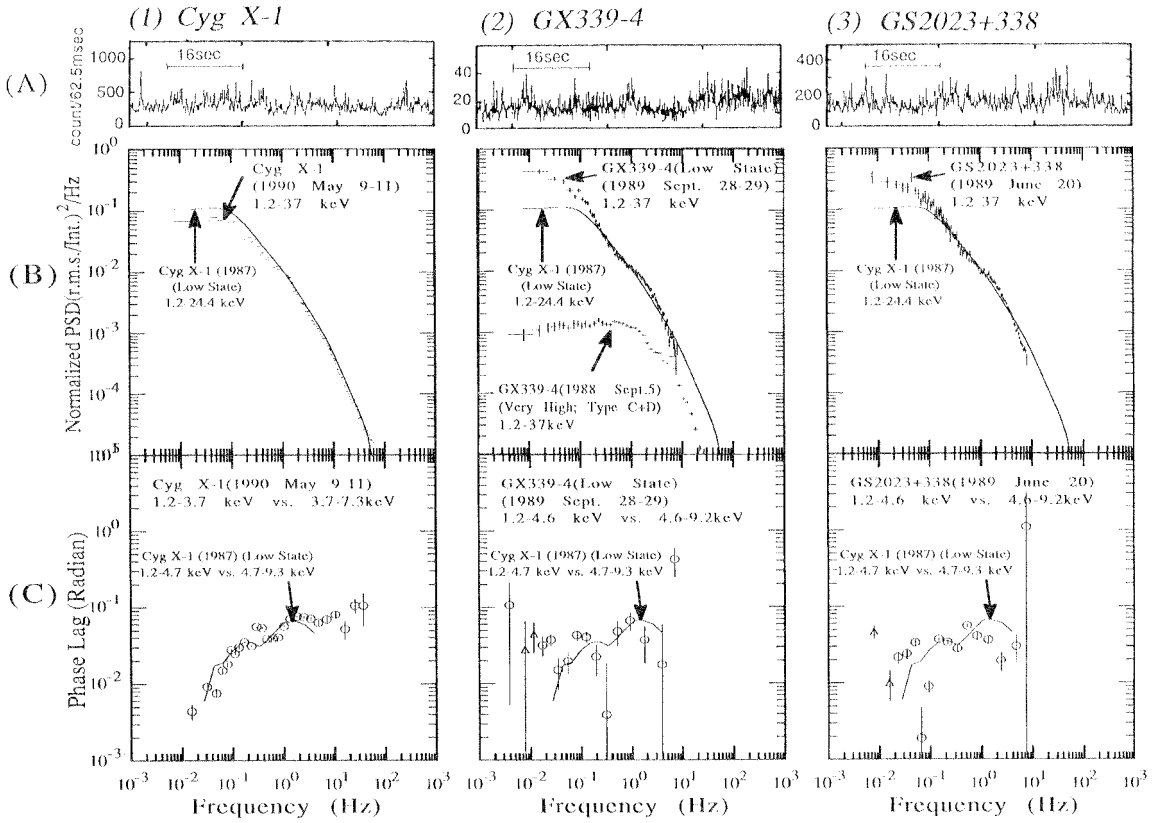

Figure 2.8: X-ray light curves (A), normalized power spectral densities (B), and phase lags (C) of three well known BHCs, Cyg X-1 (1), GX 339-4 (2) and GS 2023+338 (3), in the hard states. In (2), a normalized power spectral density of GX 339-4 in the soft (very high) state is also shown (From Miyamoto et al. 1992).

4×10^{-1} Hz in the *EXOSAT* observations of Cyg X-1 (Belloni & Hasinger 1990a). This kind of changes in the PSDs of Cyg X-1 was also confirmed in the two *Ginga* observations (Miyamoto et al. 1992). There are one or two more bends at frequencies around 1 and 10 Hz, above which the slope is about -1.8 to a frequency of about 10^2 Hz (Makishima 1988, Kitamoto and Miyamoto 1989).

Cross correlations of intensity variations in two energy bands had been calculated, and asymmetric structures in the resultant diagrams suggested hard X-ray lags due to the Comptonization (Priedhorsky et al. 1979; Nolan et al. 1981; Page 1985). Using a cross spectrum obtained with *Ginga*, however, Miyamoto et al. (1988) showed frequency-dependent time-lags of hard X-rays in the $10^{-1} - 10^1$ Hz frequency range, which could not be explained by a simple

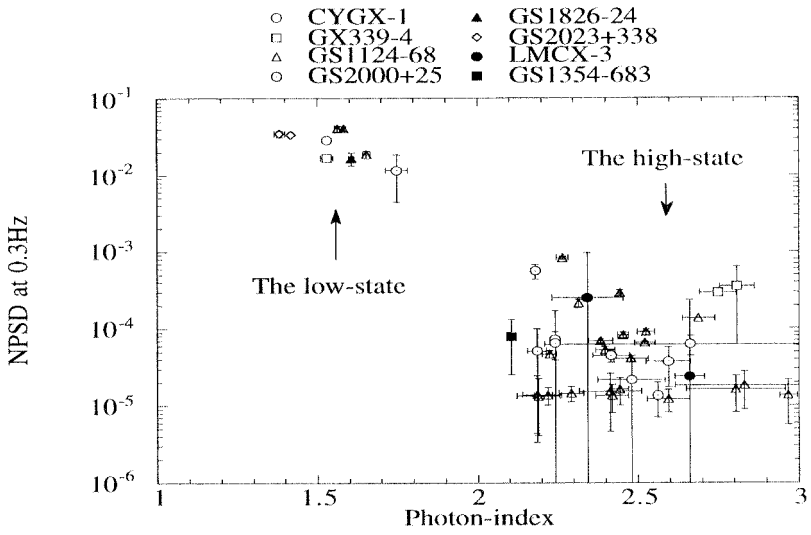

Figure 2.9: The relationship between photon indices of power-law energy spectra and normalized power spectral densities at 0.3 Hz (relative squared amplitude) of various BHCs in the hard/low and soft/hard states (from Terada 1994).

Comptonization model. This kind of hard X-ray lags is also different from those of LMXBs (van der Klis et al. 1987; Miyamoto et al. 1993).

Characteristic time variations very similar to those of Cyg X-1 were also observed in other BHCs, GX 339-4 (Samimi et al. 1979; Maejima et al. 1984), GS 2023+338 (Tanaka 1989), GS 1124-684 (Miyamoto et al. 1993) and GX1826+213 (Tanaka 1989) in the hard states. Relative amplitudes of the time variabilities and hard X-ray lags in Cyg X-1, GX 339-4, GS 2023+338, GS 1124-684 and GS 2000+25 are found to be similar at frequencies above break frequencies (Miyamoto et al. 1992, 1993; Terada 1994) (Fig. 2.8). Thus, not only in the energy spectra, but also in the time variabilities in the SBHCs, the "canonical time variations" have been established.

Note that the power-law energy spectra in the hard states are different from those in the soft states as shown in Fig. 2.9. As mentioned previously, photon indices in the hard and soft states are 1.5–1.7 and 2.1–3, respectively, and are plotted in the horizontal direction in Fig. 2.9. While the relative amplitudes of the time variabilities to the flux of the power-law component in the hard states are larger than those in the soft states, which is expressed as NPSDs at 0.3 Hz in Fig. 2.9.

MBHCs (AGNs) also exhibit chaotic time variations (Fig. 2.10). *EXOSAT* "long look" observations showed that X-ray time variabilities in AGNs (NGC 4051, NGC 5506, MCG-6-30-

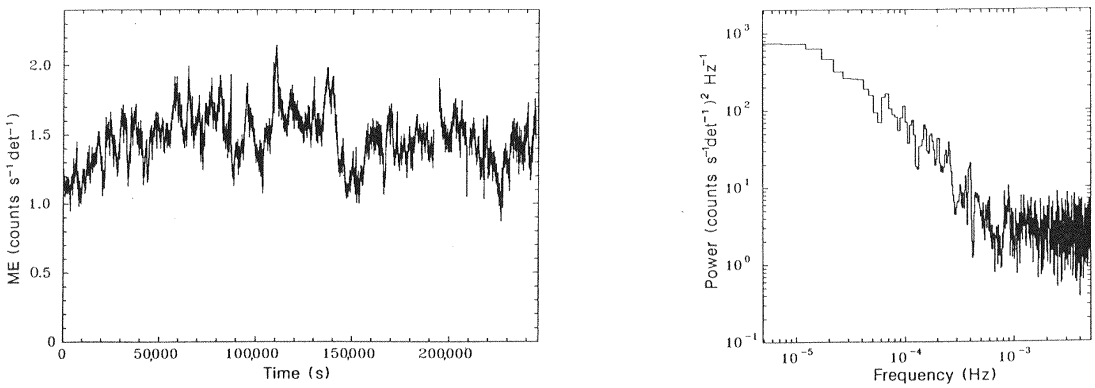

Figure 2.10: A X-ray light curve of a Seyfert galaxy, NGC5506, (*left*) and its PSD (*right*) from the *EXOSAT* "long look" observation (from McHardy & Czerny 1987).

15 and Mkn 335) except a quasar (3C273) were very similar to that in Cyg X-1, that is, to those in SBHCs (Lawrence et al. 1987; McHardy & Czerny 1987; Pounds & McHardy 1988; McHardy 1989). The PSDs of them have a slope of 1–2, not "1/f noise", in the range of 10^{-5} to 10^{-4} Hz (McHardy 1989; Lawrence & Paradakis 1993), and, in some AGNs, have a break frequency near 10^{-6} Hz.

Thus, in the time variabilities as well as the energy spectra, it is difficult to find X-ray properties of MBHCs different from those of SBHCs. Exceptions in MBHCs are some Seyfert 2 galaxies with heavily obscured nuclei (McHardy 1989; c.f., Awaki et al. 1990) and quasars from which X-rays are thought to be radiated by a different process, syncrotron-self-Compton radiation (e.g., Tashiro 1991). Green, Mchardy, & Lehto (1993), however, pointed out that AGNs with the steepest energy spectra were possibly the most variable. This tendency has not been recognized in SBHCs.

The power-law energy spectrum and the chaotic time variations may not discriminate BHCs from the other compact sources. A low mass X-ray binary, X 1608-522, also exhibited a power-law energy spectrum and a "flicking" time variation when the intensity was low (e.g., Mitsuda 1992). This may indicate that the BHCs in the hard states can not be distinguished from the LMXBs in the hard states (Tanaka 1989). A photon index of the power-law spectrum ($\sim$ 2) and a NPSD of the time variation are, however, slightly different from those in BHCs. These slight differences may be important. Thus, further studies are necessary to answer this problem.

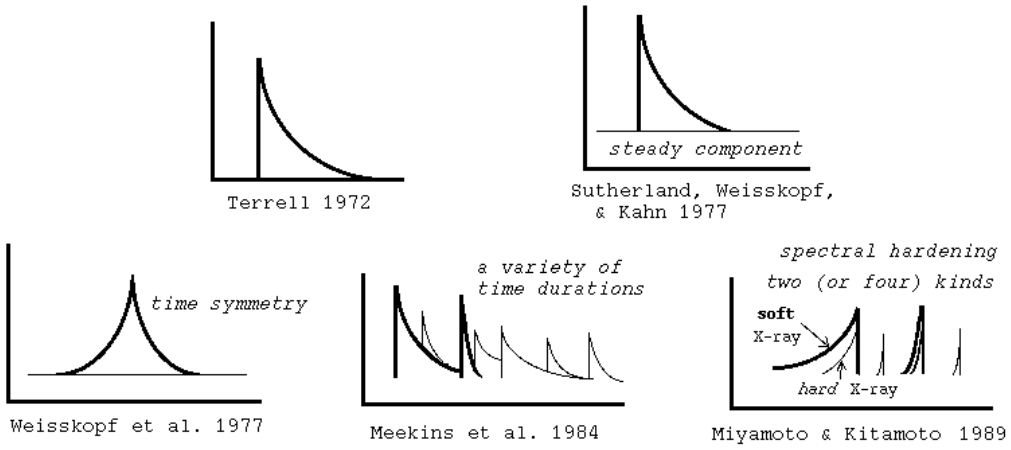

Figure 2.11: History of previous shot noise models. Schematic drawings of proposed profiles different from the others are shown.

Shot Noise Model

The above results in the timing analyses are useful for the classification of compact objects, but less suggestive for the cause of the time variability. This is mainly because a quarter of the information of time series, absolute phase values, is lost in producing a PSD and a cross spectrum. For the lack of the information, one must add some assumptions to them to reproduce the time variability from them. A *shot noise model* is a traditional approach to simulate the time variability and be connected with some physical processes, e.g. accretion disk instabilities (Lightman & Eardley 1974; Shakura & Sunyaev 1976), magnetic flares (Galeev et al. 1979; Pudritz & Fahlman 1982; Volwerk, van Oss, & Kuijpers 1993), aperiodic mass accretion (Lightman & Eardley 1974; Mineshige et al. 1994a,b) and so on.

A shot noise model was first introduced to explain fluctuations in optical luminosity of QSO 3C273 by Terrell and Olsen (1970), and applied to the X-ray variability of Cyg X-1 (Terrell 1972). In usual shot noise models (Terrell 1972; Weisskopf, Kahn, & Sutherland 1975; Oda et al. 1976; Rothschild et al. 1977; Canizares & Oda 1977; Ogawara et al. 1977; Sutherland, Weisskopf, & Kahn 1978; Priedhorsky et al. 1979; Nolan et al. 1981; Meekins et al. 1984; Miyamoto & Kitamoto 1989; Lochner, Swank, & Szymkowiak 1991), the time variability of Cyg X-1 has been assumed to consist of many randomly occurring pulses, "shots". Characteristic shapes of the shots have been determined from a mean count rate, variance, PSD (, ACF or variability coefficient) and other timing analyses of observational data (e.g., Sutherland et al. 1978).

It has been found that the above results in the timing analyses (mainly in Cyg X-1) are better explained by the following additional assumptions; (1) the shots have a time symmetric

rise and decay (Weisskopf et al. 1978; Lochner et al. 1991). (2) a steady component exists (Sutherland et al. 1978). (3) The durations and peak intensities of the shots have some (power-law) distributions (Meekins et al. 1984; for AGNs, Lehto 1989; Lawrence & Paradakis 1993; Green et al. 1993). (4) the energy spectrum of the shot hardens with the intensity increase (Miyamoto & Kitamoto 1989). (More detailed description about shot noise models is found in Lochner et al. 1991; Mereghetti 1993) Recently, an average profile of the shots was directly obtained by superposing a number of shots without any additional assumption (Negoro, Miyamoto & Kitamoto 1994).

2.4 Theoretical Models of the Time Variations

Physical interpretations of the short-term time variability (the shots) may be classified into the following three groups; (1) disk instability models (Lightman & Eardley 1974; Shakura & Sunyaev 1976), (2) magnetic reconnection models (Galeev, Rosner & Vaiana 1979; Pudritz & Fahlman 1982; Volwerk, van Oss & Kuijpers 1993) and (3) the others. The first two models are discussed in the framework of the standard α disk model (Shakura & Sunyaev 1973; Novikov & Thorne 1973).

2.4.1 Disk Instability Models

In the optically thin disk, a heating rate by the viscous disspation exceeds cooling rates by thermal bremsstrahlung or Comptonization cooling processes, and the disk is thermally unstable (Pringle and Rees 1972; Shibazaki and Hoshi 1975). In the optically thick disk, the blackbody radiation releases energy from the disk so effectively that the disk is stable. At a high accretion rate, however, an inner portion of the disk is so luminous that the radiation pressure exceeds the gas pressure at the region. As a result, the disk becomes thermally unstable (Shibazaki and Hoshi 1975; Shakura and Sunyaev 1976). (Such a radiation pressure-dominated region is referred as an "inner region".) These instabilities are called the "*thermal instabilities*".

The optically thick, radiation pressure-dominated disk is also found to be dynamically unstable (Lightman and Eardley 1974; Lightman 1974a, b). In such a disk, the (vertical integrated) viscosity $W_{r\varphi}$ is not controlled by the local density of accretion matter (e.g., $W_{r\varphi} = 2\alpha h P_{rad} = 2\alpha h a T^4/3$, where h is the half-thickness of the accretion disk, and a is the radiation density constant). If some perturbation makes the disk thickness large, then the viscous force becomes larger at the region, and accretion matter flows inward, making concentric dense regions. In this way, the disk breaks up into rings. This instability is called "*viscous (, dynamical, secular*

or L-E) instability".

Shakura & Sunyaev (1976) described two time-dependent equations for mass transfer and energy conservation in the optically thick disk, and found two kinds of solutions that perturbations exponentially grew with time (§10.4.1). According to them, the thermal instability occurs faster than the viscous instability. Piran (1978) generalized their theory, and demonstrated that inner regions of other α viscous type disks such as the two-temperature disk (Shapiro, Lightman and Eardley 1976) and the coronal disk (Liang and Price 1977) were also thermally unstable. Nowak (1994) explained power spectra of GX 339-4 in the framework of these disk instabilities.

Some of these instabilities are stabilized or modified if some additional heating and/or cooling processes work (Abramowicz et al. 1988; Czerny, Czerny, & Grindlay 1986; Kusunose & Mineshige 1992; Mineshige & Kusunose 1993 and the references therein).

2.4.2 Magnetic Reconnection Models

The origin of the magnetic field in the accretion disk and its role are still under investigation (Shibata, Tajima and Matsumoto 1990; Tout and Pringle 1992; Volwerk, van Oss and Kuijpers 1993). Initially, it was thought that the magnetic field within the accretion disk worked as a mechanism of angular momentum transfer (Lynden-Bell 1969; Shakura and Sunyaev 1973; Eardley and Lightman 1975).

Wheeler (1977) first pointed out a possibility that the time variability of Cyg X-1 arose from the magnetic field reconnection. Bisnovatyi-Kogan & Blinkov (1977) also showed importance of the magnetic field at a high accretion rate. Under a hypothesis of the existence of hydrodynamic flows within the disk, Galeev et al. (1979) demonstrated that the reconnection mechanism within the disk was not so rapid that the magnetic field developed enough to have an energy density comparable to a thermal energy density, and speculated that magnetic field tubes within less plasma appeared on the disk surface by buoyancy force and reconnected just like solar flares, resulting in the fluctuations of the X-ray intensity (Fig. 2.12).

Pudritz (1981a,b) and Pudritz and Fahlman (1982) considered a self-consistent disk structure taking account of the magnetic fields, and proved that the magnitude of a magnetic energy fluctuation became comparable to a Kepler energy density, and that this dynamo driven disk appeared in the gas pressure dominanted disk. These authors also proposed comparing observed shots and millisecond bursts with the magnetic reconnection, based on experimental scaling relations (§10.4.2).

These theories have advantages over the disk instability theories that the magnetic flares

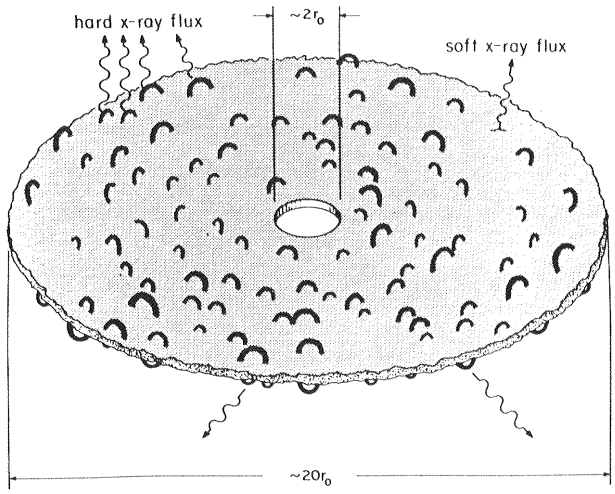

Figure 2.12: A schematic drawing of the inner portion of an accretion disk with $r_0 \equiv 6GM/c^2$ in the magnetic flare model. The solid curves drawn above and below the disk are magnetic tubes (from Galeev et al. 1979).

arise in the gas pressure-dominated disk (that is, at low luminosity), and that the magnetic flares are really observed as solar flares exhibiting non-thermal energy spectra. Thus, observed PSDs, which are inconsistent with shots with a single duration, have often been interpreted in terms of these magnetic flares with various durations (Meekins et al. 1984; Lochner et al. 1991; Lehto 1989; Lawrence & Paradakis 1993; Green et al. 1993).

2.4.3 Aperiodic Mass Accretion Models

The observed luminosity is thought to be proportional to the accretion rate. Thus, it is natural to think that the intensity variability is caused by variations of the mass accretion rate (Rothschild et al. 1974; Miyamoto et al. 1992). In fact, in the α disk model, the observed time scale of the shots ($\sim$ 0.3–1 sec) is likely to be corresponding to the drift time scale, $\tau_{drf} = r/|v_r|$, as shown below (Lightman 1974a, Pringle 1981).

$$\tau_{Kep} \sim \tau_{hyd} \sim \alpha\tau_{thr} \sim \alpha \left(\frac{h}{r}\right)^2 \tau_{drf}, \tag{2.4}$$

where τ_{Kep} is referred as the Keplar motion time scale defined by

$$\tau_{Kep} \equiv \frac{1}{\Omega} = 0.73 \left(\frac{r}{3r_s}\right)^{\frac{3}{2}} \left(\frac{M}{10M_o}\right) \text{ms}, \tag{2.5}$$

τ_{hyd} is the hydrodynamical time scale on which discontinuous physical quantities having a sound speed (shocks and magnetic disturbances, and so on) propagate to the vertical direction in the disk (and hydrodynamical equilibrium is established), and τ_{thr} is the thermal time scale on which photons escape through many scatterings from an interior of the disk to the surface (as a result, the disk is thermalized). Note that the above relation holds in the inner (radiation pressure-dominated) region.

Miyamoto and Kitamoto (1989) found in their shot noise model that shots in different energy bands had different time constants, and attributed it to spectral hardening during the shot. They interpreted this spectral hardening as thermal heating due to the release of gravitational energy when clumps of accretion matter drifted inward.

The aperiodic mass accretion may be caused by the viscous instability (Lightman and Eardley 1974). In general cases, however, accretion matter diffuses under the action of viscous torques, and fluctuations of the mass accretion rate can not be expected in the α disk models.

Recently, Mineshige et al. (1994a,b) constructed the following time-variability model, self-organized critical (SOC) model, to explain observed power-law PSDs of BHCs. An inner portion of the black-hole accretion disk is composed of numerous small reservoirs to accumulate accreting matter. If a mass density at some reservoir reaches to some critical value, an unknown instability becomes established and the accumulated material drifts inward as an avalanche, thereby emitting X-rays. When a large number of reservoirs are involved with an avalanche, a big X-ray shot is generated, whereas a small-scale avalanche yields a small shot. This model is rather rough, but successfully reproduces *almost* randomly occurring shots.

2.4.4 Other Models

A number of models to explain the chaotic time variations have been proposed, and disappeared. One of plausible (often referred) models except the models described above is a rotating spot model. Hot spots on the disk may come from the thermal instability (Shakura & Sunyaev 1976), or magnetic vortices (flares) (Abramowicz et al. 1992). Some observed PSDs of AGNs were able to be interpreted by this model (Abramowicz et al. 1989; Green et al. 1993). A quasi-periodic oscillation will be expected from this model, but have not been reported. Another interesting model for the time variability is pair tidal disruption of small black holes (Pacholczyk & Stoeger 1994).

Chapter 3

Instruments

All the data used in this thesis were obtained with the large area proportional counter (LAC) on board the *Ginga* satellite. In this chapter, three instruments of *Ginga* and the X-ray background in the LAC are described.

3.1 Ginga Satellite

3.1.1 Satellite and Scientific Instruments

The Japanese X-ray astronomy satellite, *ASTOR-C*, was launched by the Institute of Space and Astronautical Science (ISAS) from the Kagoshima Space Center (KSC) on 1987 Feb 5, and successfully thrown into a slightly elliptical orbit ($e \simeq 0.01$) with the apogee of 670 km, the perigee of 510 km and the inclination of 31°. Then, this third Japanese X-ray observatory was named *Ginga* standing for the galaxies in Japanese (Makino and the ASTRO-C team 1987). The orbital period is about 96 minutes and the argument of perigee rotates in the orbital plane with a 37-day period.

Fig. 3.1 shows a schematic view of this spacecraft. The size and weight of *Ginga* are approximately $1000 \times 1000 \times 1550$ mm and 420 kg, respectively. *Ginga* carries the following three scientific instruments.

The Large Area Proportional Counter (LAC)

The LAC is the main instrument of *Ginga* (LAC; Turner et al. 1989). The LAC has the largest effective area (~ 4000 cm^2) and most sensitive instrument in the medium X-ray energy band in X-ray astronomy satellites. The details of the LAC are presented in the following section.

The All Sky Monitor (ASM)

The ASM is an X-ray sky monitor system with a wide field of view in the energy range of 1–20 keV (Tsunemi et al. 1989a). It consists of two proportional counters with six different fields

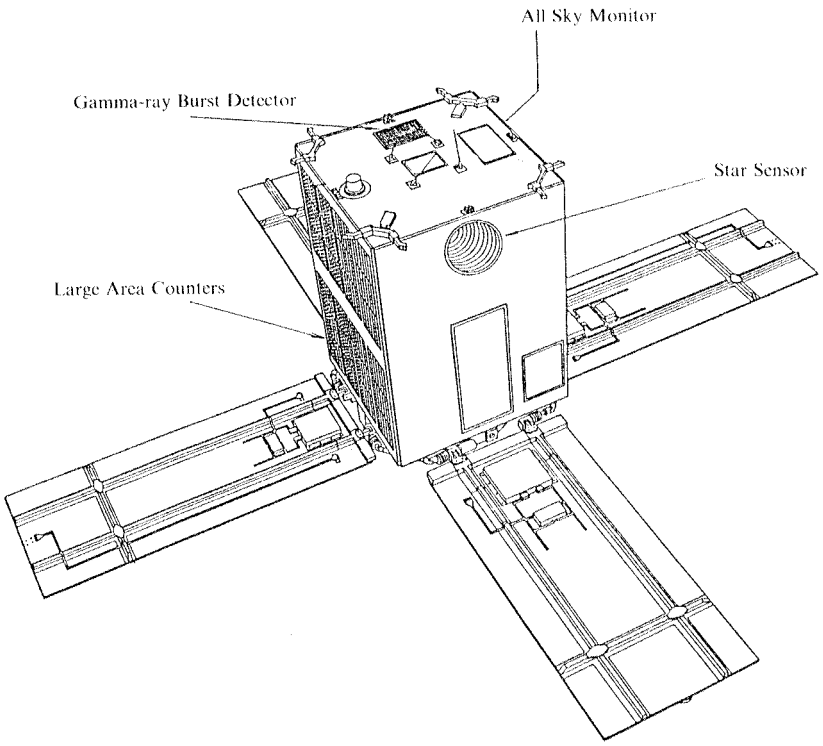

Figure 3.1: The configuration of the *Ginga* satellite (Turner et al. 1989).

of view, each of which is $1° \times 45°$ (FWHM). The ASM scans about 70 % of the sky during a rotation of the satellite around the Z-axis with the detection limit of 50 mCrab (Fig. 3.2). The ASM monitored long-term (more than 4 years) X-ray intensity variations of more than 100 X-ray sources, and found several X-ray transient sources including 4 BHCs.

The Gamma-ray Burst Detector (GBD)

The GBD is designed so as to detect gamma-ray bursts, and consists of one set of a NaI scintillation counter (SC) and a Xe-filled proportional counter, covering from X-rays to γ-rays in the energy range of 1-384 keV (Murakami et al. 1989). A radiation belt monitor (RBM), a solid state detector in the GBD, is utilized as a monitor system of high energy particle background which is trapped in the orbit (§3.3.2) and damages the above two instruments.

3.1.2 Attitude Control

The satellite attitude is stabilized by a momentum wheel (MH) which carries the Z-axis angular momentum of the satellite, and three magneto-torquers (MTQ). By changing the

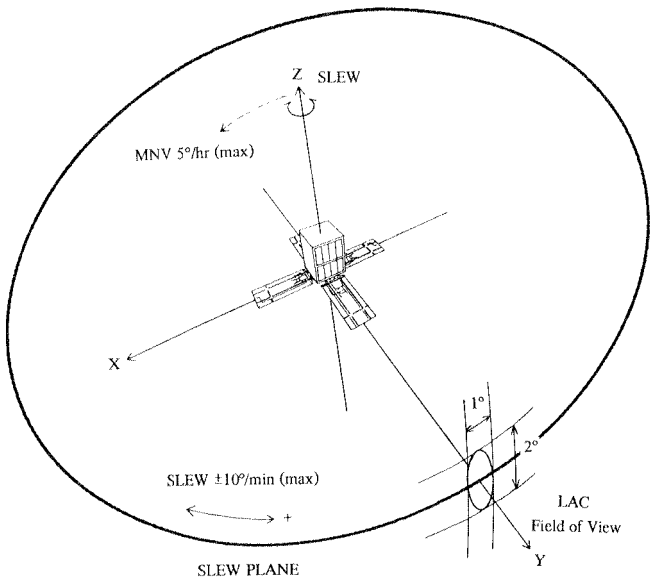

Figure 3.2: The collimator field of view (FWHM) and the satellite three axes (Turner et al. 1989).

rotation speed of the MH, the satellite body rotates around the Z-axis at a rate of 14° min^{-1} at maximum, which is called "slew" (Fig. 3.2). While, the direction of the Z-axis is changed at a relatively slow rate (5° hr^{-1}) by using an interaction of the MTQ and the geomagnetic field, which is called "maneuver". In the pointing mode, the attitude is stabilized within 0.1° day^{-1} using on-board gyroscopes. In later (1990∼) observations, however, a rotation speed of the MH became unstable, and the stability became worse. An absolute attitude of the satellite is determined on the ground with a typical accuracy of about 0.02° using star images taken with two star trackers (STT), the gyroscopes, geomagnetic sensors and the Sun angle from the non-spin-type solar attitude sensor (NSAS).

The satellite attitude is constrained by the NSAS. The NSAS must be greater than 135° for the solar paddles attached on the bottom of the satellite (− Z-axis direction) to receive enough sunlight.

3.1.3 Data Acquisition

Ginga makes contact with the ground station at KSC for about 10 min during 5 successive orbits out of 15 revolutions a day. This 5 and the other 10 orbits are called "contact" and "remote" paths, respectively. The on-board data processor (DP) edits obtained data including

attitude and housekeeping data into a telemetry format in one of the following three bit rates; "high" (16 kbps), "medium" (2 kbps) and "low" (512 bps). The data obtained at positions, where the satellite cannot make contact with the ground station, are stored in the on-board bubble data recorder (BDR). As the BDR has the limited capacity of 41.9 Mbits, the data for about 1366 (low bit rate), 341 (medium) or 43 (high) min are stored.

3.2 Large Area Proportional Counter

3.2.1 Structure

Under a Japan-US collaboration, the LAC was designed to obtain medium and hard X-ray energy spectra of nearby and distance faint objects, and to investigate rapid time variations of compact objects. Thus, it consists of eight identical proportional counters with a large effective area of about 4000 cm^2 in amount and a wide energy range of $1.2 - 37$ (60) keV.

The structure of each counter of the LAC is shown in Fig. 3.3a. X-ray photons passing through the collimator drawn on the top of the figure and penetrating through the beryllium window are detected in the multi-wire array. The collimator restricts the LAC field of view to $1.1^\circ \times 2.0^\circ$ (FWHM) as shown in Fig. 3.4. The elliptical field of view is due to the fact that the satellite attitude is more stable in the Y direction than in the Z direction. The collimator is made of 25 μm stainless steel, and painted with silver to prevent incident photons colliding with the surface of the collimator from producing the iron fluorescence line at 6.4 keV. The thickness of the beryllium foil attached on the entrance window is 62 μm, which is determined from the strength to support gas pressure of the counter and soft X-ray response.

The counter is filled with the gas composed of argon 70%, xenon 25% and carbon dioxide (as quenching gas) 5%. Xenon is used to increase sensitivity of hard X-ray photons. The total gas pressure is 1.86 atm at 273 °K. Each detector has a multicell structure divided into 4 layers and 13 lines, which are electrically connected by anode wires as shown in Fig. 3.3b. The two wires in the top layer, L1 and R1, and the wire in the middle layer, S23, are used to detect X-ray events. The other wires, V1 and V2, and an end guard cathode (EV) at the ends of these wires are used as monitors to detect charged particles (§3.3.2).

3.2.2 Efficiency and Data Modes

Fig. 3.5 illustrates the efficiency of the LAC of the L1 + R1 ("top"), S23 ("mid") and their sum as a function of energy. Soft X-rays are absorbed by the beryllium window, resulting in the decrease of the efficiency at lower energies. While, the efficiency at hard energies is

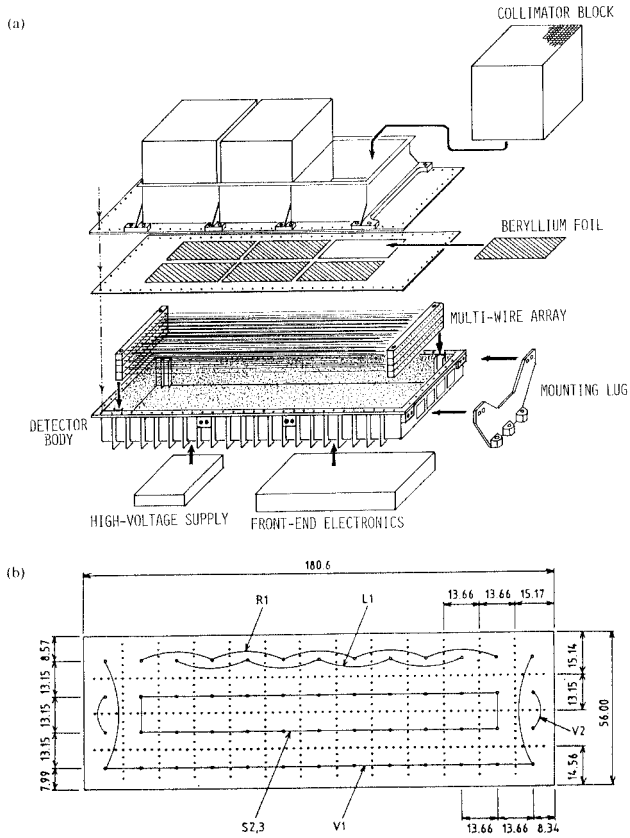

Figure 3.3: The structure of a LAC detector. Each length in (b) is indicated in units of mm (Turner et al. 1989).

determined by the composition of the gas and its pressure. The discontinuities of the efficiency at the energies of 3.0, 4.8 and 29.6 keV are due to the edge absorptions of the gas (the K-edge of argon and the L and K-edges of xenon, respectively).

The efficiency and a response matrix used in fitting observed energy spectra were constructed based on ground calibrations, and confirmed and calibrated by observing Crab nebula, a supernova remnant Cas A and other standard X-ray sources. Fine adjustment of the energy scale can be proceeded by using the line center energy at 22.1 keV of silver painted on the collimator.

Each LAC detector has its own high voltage (HV) supply. The HV is usually set to be about 1830 volt so as to observe 1.2 – 37 keV X-rays. The energy resolution is 18.0 % at 6 keV and scales as $E^{-1/2}$. By reducing the HV, the energy range can be extended up to about 60 keV. These energy ranges are equally divided into 64 energy channels by an analog to digital

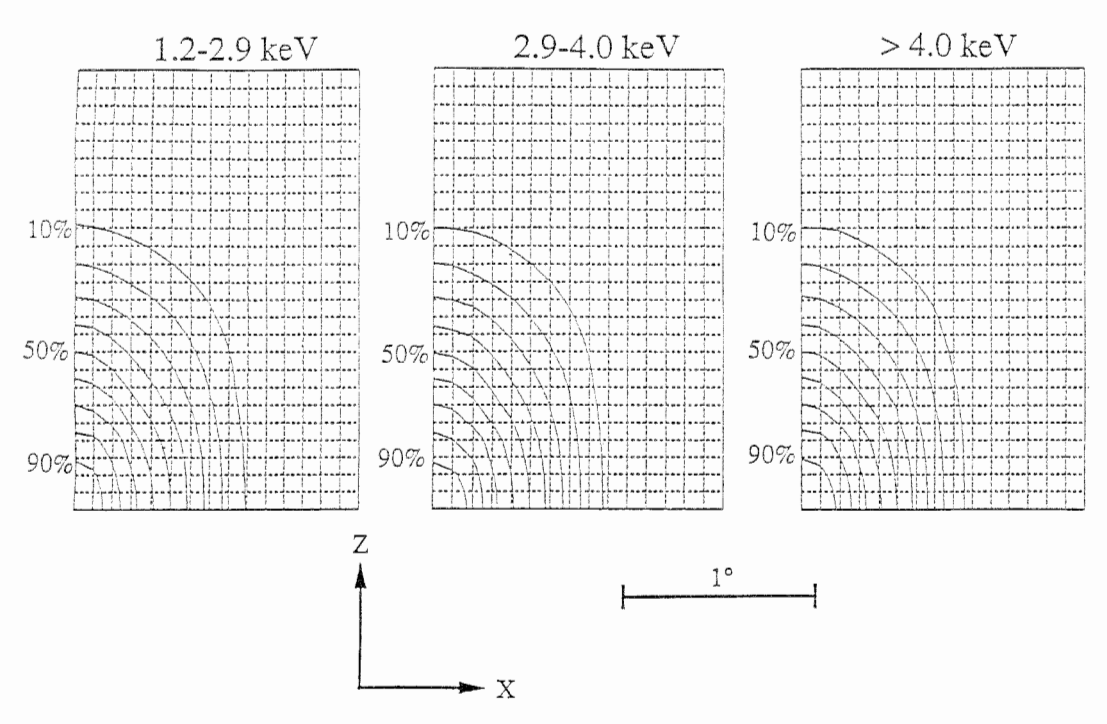

Figure 3.4: The collimator angular response function. The grid size between the dotted lines shown is 0.1° (Turner et al. 1989).

converter (ADC), and the higher 32 channels are combined in pairs, resulting in 48 channels. Furthermore, these data are combined according to the data modes referred as MPC1, MPC2 and MPC3 (see below and Table 3.1). In addition, for study of very fast time variations, a PC mode is provided in which the ADC is not used so that the dead time is reduced from 206 μsec to 16.5 μsec. The data mode is selected according to a purpose in each observation.

MPC1 mode

Signals from each of the 2 layers and each of the 8 counters are processed separately, and producing 16 spectra with 48 channels. This mode is mainly used for spectral study.

MPC2 mode

Signals from the 2 layers and 4 counters are combined, resulting in 2 spectra with 48 channels. By the compression of the spectral information, time resolution improves by a factor of eight compared with the MPC1 mode.

MPC3 mode

All the events are accumulated into a single spectrum with 12 channels. Each energy channel

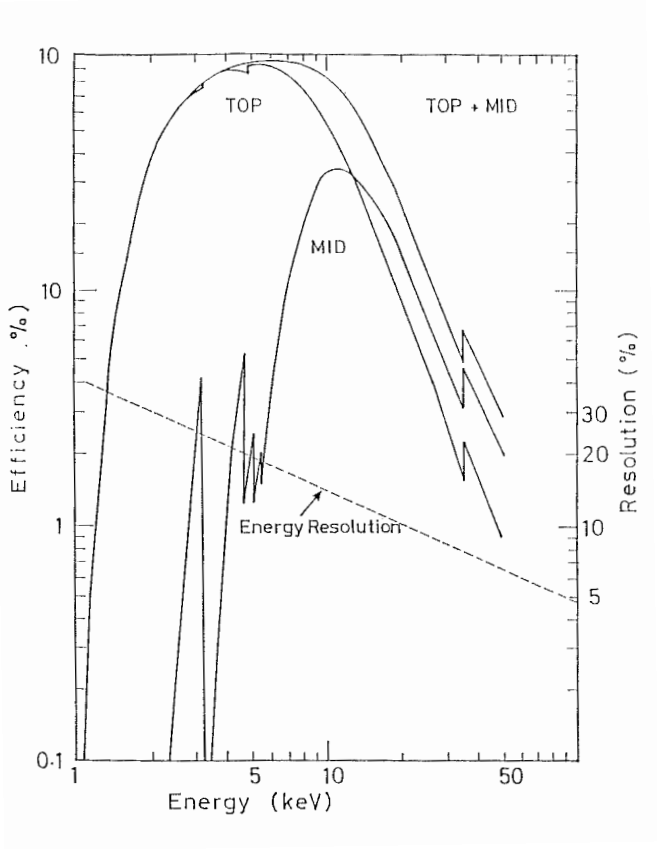

Figure 3.5: The efficiency of the LAC (solid curves) and the energy resolution (dashed line) as a function of energy (Turner et al. 1989).

corresponds to 4 consecutive channels in the above modes. By the compression of the spectral information, time resolution improves by a factor of eight compared with the MPC2 mode.

PC mode

Signals from the 2 layers and 4 counters are combined, and divided into two energy bands by three discriminators instead of the ADC.

3.3 Background in the LAC

Background events in the LAC can be divided into the diffuse cosmic X-ray background and internal background produced by non X-ray events (Hayashida et al. 1989).

Table 3.1:
DATA MODE OF THE LAC

Mode	Number of Spectral Bands	Time Resolution (Bit Rate)		
		High	Medium	Low
MPC 1	48	500 ms	4 s	16 s
MPC 2	48	62.5 ms	500 ms	2 s
MPC 3	12	7.8 ms	62.5 ms	250 ms
PC[a]	2	0.98 ms	7.8 ms	31.3 ms

a Time resolutions in the higher energy band are twice larger than those shown.

3.3.1 Cosmic X-ray Background

The cosmic X-ray background (CXB) has been known to be uniform and isotropic. A typical counting rate of the CXB is about 18 c/s/LAC. The origin is one of the mysteries since the beginning of the X-ray astronomy. To reduce the background, the LAC is shielded with 0.2 – 0.5 mm thick tin for all directions except the direction of the field of view of the LAC.

3.3.2 Internal Background

Internal background arises from cosmic-rays, geometrically trapped charged particles, fluorescence of X-rays, radio-active isotopes, and contaminations of the sunshine and its scattering by the atmosphere of the Earth. A counting rate of the internal background is $50 \sim 100$ c/s/LAC which depends on time, a position in the orbit and a direction of the field of view of the LAC. Of the internal background events, the solar contaminations can be completely excluded by using only the data without the contaminations (§4.2.1). The other background events are reduced in the LAC, and the residual events are evaluated as follows.

Charged particles

Charged particles due to the cosmic-rays and those geometrically trapped near the south atlantic anomaly (SAA) over Brazil produce γ-rays by colliding with the satellite body or the surface of the LAC, resulting in a significant increase in the internal background. These particles ionize the gas along their path, and usually produce signals in two or more cells. Using this fact, only signals which satisfy the relation, (L1 xor R1 xor S23) not (V1 or V2 or EV) where xor means "exclusive or", are regarded as true X-ray events. This "anti-coincidence" counting system reduces the charged particle background by more than 90 %.

γ-rays

In passing through the SAA, materials in the detectors and/or the satellite body become radio-

active. The radio-active isotopes have the decay time of 5.5 min, 41 min and 8 hours, and create γ-rays. The background due to the γ-rays by the charged particles and the radio-active isotopes can be also reduced by monitoring signals from V1, V2 and EV and using the above relation of the anti-coincidence.

The residual background events are mainly evaluated by the following parameters.

SUD; the SUD is the counting rate of X-ray-like events above the highest spectral channel (37 keV) of the LAC. As the detection efficiency at these energies is quite low, the SUD can be used as a monitor of the internal background.

COR; the COR is the cutoff rigidity of charged particles, defined as the minimum momentum per elementary charge to penetrate the magnetosphere of the Earth and reach a given point of the orbit.

MID; the MID is the counting rate detected in the middle layer in the 1-5 keV range. For the same reason of the SUD, this is thought to be used as a monitor of the internal background. As expected, the MID has a strong correlation with the SUD as shown in Fig. 3.6.

Furthermore, there are other parameters to monitor the internal background; the counting rate of the V2 (PIM) and the counting rate of the RBM (SOL2).

3.3.3 Reproduction of the Background

Since the background mainly depends on a position in the orbit, the background in the LAC can be reproduced from the housekeeping or environmental parameters through the following simple formula (Hayashida et al. 1989).

$$C(E,t) = F_1(E) + \sum_{n=2}^{N} P_n(t) \times F_n(E), \tag{3.1}$$

where $C(E,t)$ is the LAC counting rate, n is the label of the component, $P_n(t)$ is parameter depending on time, and $F_n(E)$ is the coefficients of the n-th component.

The time-independent component, $F_1(E)$, is mainly corresponding to the diffuse X-ray background, and determined from observations of high galactic sky positions. As the time-dependent parameters, the following four parameters are frequently used; the SUD, the COR, the MID and a component including the argument of perigee of the satellite orbit (Hayashida et al. 1989). The coefficients, $F_n(E)$, were determined from frequent observations of the fixed part of the source-free sky.

The first three components depend on orbital positions of the satellite (mainly due to the effect of the SAA), and reproduce a large ($\sim$ 100 %) variation of the internal background in a

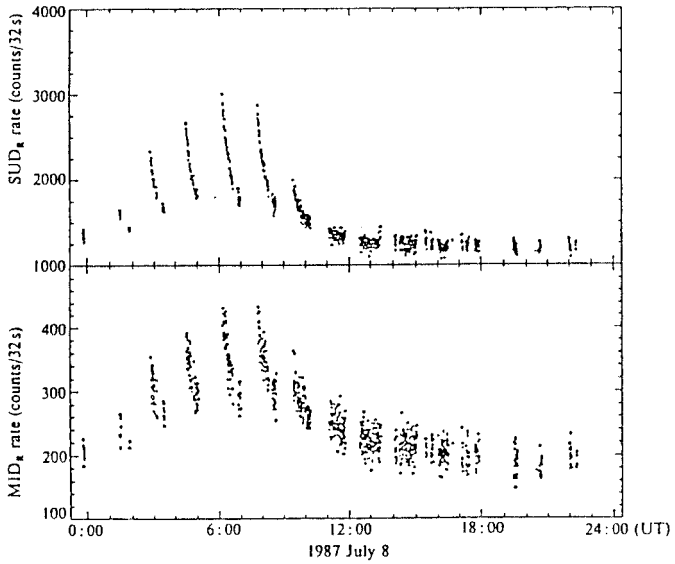

Figure 3.6: The background behavior during an observing day (Hayashida et al. 1989).

day (Fig. 3.6). The forth component describes variation of the altitude at which *Ginga* passes through the South Atlantic Anomaly, and reproduces a significant ($\sim$ 25 %) variation of the background of the 37-day period.

Of these time-depend parameters, the SUD is usually most sensitive to the internal background as shown in Fig. 3.6 so that the background is constructed according to the SUD counting rate ("SUD-sorting method"). The effect of the SAA can be considered if the COR is taken into account. This background production method is called "Hayashida Method I".

Even if these are no appropriate background data, background can be constructed by using a large data base taking account of the 37 day periodicity of the background and the MID counting rate ("Hayashida Method II").

Chapter 4

Observation

Three pointing observations of Cyg X-1 were carried out with the LAC in the Ginga's lifetime, and the first two set of the data were used in this analyses. In this chapter, the observations and data reductions are described in detail.

4.1 Observations of Cyg X-1

4.1.1 1987 August 5-8

The first observation of Cyg X-1 was performed through four days in the PV (performance verification) phase of *Ginga*. Cyg X-1 was in the low intensity state. PC data were obtained in the first day, 1987 Aug 5, to investigate millisecond structure of the time variability. The PC data are not suitable for this analyses because they have only 2 spectral bands and low counting rate per bin, resulting in large statistical count fluctuations. The data for the other 3 days were taken in MPC 2 or 3 high-bit-rate mode in contact orbits and in MPC 1 or 2 high-bit-rate mode in remote orbits. The data obtained on Aug 7 and 8 near the superior conjunction were not used in this analyses because intensity dips (Mason et al. 1974; Kitamoto et al. 1984, 1989) were sometimes observed. Thus, the only data on Aug 5 and 6 are available for this analyses.

The X-ray intensity increased by about 30 % ($\sim$ 1000 c/s) in 4 hours on Aug 6, but the energy spectrum hardly changed. Before aspect correction was applied to some data, the correlation between the intensity increase and values of the collimator transmission was investigated. This confirmed that the increase was due to the source activity.

4.1.2 1990 May 9-11

The second pointing observation of Cyg X-1 was carried out for three days as a Ginga-team project for massive X-ray binaries. PIs (principal investigators) in this observation were

Table 4.1:
DATA LOG OF CYGNUS X-1

Date			Data Mode	Exposure Time (sec)	Counting Rate (c/s)[a]	Orbital Phase[b]	ref[c]
1987	Aug 5	11.7 – 12.4	MPC2 H	1836	4700	0.59 – 0.60	1-5
	Aug 6	11.8 – 18.8	MPC3 H	10972	3500-4500	0.77 – 0.82	
1990	May 9	1.7 – 6.5	MPC3 H	5257	4800	0.53 – 0.56	5–7
	May 9	12.1 – 14.0	MPC1 M	2016	4300	0.60 – 0.62	
	May 9	23.8 – 6.5	MPC3 H	5238	4400	0.69 – 0.74	
	May 10	21.8 – 4.3	MPC3 H	6347	4800	0.85 – 0.90	

a. counts/s in 1.2 – 37.1 keV (1987) and 1.2 – 58.4 keV (1990) with the LAC(4000 cm^2)
b. according to Gies and Bolton (1982)
c. (1) Makishima (1988) (2) Miyamoto et al. (1988) (3) Miyamoto and Kitamoto (1989) (4) Kitamoto and Miyamoto (1989) (5) Ebisawa (1991) (6) Miyamoto et al. (1991) (7) Negoro et al. (1994)

Makishima and Kitamoto et al. The LAC high voltage was reduced during this observation in order to observe X-rays up to about 60 keV. Cyg X-1 was still in the low state. According to data of the ASM on board *Ginga*, Cyg X-1 had been in the low state through the Ginga's life (Egoshi 1995).

The X-ray intensity decreased by about 10 % on May 9, and recovered in the late afternoon (Table 4.1). The intensity variations are also due to the intrinsic source activity since no apparent correlation with values of the collimator transmission was recognized.

4.2 Data Selection and Reduction

Data were taken in various data modes in both the observations. Data taken in MPC 3 were used to investigate the time variability, and those in MPC 1 and 2 were used to obtain detailed information on the energy spectrum. So, different data selections and reductions were proceeded for the MPC 3 data and the MPC 1 and 2 data.

4.2.1 Data Reduction

Cyg X-1 could be observed for about a half of the period of each observation because of Earth occultation of the LAC field of view. In pointing the source, the data further suffer from the internal background described in §3.2. According to the ordinally data reduction method (Hayashida et al. 1989), the data were selected using the following criteria to exclude or reduce the internal background:

1. The elevation angle of the LAC field of view from the earth ridge is greater than 5°, in order to exclude atmospheric scattering of solar X-rays mainly.

2. The cutoff rigidity is greater than 10 GeV, in order to reduce the background induced by the cosmic-rays.

3. The satellite position is away from the region near the SAA, in order to exclude an effect of the geomagnetically trapped charged particles. The SUD and PI counts are referred as this monitor.

4. The collimator transmission for the target is greater than 30 %.

In general, these criteria are not enough to exclude or reduce the background. If an apparent increase in background was recognized in light curves and hardness ratios of the curves, the data were excluded. This procedure was carefully performed especially for the MPC 1 and 2 data used in the spectral analysis. Finally, the data corrections for the dead time, background subtraction, and collimator response were applied to all the data. The background subtraction is described next.

4.2.2 Background Subtraction

MPC 3 Data

All the MPC 3 high-bit-rate mode data were obtained in "contact orbits" of the KSC because of the limited capacity of the BDR (§3.2). In general, the background counting rate in the contact orbits is higher than that in the remote orbits (§3.3).

In the 1987 observation, however, the background X-rays were accumulated only in remote orbits. Thus, substitute background data, pointing at $(\alpha, \delta) = (193.03, 26.18)$, were used which were taken in contact orbits before about 37 days (1987 July 2, see §3.3). The counting rate was $\sim$ 101 c/s, while that taken in the remote orbits in this observation is $\sim$ 74 c/s.

In the 1990 observation, background X-ray data were also obtained only in remote orbits, offset by $\sim 3°$ from the source. Unfortunately, there were no appropriate background data before or after about 37 or 74 days because observations with high voltage of the LAC down were not carried out so frequently. These made it impossible to subtract background correctly. Thus, the background data obtained in the remote orbits were used.

For the MPC 3 data in 1987 and 1990, the background was subtracted at a *constant* rate to investigate time variations in all the time scales less than a few hundred seconds[1].

MPC 1 & 2 Data

Data taken in these modes are used to obtain detailed information on the energy spectrum. In above $\sim$ 30 keV, counting rates of the background exceeded those of the source. Thus, more accurate subtraction of background is needed than that in the MPC 3 data.

In the 1987 observation, only MPC 2 high-bit-rate mode data were used in this analysis (Table 4.1). This is because the data in this mode have not only detailed spectral information (48 bins) but also the relatively high time resolution (62.5 ms), which are suitable for this temporal and spectral analyses. Unfortunately, the source was not observed so long in this mode because the data were obtained only in contact orbits just like the MPC 3 high-bit-rate mode data, and because the quality of energy spectra made from MPC 2 data was worse than that from MPC 1 mode data (§3.2). As a result, only 4000 sec data of Cyg X-1 had been obtained in this mode with the LAC.

In making *light curves*, the background was subtracted at a *constant* rate using the substitute background data on July 2 described previously. In producing a *energy spectrum*, the background was subtracted using a "modified Method 1", which took account of the fact that the energy spectrum of Cyg X-1 extended over higher energies and some X-rays from the source leaked into the SUD counting rate (Hayashida private communication).

In the 1990 observation, a large number of energy spectra with 48 energy bins were obtained. But only a small number of the spectra taken in remote orbits were available because of the limited SUD range of the background data. Thanks to the intense flux of Cyg X-1, however, the data have enough statistics to discuss various spectral models. The energy spectrum made from this data was obtained using the "SUD-sorting method".

[1] In the background subtraction methods of the "SUD-sorting method" and "Method 1 or 2", which were usually performed in the *Ginga* data analyses, the background counting rates were estimated at intervals of 16 or 32 sec, which could result in artificial intensity gaps in light curves.

Chapter 5

Analysis Method of the X-ray Shots

In this chapter, an analysis method of the shots, the superposition of X-ray shots, and its known systematic effects are described in detail.

5.1 Method of the Superposition of X-ray Shots

Light curves of Cyg X-1 in the 1990 observation are displayed in various time scales in Fig. 5.1. One can clearly recognize that these is a characteristic structure (time variation) with a sharp peak and wings. For instance, three events with this structure can be seen in the bottom panel of Fig. 5.1. The structure seems to be unique in any time scale by contrast with other small spike-like structures (cf., Makishima 1988). Events with the structure will be called *shots*. We focused our attention only on these shots.

To obtain an average shot profile, we superpose a number of shots as follows. Data are divided into contiguous segments with a certain duration T_m. For each segment, the local mean number of X-ray counts, $<p>$ (c/bin), is calculated. Shots are selected using the following criteria. The peak number of counts of the shot p should be larger than $2 \sim 3$ times the local mean number of counts $<p>$ (*peak criterion*), and should have the maximum intensity within a certain duration T_p on both sides (*duration criterion*). An example for $T_m = 32$ sec and $T_p = 8$ sec is shown in the forth panel from the top of Fig. 5.1. There are 8 shots with $p \geq 2.0 <p>$, which satisfies the peak criterion. But the only shot indicated by the arrow in the panel satisfies the duration criterion.

The selected shots are superposed in each energy band by aligning the peak bins. Namely, in each energy band, photon counts are accumulated in relative time bins where the peak-bin time is zero. Note that the peak-bin time is decided from curves in selecting shots, not from curves in each energy band. In this paper, shots are selected from curves in all the energy bands,

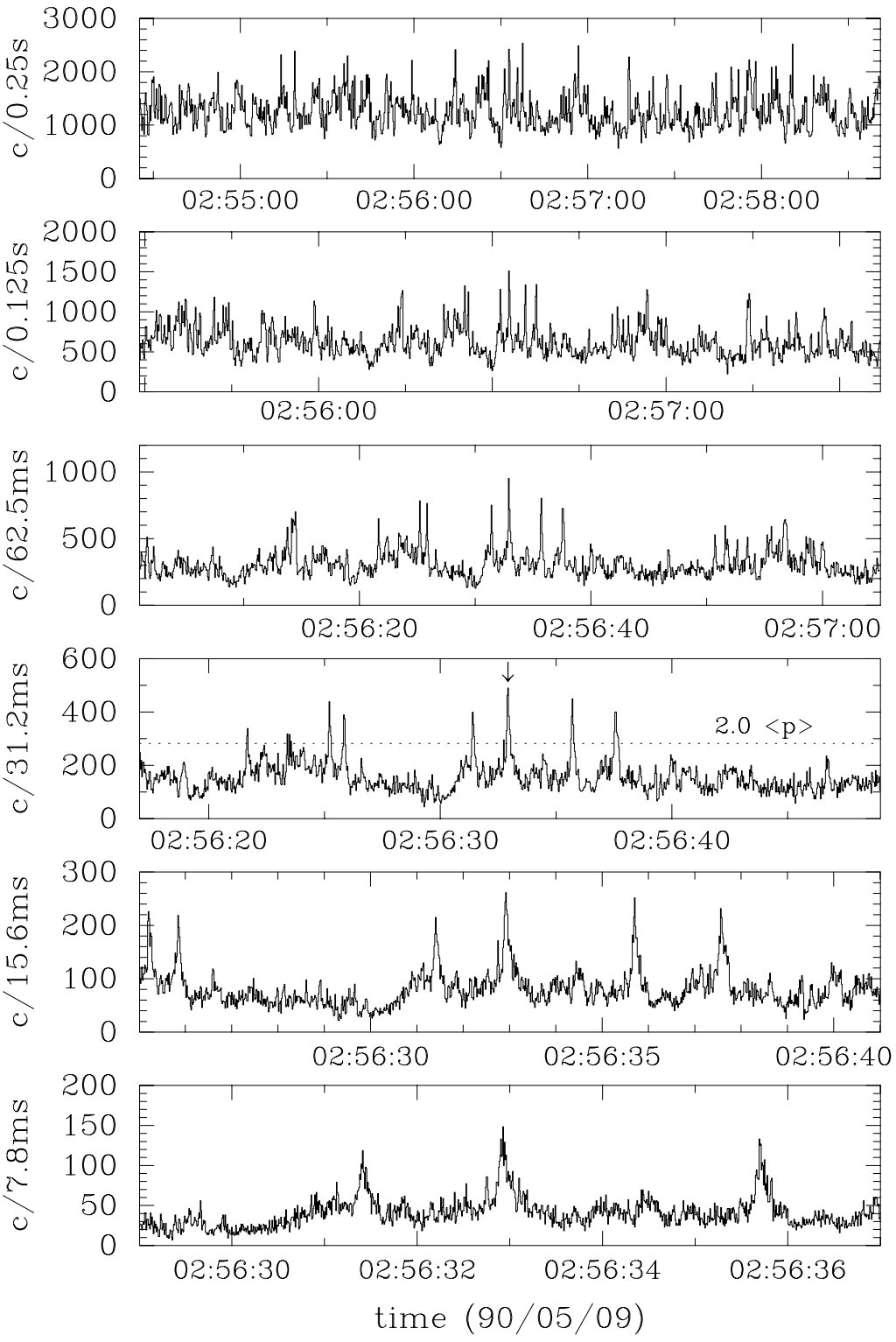

Figure 5.1: X-ray light curves of Cyg X-1 in the 1990 observation, plotted in various time scales. Note that X-ray shots with a sharp peak and wings are recognized in all the curves. The dot line in the fourth panel from the top indicates a counting rate two times larger than the local mean counting rate over 32 s (2.0 $<p>$) (see text).

i.e., the 1.2–37 keV band in 1987 and the 1.2–58 keV band in 1990, unless mentioned.

If a shot is near the beginning or end of a data segment, the segment is connected with its continuous data segment to test the duration criterion to the shot. If there is not a continuous data segment before or after the segment, the shot is abandoned to be selected. Finally, accumulated counts in each relative time bin are divided by the number of the selected shots, giving an average profile of the shots. We will call this averaged shot a "superposed shot". In some cases, criteria other than these are applied. Those criteria are mentioned if necessary.

The lengths of time to take the local mean number of counts T_m and to decide a peak bin T_p are set to be 32 and 8 sec, respectively, through this paper unless otherwise mentioned. We carefully chose these lengths so as not to have little effect on the profile of the superposed shot, but to select shots as many as possible. Systematic effects due to this technique are described next.

5.2 Systematic Effects

5.2.1 General Description

The superposed shots suffer from the following three factors; the criteria in selecting shots, the statistical count fluctuations, and a temporal distribution of the shots. The first contains T_m and T_p described in the last section, but their artificial effects can be removed if their values are carefully chosen by trial and error. (Their best values depend on a profile of the shots.) The second factor can not be avoided in principle, and only its effect is estimated in the following subsection, §5.2.2. In the subsection, some results of superposed shots are quoted beforehand to show how the count fluctuations influence properties of the superposed shots. The third factor also has an effect on obtained properties of a superposed shot, but rather represents physical background of the shots. This will be investigated in §6.1. The quantitative estimation of the effect needs much information on the shots, which appear in chapter 8.1.

5.2.2 Effects of the Count Fluctuations

The local mean counting rates in 1987 and 1990 were 109 ± 9 and 146 ± 11 count/31.25ms, respectively. In both the cases, the probability is negligible small to select a peak due to a statistical count fluctuation if we choose the shots with peak counts p larger than $1.5 <p>$ ($\gtrsim$ 5.4 (1987) and 6.0 (1990) σ levels in the Poisson statistics).

Count fluctuations near the peak bins, however, have some effects on a superposed shot profile. In selecting shots, positive count fluctuations are summed up systematically in the peak

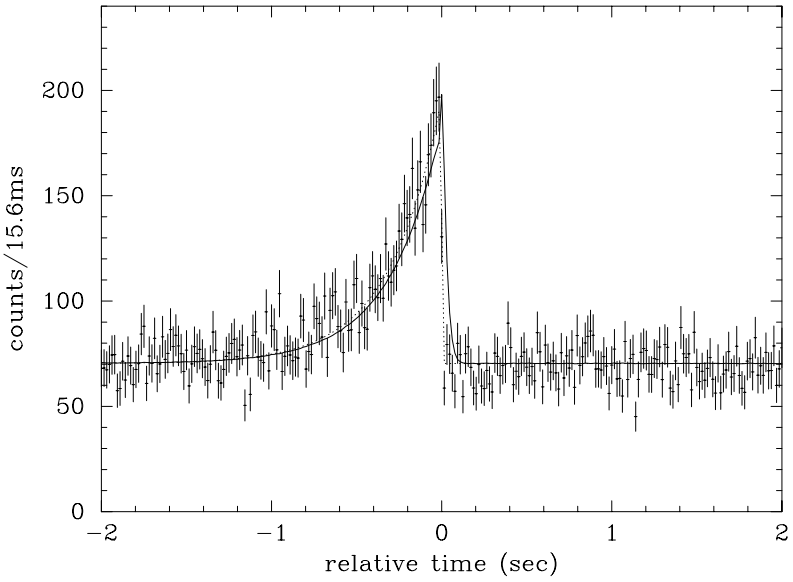

Figure 5.2: A simulated shot (points with 1 σ errors), its original one (dotted line), and the resultant superposed shot (solid line). The original profile is an exponential rise and rapid decay with the time constants of 0.3 and 0.001 sec. The superposed shot consists of ten thousand simulated shots.

bins of the shots, resulting in a systematic count increase in the peak bin of the superposed shot. If shots are selected from light curves in some energy band, a counting rate in the peak bin of the resultant superposed shot is extremely increased in the only energy band. The rate of the increase can be estimated in some ideal cases (APPENDIX A). In most cases, however, real situation is so complex that properties of peak bins of the superposed shots are not discussed.

An whole profile of a superposed shot is distorted by superposing shots aligning the peak bins which are not at their original peak positions but have the maximum counts of the shots due to the count fluctuations. To investigate this effect, we created a number of (ten thousands) light curves of a shot with an identical profile (Fig. 5.2). Assuming a counting rate similar to the observed one, count fluctuations according to the Poisson statistics and a dead time effect of the detectors were taken into account in the curves.

The following results were obtained from the simulations (Negoro et al. 1994);

1) If an original shot has a sharp peak like an exponential with a time constant less than 0.1 sec, most of selected peak bins of the simulated shots are at the original peak positions, and the resultant superposed shot has almost the same profile with the original one. 2) If an original shot has a dull peak, such as rectangular or triangular profile, most of selected peak bins are not at the original peak positions. As a result, a profile of the supposed shot except the peak

Table 5.1: PROBABILITIES OF THE PEAK POSITIONS

bin width (ms)/peak intensity†		31.3/2.00			15.6/2.35			7.8/2.60		
peak position (bin)		-1	0	+1	-1	0	+1	-1	0	+1
probability (%)	1987 data	17	63	16	20	38	21	14	21	16
	1990 data	7	84	9	15	55	24	14	31	23

†The peak intensities of simulated shots are denoted by $p/<p>$, where p is the peak number of counts of a simulated shot and $<p>= C_{\pm}$ here .

bin is smeared and far different from that of the original one. Together with the fact that the superposed shots of Cyg X-1 shown later have sharp peaks, it can be concluded that each shot of Cyg X-1 has a sharp profile like the superposed one.

Next, we pick up examples more suitable for real cases. Each simulated shot is assumed to have a profile represented by

$$I(t) = \begin{cases} A_- exp((t-t_c)/\tau_{a_-}) + B_- exp((t-t_c)/\tau_{b_-}) + C_- & ;\tau_{b_-} > \tau_{a_-} > 0 \quad (t < t_c sec) \\ A_+ exp(-(t-t_c)/\tau_{a_+}) + B_+ exp(-(t-t_c)/\tau_{b_+}) + C_+ & ;\tau_{b_+} > \tau_{a_+} > 0 \quad (t > t_c sec). \end{cases} \tag{5.1}$$

Profiles of the superposed shots of Cyg X-1 are roughly described by this function. As true parameters of the average profile of the shots are unknown a priori, profiles of some superposed shots in 1987 and 1990 are regarded as average profiles of the shots. Parameters used in the 1987 case are $A_-/B_- = 3.0$, $A_+/B_- = 3.2$, $B_+/B_- = 0.92$, $C_{\pm} = 3500$, $\tau_{a_-} = 0.125$ s, $\tau_{b_-} = 1.18$ s, $\tau_{a_+} = 0.111$ s, $\tau_{b_+} = 1.37$ s, while those in the 1990 case are $A_-/B_- = 3.5$, $A_+/B_- = 4.2$, $B_+/B_- = 0.69$, $C_{\pm} = 4500$, $\tau_{a_-} = 0.083$ s, $\tau_{b_-} = 0.72$ s, $\tau_{a_+} = 0.075$ s, $\tau_{b_+} = 1.13$ s (cf., Table 6.3). In each case, absolute peak intensity of simulated shots is set to be the minimum intensity of shots to be superposed in the real case.

Results of the simulations are summerized in Table 5.1. Only probabilities are shown that peak positions are shifted by -1, 0, +1 bins from the original ones. Due to the lower counting rate and longer duration of the simulated shots in 1987 than those in 1990, the probabilities of no shift are relatively low in 1987. Note that all the properties of the superposed shots are smeared in time by these probabilities. In general cases, it is found from the simulations that the smaller time constants $\tau_{a_{\pm}}$ of the superposed shot become $5 \sim 6$ % larger than those of the original shot, while the larger time constants $\tau_{b_{\pm}}$ become $1 \sim 2$ % larger. But, it is also found that these effect can be suppressed if a few bins nearest to peak bins are ignored as well as the peak bins.

Chapter 6

Analysis and Result of the X-ray Shots

First of all, some distributions of the shots are investigated, which provide not only physical properties of the shots but also an attention to results of the superposed shots as mentioned in §5.2.1. Next, general properties of time profiles and hardness ratios of superposed shots in 1987 and 1990 are presented. Finally, the dependence of these results on the peak intensity of the shots are examined. In the following chapter §7.1, it will be demonstrated that obtained properties of superposed shots are well consistent with results of other timing analyses.

6.1 Distributions of the X-ray Shots

6.1.1 Peak Interval Distribution

A profile of a superposed shot is not affected by a temporal distribution of the shots if they occur at random. However, the appearance of big shots tends to be suppressed for several seconds before and/or after one big event (Negoro et al. 1995).

Fig. 6.1 plots ratios of the observational peak-interval distributions of X-ray shots in the 1990 observation to the distributions expected if the shots appear at random, $f = N \exp(-\lambda t)$ with N and λ being the normalization and the average frequency. The shots were selected using the criteria of $p \geq 1.5 <p>$ (top panel), $2.0 <p>$ (middle panel) and $2.35 <p>$ (bottom panel), respectively, and $T_p = 0.25$ sec.

Real values of N and λ can not be obtained from the observations because the observational peak-interval distributions have intrinsic and systematic structures both mentioned later. Thus, the average frequencies λ were estimated by fitting the observed frequencies at large intervals 6 – 14 sec (top panel), 10 – 50 sec (middle and bottom panels), where no significant structure was

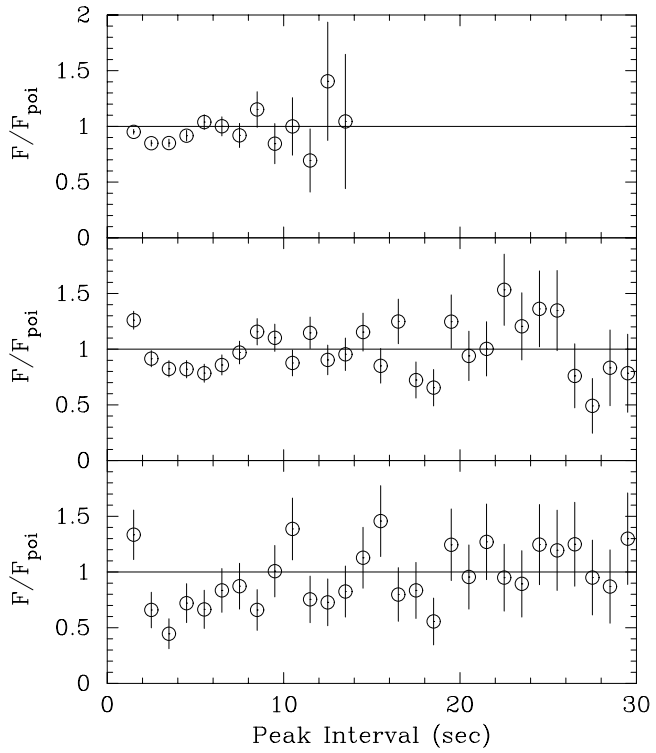

Figure 6.1: The ratios of the peak-interval distribution in 1990 to the random distribution (Negoro et al. 1995). The results for the shots with peak intensities of $p \geq 1.5 <p>$ (*top panel*), $p \geq 2.0 <p>$ (*middle panel*) and $p \geq 2.35 <p>$ (*bottom panel*) are shown. Note the shift of the local minima towards longer time intervals for larger shots.

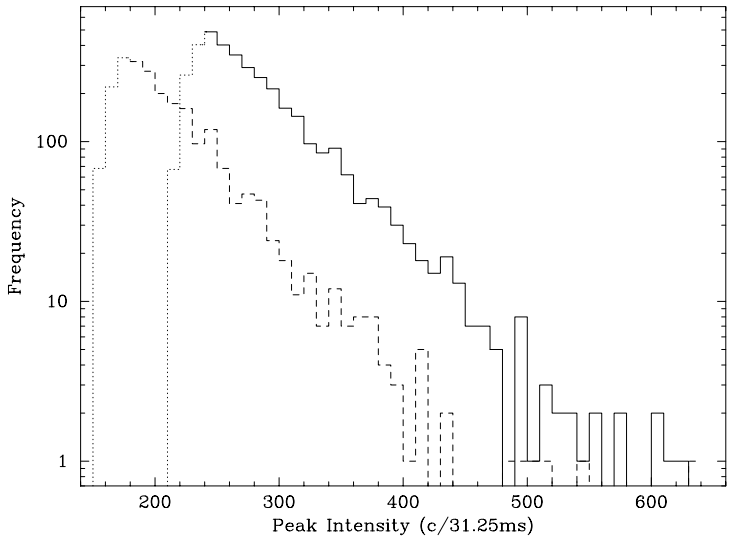

Figure 6.2: Peak-intensity distributions of shots with $p \geq 1.5 <p>$ in 1987 (dashed line) and 1990 (solid line) (Negoro et al. 1995). Because of the fluctuations of the local mean counting rates, the shots with the peak intensities below $\sim$ 180 (1987) and 240 (1990) c/31.2ms are not completely accumulated (dotted line).

recognized, with an exponential function. These fits were proceeded by the maximum likelihood technique taking account of low accumulated frequencies at larger intervals. Note that since one shot has wings with ~ 2 sec as shown later (see Fig. 6.3), peak counts of small shots overlapping the wings increase, and unexpected shots with small peak counts are selected in this procedure. Therefore, the frequencies at small intervals are enhanced. We thus focus our discussion on the parts longer than a few seconds.

It is clear in this figure that the frequencies of big events occurring within several seconds after another big event are significantly lower than those expected if fluctuations occur at random. Hereafter we call "low-frequency intervals" denoting the time intervals at which the observed distribution is below the random distribution. Moreover, this low-frequency interval is longer ($\lesssim 7$ s) for the shots with larger peaks (middle or bottom panel) than that ($\lesssim 5$ s) for the shots with smaller peaks (top panel). Note that the property of non-random distributions is rather weak when we select small shots.

The same analysis in the 1987 data also show the same tendencies. Low-frequency intervals of the shots with $p \geq 1.5 <p>$ and $p \geq 2.0 <p>$ are $\lesssim 5$ and $\lesssim 6$ or 8 sec, respectively. These results are the first evidence against the random distribution of the shots which have been long believed (e.g., Terrell 1972).

6.1.2 Peak Intensity Distribution

Next, peak-intensity distributions of the shots are investigated (Negoro et al. 1995). The results for the shots with $p \geq 1.5 <p>$ are shown in Fig. 6.2 by dotted (1987) and solid (1990) lines. As local mean counting rates $<p>$ in 1987 increased by about 30 % during the observation, we only used the data before the increase, and shots were selected from the data with similar distributions of the mean counting rates ($100 \leq <p> < 120$) in order to evaluate the distribution correctly.

$<p>$ in 1990 also fluctuated such as 149.6 ± 7.7 c/bin on May 9th, 137.2 ± 9.1 c/bin on May 10th and 151.4 ± 9.4 c/bin on May 11th. Similarly, the only data on May 9th and 11th with similar distributions of the mean counting rates ($140 \leq <p> < 160$) were used. In this case, frequencies of the peak counts less than 180 c/bin (1987) and 240 c/bin (1990) were not completely accumulated (dotted lines).

With these incomplete sampling regions omitted, the distributions can be described by an exponential function. Obtained parameters in the fits with the exponential function depend on the peak criteria T_p as summerized in Table 6.1. This is because, if T_p is set to be larger, small

Table 6.1:
BEST-FITTING PARAMETERS OF THE PEAK-INTENSITY DISTRIBUTION[a]

T_p (sec)	fitting region (c/bin[b])	N ($\times 10^3$ bin[b]/c[c])	p_{decay} (c/s)
	1987		
0.25	180-640	4.2 ± 0.5	1314 ± 27
0.25	250-640	1.8 ± 0.6	1467 ± 70
0.50	180-640	2.0 ± 0.2	1451 ± 35
0.50	250-640	1.2 ± 0.4	1544 ± 80
	1990		
0.25	240-630	10.5 ± 1.1	1545 ± 26
0.25	350-630	5.3 ± 2.2	1684 ± 95
0.50	240-630	5.3 ± 0.6	1688 ± 32
0.50	350-630	5.0 ± 2.2	1690 ± 97

a The assumed distribution form is $f(p) = Nexp(-p/p_{decay})$.
b The bin width used is 31.25 ms.
c Accumulated time in 1987 and 1990 is 5344 and 8320 sec, respectively. Note that a part of the accumulated time is lost in selecting shots

peaks within T_p are ignored by the definition, and frequencies at smaller peak intensities are suppressed. Inversely, if T_p is set to be smaller, numerous smaller peaks overlapping the wings of other shots are picked up and frequencies at smaller peak intensities are enhanced. However, it should be noted that the decay constants p_{decay} are in the range of 1450 ± 100 c/s (1987) and 1600 ± 100 c/s (1990) in all the cases, and that the constants are free from contributions from numerous small shots and/or a steady emission component to each peak count.

From these distributions, one should bear in mind that properties of the superposed shots within several seconds from the peaks may be influenced by the non-random distribution of the shots. In §8.2, using these distributions and other relations, we show that the suppression of the shot appearance may reduce intensity of the superposed shot at the low-frequency intervals by a few percents.

6.2 Time Profiles

6.2.1 General Profiles

Figure 6.3 shows a sample of superposed shots in the 1987 and 1990 observations. There have been no definitive functions to describe these profiles because no physical models to explain the shots have been established. To discuss the profiles quantitatively, they are represented with

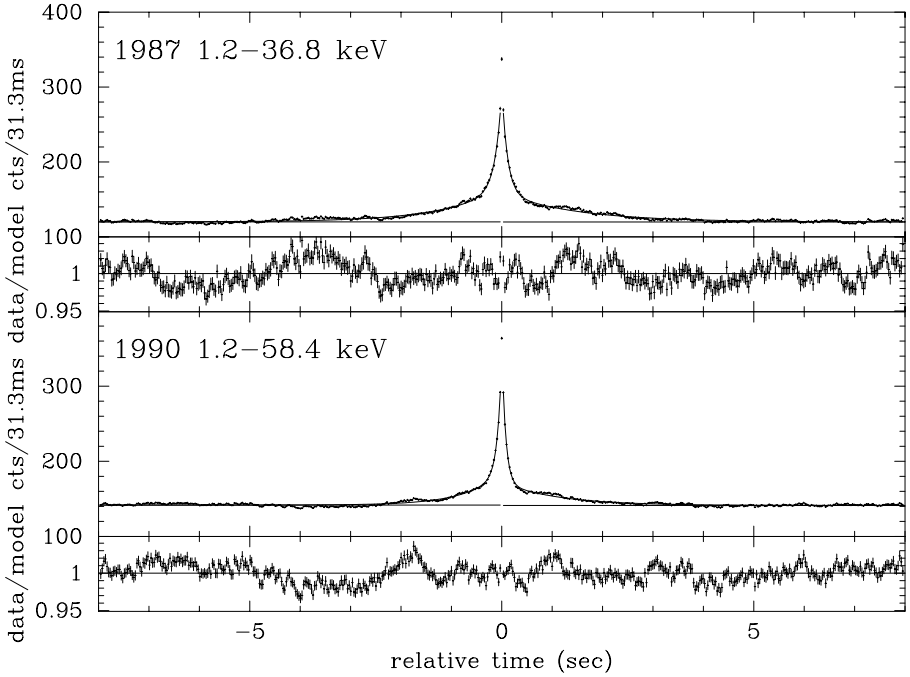

Figure 6.3: Average profiles of shots in the 1987 observation (*upper panel*) and in the 1990 observation (*lower panel*). 541 (1987) and 872 (1990) shots with $p \geq 2.0 < p >$ are superposed by aligning their peaks, and their average profiles are shown. The best-fitting models with a sum of two exponentials plus a constant component and the constant components are indicated by the solid lines. Count ratios of the data to the model are also shown below the data.

two empirical models, a sum of two exponential function and a "fractal" function. Both the models can roughly represent the profiles to the same extent. The exponential model is utilized for convenience and for the following reasons: (1) it is easy to compare this results with those of previous shot noise models (§2.3.2), in which the shots have been represented by an exponential, sometimes some exponentials. (2) some physical model has demonstrated exponential profiles of the shots (§10.4.1). The fractal model is newly introduced, and its physical interpretation will be discussed in §10.4.3.

Exponential Function Fit

The profiles of the superposed shots for 8 sec before and after the peaks are fitted with one exponential rise/decay model, but the model poorly represents both of them (reduced $\chi^2 \geq 15$). Next, the sum of 2 exponentials model (Eq. 5.1 with $t_c = 0$) is applied, and able to roughly represent them as shown in Fig. 6.3 (Negoro et al. 1994). The first terms on the right hand side of Eq. 5.1 present the sharp profiles near the peaks and the second terms stand for the wings lasting for $4 \sim 5$ sec (1987) or $2 \sim 4$ sec (1990) on both sides. The best-fitting parameters for

Table 6.2:
THE BEST-FITTING PARAMETERS WITH THE TWO EXPONENTAIL MODEL

RISE PHASE (1987)						
data† (bin width)	$A_-[c/s]$	$\tau_{a_-}[s]$	$B_-[c/s]$	$\tau_{b_-}[s]$	$C_-[c/s]$	χ^2_ν (d.o.f.)
(15.6 ms)	3973 ± 50	0.125 ± 0.003	1310 ± 24	1.18 ± 0.02	3544 ± 3	2.96(506)
(31.2 ms)	4140 ± 71	0.128 ± 0.004	1446 ± 32	1.18 ± 0.03	3840 ± 3	3.38(250)
DECAY PHASE (1987)						
data† (bin width)	$A_+[c/s]$	$\tau_{a_+}[s]$	$B_+[c/s]$	$\tau_{b_+}[s]$	$C_+[c/s]$	χ^2_ν (d.o.f.)
(15.6 ms)	4175 ± 54	0.111 ± 0.002	1210 ± 18	1.37 ± 0.03	3558 ± 3	2.42(506)
(31.2 ms)	4520 ± 77	0.112 ± 0.003	1250 ± 22	1.47 ± 0.04	3837 ± 4	2.86(250)
RISE PHASE (1990)						
data† (bin width)	$A_-[c/s]$	$\tau_{a_-}[s]$	$B_-[c/s]$	$\tau_{b_-}[s]$	$C_-[c/s]$	χ^2_ν (d.o.f.)
(15.6 ms)	5509 ± 59	0.083 ± 0.002	1405 ± 29	0.76 ± 0.02	4555 ± 2	2.58(506)
(31.2 ms)	4956 ± 77	0.083 ± 0.002	1404 ± 35	0.72 ± 0.02	4543 ± 2	4.71(250)
DECAY PHASE (1990)						
data† (bin width)	$A_+[c/s]$	$\tau_{a_+}[s]$	$B_+[c/s]$	$\tau_{b_+}[s]$	$C_+[c/s]$	χ^2_ν (d.o.f.)
(15.6 ms)	6213 ± 63	0.075 ± 0.001	952 ± 15	1.25 ± 0.03	4531 ± 3	2.68(506)
(31.2 ms)	5886 ± 84	0.075 ± 0.001	974 ± 18	1.13 ± 0.03	4525 ± 3	2.88(250)

† The shots with $p \geq 2.35 <p>$ (15.6 ms) and $2.00 <p>$ (31.2 ms) are used in the superpositions. The numbers of the shots are 499 (1987, 15.6 ms), 541 (1987, 31.2 ms), 692 (1990, 15.6 ms) and 872 (1990, 31.2 ms).

the superposed shots, obtained from the data binned into 15.6 ms and 31.3 ms, with this model are summarized in Table 6.2. Shots selected from the 15.6 ms data are not always the same ones from the 31.3 ms data, resulting in the difference between the intensity parameters, $A_\pm, B_\pm$ and $C_\pm$, in the 15.6 ms data and those in the 31.3 ms data. However, it should be noted that all the time constants hardly depend on the time resolutions of the data ($\Delta\tau_a \sim 1\%$, $\Delta\tau_b \sim 5\%$).

The time constants in 1987 are $30 \sim 60$ % larger than those in 1990. A ratio of the wing components to the sharp components in 1987, which can be roughly evaluated by $(\tau_{b_-}B_- + \tau_{b_+}B_+)/(\tau_{a_-}A_- + \tau_{a_+}A_+)$, is about $30 \sim 40$ % larger than that in 1990. These mean that the shot profile is not peculiar to the source. However, it is interesting that, in spite of these differences, time symmetric profiles are recognized in both the superposed shots; $(\tau_{a_-}A_- + \tau_{b_-}B_-)/(\tau_{a_+}A_+ + \tau_{b_+}B_+) = 0.96 \pm 0.03$ in 1987 and 0.92 ± 0.03 in 1990.

Fractal Function Fit

These time profiles are also roughly represented by a following simple function,

$$I(t) = \begin{cases} A_-/(\tau_{f_-} - t)^{\alpha-} + C_- & (t < 0sec) \\ A_+/(\tau_{f_+} + t)^{\alpha+} + C_+ & (t > 0sec). \end{cases} \tag{6.1}$$

Table 6.3:
THE BEST-FITTING PARAMETERS WITH THE FRACTAL FUNCTION MODEL

RISE PHASE (1987)					
data† (bin width)	$A_-[c/s]$	$\tau_{f_-}[s]$	α_-	$C_-[c/s]$	χ^2_ν (d.o.f.)
(15.6 ms)	719 ± 10	0.070 ± 0.004	0.810 ± 0.017	3382 ± 8	2.80(507)
(31.2 ms)	805 ± 12	0.069 ± 0.006	0.794 ± 0.021	3652 ± 12	3.13(251)
DECAY PHASE (1987)					
data† (bin width)	$A_+[c/s]$	$\tau_{f_+}[s]$	α_+	$C_+[c/s]$	χ^2_ν (d.o.f.)
(15.6 ms)	760 ± 12	0.036 ± 0.003	0.663 ± 0.014	3345 ± 10	3.55 (507)
(31.2 ms)	862 ± 18	-0.020 ± 0.003	0.600 ± 0.016	3570 ± 16	4.47(251)
RISE PHASE (1990)					
data† (bin width)	A_-[c/s]	$\tau_{f_-}[s]$	α_-	$C_-[c/s]$	χ^2_ν (d.o.f.)
(15.6 ms)	413 ± 6	0.069 ± 0.003	1.093 ± 0.019	4490 ± 4	3.53(507)
(31.2 ms)	375 ± 6	0.084 ± 0.005	1.180 ± 0.028	4486 ± 5	6.67(251)
DECAY PHASE (1990)					
data† (bin width)	$A_+[c/s]$	$\tau_{f_+}[s]$	α_+	$C_+[c/s]$	χ^2_ν (d.o.f.)
(15.6 ms)	444 ± 6	0.021 ± 0.002	0.805 ± 0.013	4441 ± 6	4.88(507)
(31.2 ms)	446 ± 9	-0.010 ± 0.002	0.762 ± 0.015	4411 ± 7	5.70(251)

† see. Table 6.2.

This function will be called a fractal function because a PSD of this function with $\tau = 0$ and $\alpha = 1/2$ is proportional to $1/\nu$ where ν is the frequency (Press 1978; §7.1.1). These fitting results are shown in Table 6.3. Count ratios of the data to the model in this fits are very similar to those in the exponential fits except rations at the relative time of $0 \sim 1$ sec (cf., Fig. 6.3). The ratios in that region are much lower than those in the exponential fits.

It is found in χ^2 that this function better represents the rise profiles than the decay ones, and that the rise profile in 1987 is better fitted with this function than the exponential function. As the wing component in the decay phase varies in time as shown later, this one-component function is unlikely to be suitable to represent the decay profiles. Note that τ_{f_-} in 1987 is similar to that in 1990 ($\Delta\tau_{f_-} \sim 10$ %) by contrast with the time constants in the exponential fits. It is interesting that τ_{f_-} in 1990 in this fit is similar to τ_{a_-} in 1990 in the exponential fit. While α_- varies by 20–30 % between the two observations.

Mathematically, these consistency and difference in the fits with the two models are understood as follows. For small $|t|$ ($< \tau_{a_-}, \tau_{f_-}$), these model functions are expanded as $exp(t/\tau_{a_-}) = 1 + t/\tau_{a_-} + (t/\tau_{a_-})^2/2 + \cdots$, and $(1 - t/\tau_{f_-})^{-\alpha_-} = 1 + \alpha_- t/\tau_{f_-} + \alpha_-(\alpha_- + 1)(t/\tau_{f_-})^2/2 + \cdots$. Thus, as $\alpha \simeq 1$ in 1990, the time constants τ_{a_-} and τ_{f_-} show similar values. Furthermore, α_- in 1987 is smaller than that in 1990 instead of the larger value of τ_{a_-} in 1987 than that in 1990.

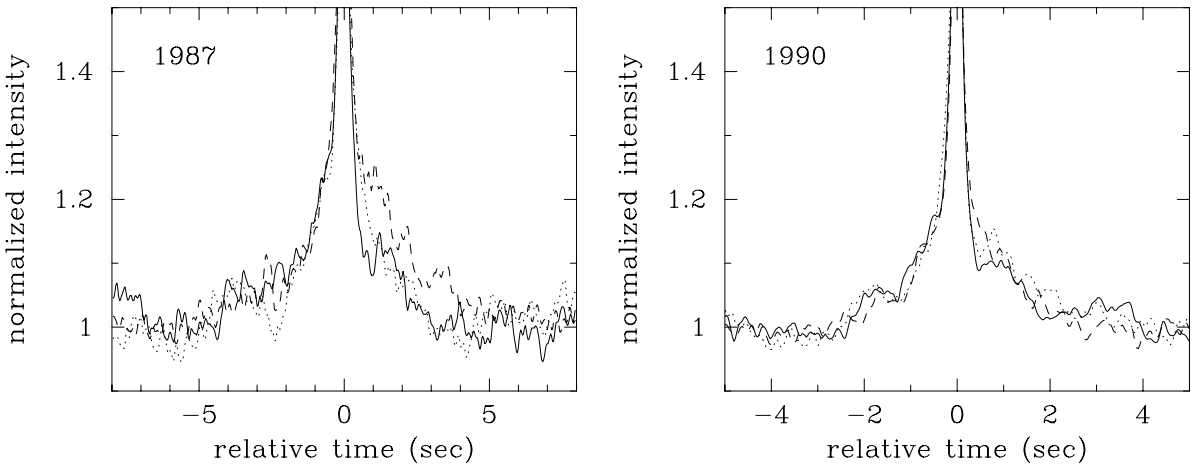

Figure 6.4: Average profiles of shots with $p \geq 2.0 <p>$ obtained from data divided in time. All these superposed shots are normalized by average counts on both sides, and smoothed by an average of adjoining five bins with the weights of 1, 2, 3, 2, 1. Local fluctuations are due to other shots than the shots superposed. Sizes of 1 σ errors before smoothing are smaller than the local fluctuations. (*left*) The number of shots superposed and observational time are 131 and 1987/08/06 11h50m - 13h28m (solid line), 111 and 13h30m - 15h10m (dotted line), and 151 and 17h09m - 18h47m (dashed line). The data during 15h39m - 17h06m are not shown. (*right*) 279 and 1990/05/09 01h44m - 06h35m (solid line), 277 and 05/09 23h45m - 05/10 06h28m (dotted line), and 316 and 05/10 21h49m - 05/11 04h20m (dashed line).

Time Variation

Superposed shots in each observation exhibit different profiles on time scales of a few hours or less. Figure 6.4 shows superposed shots accumulated at intervals of a few hours in 1987 and 1 day in 1990. The small number of shots superposed in 1987 causes large local fluctuations in the resultant superposed curve. Obviously, the profiles before the peaks are steady in all the observations, while those after the peaks are quite changeable. However, profiles of superposed shots in 1990 accumulated at intervals of a few hours do not greatly change both before and after the peak. Also note that the profiles after the peaks also depend on the peak intensities of shots, which will be shown in §6.4.

Sub-Structures

The superposed shots have a few structures unable to be represented by both the models as one can see in the ratios of the data to the model in Fig. 6.3. Some of them are obvious and always appear at the same positions of all the superposed shots (cf., Fig. 6.4). Hereafter we call them "sub-structures". Sub-structures of the superposed shot in 1987 are a slight (∼

Table 6.4:
THE BEST-FITTING PARAMETERS
WITH THE FRACTAL FUNCTION PLUS GAUSSIAN MODEL

Data[a] (Bin Width)	Fractal			$C_-[c/s]$			
	$A_-[c/s]$	$\tau_{a-}[s]$	α_-				
1987 (31.25 ms)	970 ± 25	0.048 ± 0.005	0.66 ± 0.02	3480 ± 24			
	394 ± 26	0.16 ± 0.09	1.46 ± 0.72	3746 ± 57			
1990 (31.25 ms)	653 ± 20	0.025 ± 0.003	0.72 ± 0.02	4202 ± 18			
	323 ± 42	0.11 ± 0.02	1.38 ± 0.16	4412 ± 21			
Gaussian[b]			Gaussian[b]			χ^2_ν (d.o.f.)	
t_c [s]	t_w [s]	Total Cnts [c]	t_c [s]	t_w [s]	Total Cnts [c]		
-3.48 ± 0.04	0.57 ± 0.05	183 ± 20	—	—	—	1.65(185)	
-3.57 ± 0.07	0.90 ± 0.09	446 ± 93	-0.64 ± 0.45	0.88 ± 0.31	951 ± 736	1.31(182)	
-1.81 ± 0.02	0.23 ± 0.02	81 ± 9	—	—	—	2.29(121)	
-1.77 ± 0.02	0.36 ± 0.02	191 ± 19	-0.74 ± 0.02	0.25 ± 0.03	167 ± 28	0.95(118)	

a see. Table 6.2.
b The gaussian function is represented by $N\,exp(-(t-t_c)^2/2t_w^2)$ with total counts $\sqrt{2\pi}Nt_w$.

2 %) decrease of the intensity at the relative time of -7 to -5 sec and a followed broad bump around -3.7 sec. However, these are obviously recognized in the only superposed shot created from data from 13h30m to 15h10m in August 6 (dotted line in the left panel of Fig. 6.3). It is confirmed that these structures always appeared through this short data, and that they are slightly recognized in a superposed shot produced from the sum of the other data.

While, the superposed shot in 1990 has rigid sub-structures in the rise phase. There are a long, and slight ($\sim$ 2 %) intensity decrease of the intensity at the relative time of -5 to -2 sec and a bump around -1.8 sec, not recognized in the superposed shot in 1987. Both are recognized in all the superposed shots in 1990 (right panel in Fig. 6.4).

These intensity decrease before the peak in 1987 and 1990 can be interpreted by the temporal distribution of the shots as shown in §8.2. While, the bump structures do not arise from the temporal distribution of the shots, the criteria to select shots, nor the difference of the energy bands between the superposed shot in 1987 and that in 1990. Because both the superposed shots are produced by the same superposition method with the same criteria, and the contribution of 37.1-58.4 keV X-ray counts to the total X-ray counts is only 0.5 %.

Taking account of these sub-structures, the rising profiles for 6 sec (1987) and 4 (1990) sec before the peaks are fitted with the fractal function plus one or two additional Gaussian model, and their best-fitting parameters are summarized in Table 6.4. The only fractal function fits are shown in relation to §10.4.3. Note that, in the case of one additional gaussian, α_- in 1987 become similar to that in 1990 ($\simeq 0.7$), and τ_{a-} in 1987 is about two times larger than that in

1990.

No rigid sub-structure is recognized in the decay phase because the whole profile itself is not steady. However, it should be noted that the profiles exhibit knee like structures at the relative time $\sim$ 1.5 sec in 1987 and $\sim$ 1 sec in 1990. Those make it hard to represent the decay profiles by both the models. Is should be also noted that slight intensity decreases are also recognized after the peak intensity.

6.2.2 Energy Dependence

Figure 6.5 shows time profiles of the superposed shots divided into some energy ranges. First, one can notice that they are very similar each other. The time coincidence of the peak bins is due to the count increase in the peak bins by the count fluctuations (§5.2.2), and they are not plotted in the figure. However, even if shots are selected from curves in the lowest energy band (1.2 – 2.6 keV in 1987, 1.2 – 3.7 keV in 1990), no significant time lags of peak bins in higher energy bands are recognized.

Their rise and decay profiles are also represented by the sum of two exponentials, and their best-fitting parameters are summaried in Table 6.5. To avoid the effect of the count fluctuations, we use the superposed shots binned into 31.25 ms in the fits (see Table 5.1). Moreover, for the superposed shots in 1987, both side bins of the peak bins are ignored because they are thought to be much affected by rapid spectral hardening at the peak intensity as shown later (cf., §5.2.2). Note that all the time constants scarcely depend on the energy. But the large decay time constant τ_{b_+} in 1987 and the small decay time constant τ_{a_+} in 1990 has slightly ($\sim$ 10 %) energy dependence. It has a larger value in a higher energy band. The rise time constants τ_{a_-} and τ_{b_-} in the 23.0-36.8 keV band in 1987 also show extremely smaller values compared with those in the lower energy bands, which can be seen in Fig. 6.2.2.

The broad bump before 3.6 sec from the peak in 1987 is recognized in all the energy bands though its energy dependence is not clear because of the poor statistics (Fig. 6.5). On the other hand, the small bump before 1.8 sec from the peak in 1990 is not apparently observed in the 21.9-58.4 keV bands. (The addition of the Gaussian does not provide a significantly improvement in χ^2.) This suggests that the small bump has a soft energy spectrum. In both the superposed shots, the small bumps at the relative time -0.8 sec seem to be clearer in higher energy bands. These become clearer by calculating hardness ratios of the superposed shots.

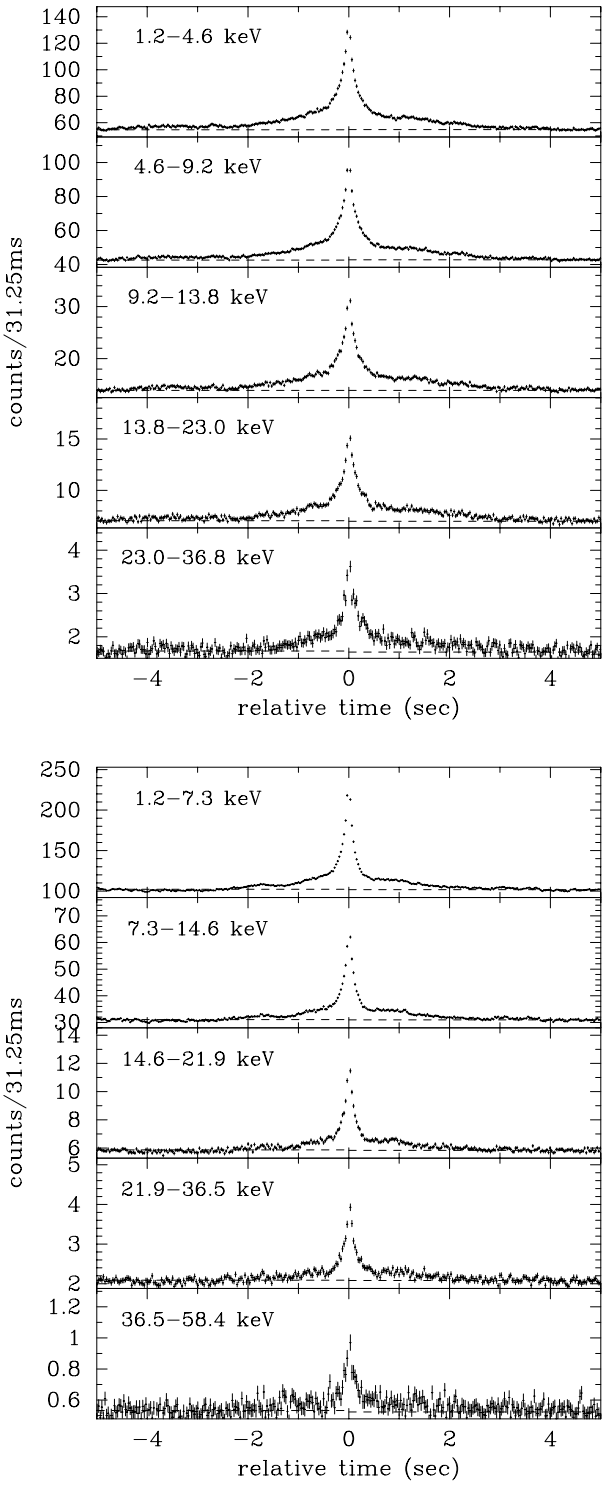

Figure 6.5: Average shot profiles in different energy bands in 1987 (*upper*) and 1990 (*lower*). They are obtained by superposing 541 and 872 shots with $p \geq 2.0 < p >$, respectively. The constant components, C_- and C_+, are indicated by dashed lines. The peak-bin counts suffering from the statistical count fluctuation are not plotted.

Table 6.5:
ENERGY DEPENDENCE OF THE SHOT PARAMETERS (TWO EXPONENTIAL FITS)

1987						
RISE PHASE						
energy band [kev]	$A_-[c/s]$	$\tau_{a_-}[s]$	$B_-[c/s]$	$\tau_{b_-}[s]$	$C_-[c/s]$	χ^2_ν
1.2 – 4.6	1870 ± 71	0.146 ± 0.008	665 ± 26	1.26 ± 0.05	1750 ± 3	1.40
4.6 – 9.2	1311 ± 48	0.149 ± 0.008	464 ± 20	1.24 ± 0.06	1363 ± 2	1.38
9.2 – 13.8	362 ± 19	0.148 ± 0.012	149 ± 9	1.22 ± 0.07	444.8 ± 0.9	1.45
13.8 – 23.0	177 ± 12	0.145 ± 0.016	168 ± 25	1.23 ± 0.10	225.5 ± 0.6	1.36
23.0 – 36.8	47 ± 15	0.083 ± 0.029	80 ± 28	0.81 ± 0.13	53.5 ± 0.3	0.97
DECAY PHASE						
energy band [kev]	$A_+[c/s]$	$\tau_{a_+}[s]$	$B_+[c/s]$	$\tau_{b_+}[s]$	$C_+[c/s]$	χ^2_ν
1.2 – 4.6	1948 ± 91	0.118 ± 0.007	579 ± 19	1.43 ± 0.06	1753 ± 3	1.12
4.6 – 9.2	1474 ± 62	0.122 ± 0.006	428 ± 13	1.52 ± 0.06	1361 ± 2	1.30
9.2 – 13.8	474 ± 26	0.118 ± 0.008	142 ± 5	1.55 ± 0.08	445.0 ± 1.1	1.35
13.8 – 23.0	246 ± 16	0.118 ± 0.009	69 ± 3	1.68 ± 0.12	223.6 ± 0.8	1.35
23.0 – 36.8	42 ± 5	0.176 ± 0.035	15 ± 2	1.77 ± 0.38	52.7 ± 0.5	1.05
1990						
RISE PHASE						
energy band [kev]	$A_-[c/s]$	$\tau_{a_-}[s]$	$B_-[c/s]$	$\tau_{b_-}[s]$	$C_-[c/s]$	χ^2_ν
1.2 – 7.3	3811 ± 72	0.084 ± 0.003	1085 ± 33	0.71 ± 0.02	3270 ± 2	2.94
7.3 – 14.6	914 ± 24	0.084 ± 0.004	254 ± 11	0.75 ± 0.03	993.9 ± 0.8	2.16
14.6 – 21.9	165 ± 8	0.075 ± 0.007	48 ± 4	0.64 ± 0.05	187.7 ± 0.3	1.69
21.9 – 36.5	46 ± 4	0.093 ± 0.015	13 ± 2	0.77 ± 0.14	66.8 ± 0.2	1.21
36.5 – 58.4	12 ± 3	0.078 ± 0.031	3.0 ± 1.1	0.90 ± 0.37	1.70 ± 0.12	0.99
DECAY PHASE						
energy band [kev]	$A_+[c/s]$	$\tau_{a_+}[s]$	$B_+[c/s]$	$\tau_{b_+}[s]$	$C_+[c/s]$	χ^2_ν
1.2 – 7.3	4366 ± 80	0.074 ± 0.002	724 ± 17	1.11 ± 0.03	3257 ± 3	1.81
7.3 – 14.6	1213 ± 27	0.078 ± 0.002	196 ± 6	1.17 ± 0.05	991.1 ± 1.0	1.73
14.6 – 21.9	218 ± 9	0.077 ± 0.004	37 ± 2	1.14 ± 0.08	186.8 ± 0.3	0.99
21.9 – 36.5	68 ± 5	0.082 ± 0.008	13.1 ± 1.4	1.10 ± 0.15	66.6 ± 0.2	1.06
36.5 – 58.4	14 ± 3	0.092 ± 0.023	2.9 ± 0.5	1.88 ± 0.70	16.8 ± 0.2	0.87

6.3 Hardness Ratios

6.3.1 Hardness Ratios

Hardness ratios of the superposed shots in 1987 and 1990 have almost the same characters (Fig. 6.6). The ratios gradually decrease from at least 1 sec before the peak intensity, and show the lowest values just before the peak intensity. After the peak intensity, they rapidly increase, but remaining lower than or equal to the average values. More detailed descriptions will be made in the next subsection.

These results lead that the shots have a softer energy spectrum than all the X-rays observed, and that the other component with a harder spectrum is necessary to reproduce the observed energy spectrum. The other component must have a smaller time variation than the shots because it could not be selected in the superposition method. We will then call it a steady component which may be identical with what have been introduced in the shot noise models

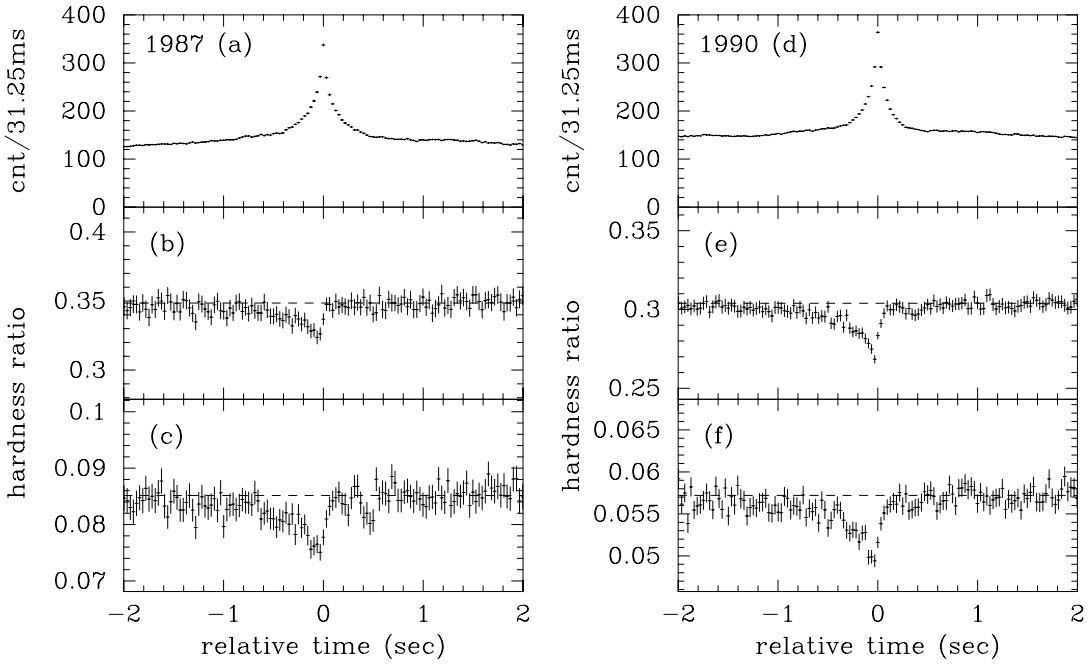

Figure 6.6: Average shot profile and hardness ratios in 1987 (*left*) and 1990 (*right*). These are the same superposed shots shown in Fig. 6.5. Corresponding energy ranges are (a) 1.2 – 36.8 keV (b) 6.9 –13.8 keV/1.2 – 6.9 keV (c) 13.8 – 23.0 keV/1.2 – 6.9 keV (d) 1.2 – 58.4 keV (e) 7.3 – 14.6 keV/1.2 – 7.3 keV (f) 14.6 – 21.9 keV/1.2 – 7.3 keV. Time averaged hardness ratios of all the X-rays are shown by the dashed lines.

(Sutherland et al. 1977).

The soft energy spectrum of the shots is not an artificial result arising from the superposition technique. Even if shots were selected from curves in higher energy bands, a similar result was obtained. Furthermore, a cross correlation between intensity in the hard X-ray band ($14.6 \sim 58.4$ keV) and its ratio to intensity in the lower energy ($1.2 \sim 14.6$ keV) band indicates negative values at the lag time of $-5 \sim -3$ sec (the hardness ratio advances) to about 1 sec (the intensity advances). This negative correlation is consistent with an expected one between those in the superposed shot.

6.3.2 Hardness Ratios of the Excess Shot Component

Here we define an "excess shot component", which is excess counts above the baseline counts. Considering the extension of the shots, the baseline counts in 1987 were estimated from average counts in the regions apart from the peak intensity by 6-8 sec (indicated by the dashed line in the top panel of Fig. 6.7). Those in 1990 were obtained from the regions apart from the peak intensity by 4-8 sec because of their smaller wings. This excess shot component

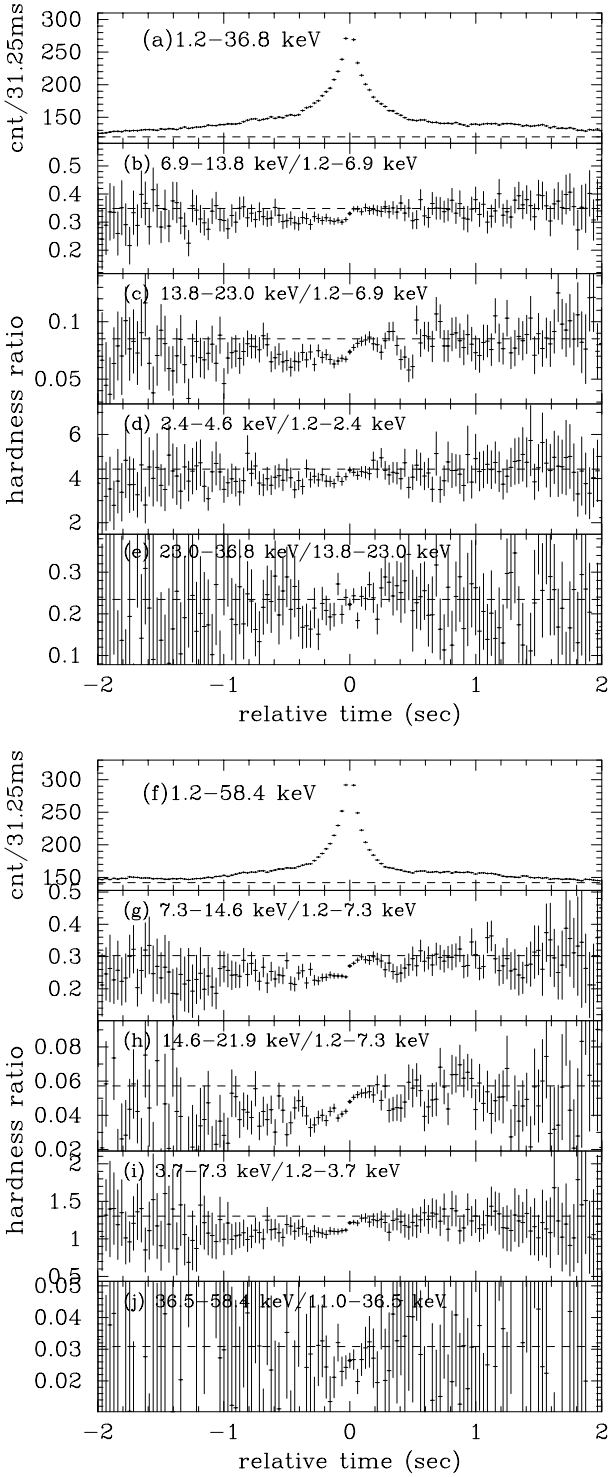

Figure 6.7: The time profile of the superposed shot shown in Fig. 6.5 and hardness ratios of the excess shot components in 1987 (*upper*) and 1990 (*lower*). The baseline counts defining the excess shot component and time averaged hardness ratios of all the X-rays are indicated by the dashed line. Vertically plotted ranges in the ratios are a factor of 1/3 to 5/3 of the averaged ratios.

essentially corresponds to the exponential parts of Eq. (5.1), and the baseline counts are the same as the constant component of Eq. (5.1) with accuracy of less than 1%. Such a separation of the excess shot component and the other components is very useful to investigate spectral changes of the excess shot component in detail. But one must recall that their values may be slightly influenced by the temporal shot distribution (§6.1.1). Namely, if the real baseline counts are below the observed ones due to the suppression of neighboring shots, intrinsic ratios of the shots themselves can not be estimated. One should also notice that the other component, a "subtracted component", consists of the other shots and the steady component.

Hardness ratios of the excess shot components are shown in Fig. 6.7. Acceptable linear fits with the function, $ratio(t) = at + b$ $(-2.0 \leq t(s) < 0.0)$ where t is the relative time, show that the ratios except (e) are consistent with constants, i.e., $a \simeq 0$, and significantly lower than the average ones of all the X-rays. Obtained b and corresponding average ratios of all the X-rays are (b) 0.305 ± 0.004 and 0.353, (c) 0.067 ± 0.001 and 0.085, (d) 4.00 ± 0.06 and 4.43, (f) 0.237 ± 0.003 and 0.304, (g) 0.041 ± 0.001 and 0.057, (h) 1.10 ± 0.02 and 1.30, and (i) 0.025 ± 0.002 and 0.031. But the ratio of the intensity in the 23.0-36.8 keV band to others (cf., (e) in the Fig. 6.7) suggests a spectral hardening, $a = 0.044 \pm 0.020$ and $b = 0.22 \pm 0.01$. Such a exception in high energy bands is not recognized in ratios in the superposed shot in 1990. These are consistent with the fitting results. The ratios of (c) and (g) in Fig. 6.7 show the slight increase at the relative time around -0.8 sec, indicating the small bump before ~ 0.8 sec from the peak has a hard spectrum.

At the peak intensity, the hardness ratios dramatically harden. This rapid spectral change in 1990 is clear than that in 1987. This spectral change is worth investigating more for purposes of knowing the physical time scale and preventing readers from misreading the data. Figure 6.8 shows an excess shot component and its hardness ratios of a superposed shot in 1990 obtained from data binned into 7.8 ms. Continuous spectral changes, on a time scale of 30-50 ms, near the peak intensity are recognized, but one must remind that some shots are superposed by aligning the peak bins which are not at their original peak positions (§5.2.2). According to the probability of peak positions as shown in §5.2.2, hardness ratios of a simulated superposed shot with the same profile as the observed one are calculated. Hardness ratios of each simulated shot before and after the peak intensity are assumed to have different constant values similar to the real ones. At the peak intensity, an average value in the ratios before and after the peak is assumed. Count fluctuations for the ratios are not taken into account. Resultant hardness ratios are denoted by the solid lines in the same figure, indicating that the ratios continuously change on the time scale of 50 ms and well trace the real ones. Thus, it can be concluded that

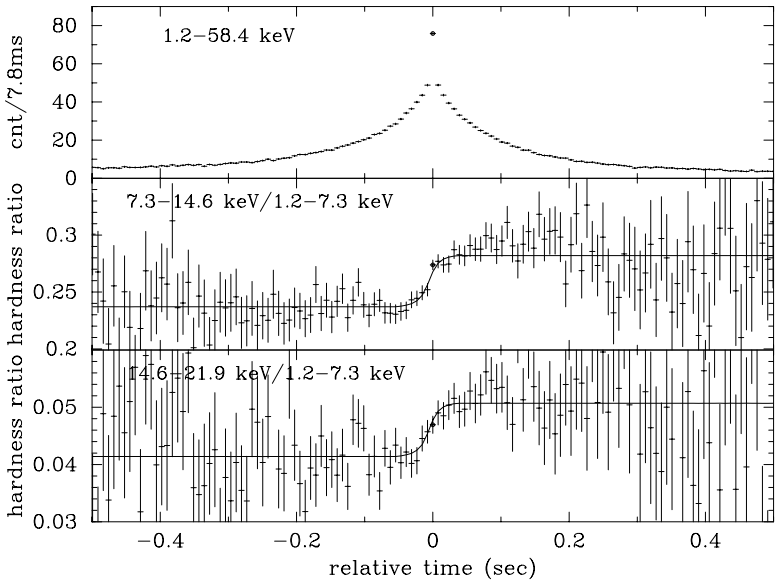

Figure 6.8: An excess shot component of a superposed shot in 1990 obtained from data binned into 7.8 ms and hardness ratios of the excess shot components. In this case, $T_p = 4$ sec, and the superposed shot are obtained from 937 shots with $p \geq 2.6 < p >$. The solid lines in the middle and lower panels are ratios expected by superposing shots with different, constant values before and after the peak intensity. The continuity of the solid lines near the peak intensity is due to count fluctuations (see text). The count fluctuations also have a great effect on the peak counts and corresponding ratios (denoted by the circles).

a discontinuous ($\lesssim$ 8 ms) spectral change at the peak intensity can not be ruled out.

After the peak intensity, the ratios show complex spectral changes. Some ratios ((c), (g) and (h) in Fig. 6.7, Fig. 6.8) continue to increase for 0.2-0.3 sec, reaching almost the same values as those of all the X-rays. Judging from the time scale, this spectral hardening is not due to the count fluctuations. It is interesting that the duration of the spectral hardening in 1987 is equal to or even shorter than that in 1990 in spite of the longer shot duration in 1987. We also notice that ratios between some energy bands temporally decrease at the relative time $0.3 - 0.6$ sec and become harder again. The minima of the temporal decreases are around 0.5 sec in 1987 and 0.4 sec in 1990. (In (c) and (h), one more decrease is found at the relative time about 0.25 and 0.6 sec, respectively. However, these are not recognized in the other ratios.) It can be found from the profile in each energy band shown in Fig. 6.5 that this temporal softening arises from relatively fast decrease in intensity in higher energy bands. In other words, the intensity in the lower energy band more gradually decrease. The profile in the decay phase changes on time scales a few hours or less, but we can not confirm their energy dependence because the small number of shots superposed results in poor statistics.

Table 6.6:
THE BEST-FITTING PARAMETERS WITH THE TWO EXPONENTAIL MODEL

RISE PHASE (1990)						
Peak Criteria[a]	$A_-[c/s]$	$\tau_{a_-}[s]$	$B_-[c/s]$	$\tau_{b_-}[s]$	$C_-[c/s]$	$\chi^{2\,b}_\nu$
$2.275 > R \geq 2.00$	3458 ± 82	0.100 ± 0.005	945 ± 56	0.72 ± 0.04	4512 ± 4	3.16
$2.60 > R \geq 2.275$	4948 ± 117	0.076 ± 0.003	1379 ± 56	0.70 ± 0.03	4549 ± 4	2.97
$R \geq 2.60$	6943 ± 152	0.079 ± 0.003	1946 ± 63	0.74 ± 0.02	4564 ± 4	2.27
DECAY PHASE (1990)						
Peak Criteria[a]	$A_+[c/s]$	$\tau_{a_+}[s]$	$B_+[c/s]$	$\tau_{b_+}[s]$	$C_+[c/s]$	$\chi^{2\,b}_\nu$
$2.275 > R \geq 2.00$	4251 ± 106	0.074 ± 0.003	901 ± 33	0.98 ± 0.04	4492 ± 4	2.27
$2.60 > R \geq 2.275$	5163 ± 110	0.081 ± 0.003	1006 ± 35	1.05 ± 0.05	4543 ± 4	1.94
$R \geq 2.60$	8604 ± 173	0.071 ± 0.002	1066 ± 28	1.34 ± 0.05	4542 ± 6	2.87

a Peak Criteria, R, stands for $p/<p>$.
b The degree of freedom is 250.

6.4 The Dependence on the Peak Intensity

The reason why we focus our attention on the dependence of the shot profiles on the peak intensities is that the dependence is thought to reflect physical nature when shots occur, and some physical models predict some dependence (§10.4).

Shots in 1987 were divided into two peak classes according to the peak intensities, $p/<p>$; $2.0 \leq p/<p> < 2.45$, and $2.45 \leq p/<p>$. While those in 1990 are divided into three; $2.0 \leq p/<p> < 2.275, 2.275 \leq p/<p> < 2.6$, and $2.6 \leq p/<p>$ (Negoro et al. 1994). Obtained profiles of the biggest and smallest superposed shots are shown in the left panels of Fig. 6.9 (1987) and 6.10 (1990). The right panels in both the figures show the excess shot component normalized by average counts in the two adjoining bins of the peak bins.

Time constants obtained by fitting these profiles with the sum of 2 exponentials were given in Table 6.6. As the decay profiles are mainly discussed here, the fractal function fits are not appropriate (cf., §6.2.1). These fits are, of course, not acceptable statistically, but enough to discuss properties of the whole profiles. Parameters in 1987 are not shown because a bump at the relative time around -4 sec is so different between the bigger and smaller superposed shots that the best-fitting parameters are much affected by them (cf., Table 6.7).

Note that the superposed shots in the same observation have almost the same time constants (durations) in spite of the large ($\sim$ 100 %) difference of the peak intensities. This shows the existence of some characteristic time constants independent of the peak intensity. The small bump at the relative time ~ -1.8 sec can be seen in all the superposed shots in 1990, but its

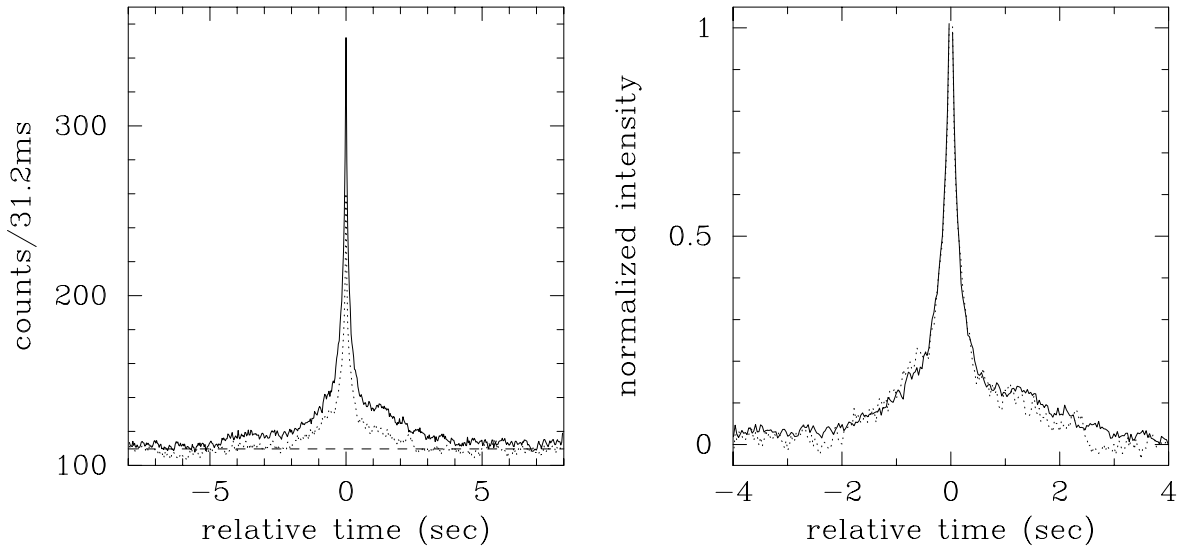

Figure 6.9: (*left panel*) Average profiles of the shots with different peak intensities in 1987. (*right panel*) Profiles of their excess shot components normalized by average counts in the adjoining bins of the peak bins. They are obtained by superposing 246 shots with $p \geq 2.0 <p>$ and $p < 2.45 <p>$ (dotted line) and 295 shots with $p \geq 2.45 <p>$ (solid line). Note that both the shots have almost the same time durations.

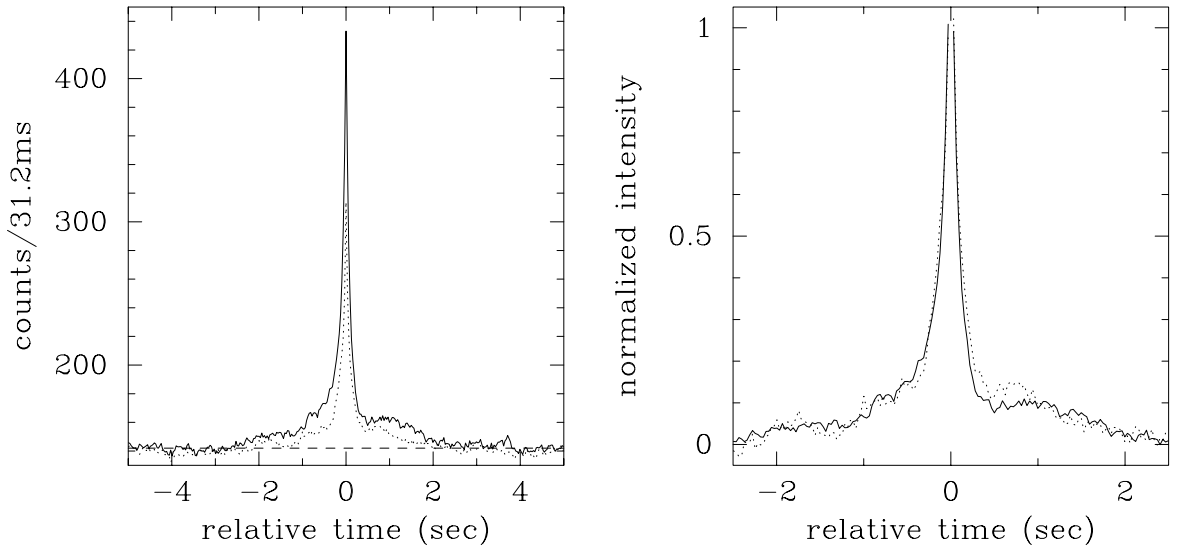

Figure 6.10: In the 1990 observation, average profiles and normalized profiles (see in Fig. 6.9). They are obtained by superposing 313 shots with $p \geq 2.0 <p>$ and $p < 2.275 <p>$ (dotted line) and 265 shots with $p \geq 2.6 <p>$ (solid line). The average profile of 294 shots with $p \geq 2.275 <p>$ and $p < 2.6 <p>$ is omitted for simplicity. It has just a middle profile between the superposed shots shown. Note that the larger shot has an asymmetric profile.

Table 6.7:
THE BEST-FITTING PARAMETERS
WITH THE FRACTAL FUNCTION PLUS GAUSSIAN MODEL

Data	Peak Criteria	Fractal						
		$A_-[c/s]$	$\tau_{a-}[s]$	α_-				
1987	$2.45 > R \geq 2.00$	1289 ± 266	0.008 ± 0.009	0.36 ± 0.07				
	$R \geq 2.45$	974 ± 27	0.057 ± 0.007	0.73 ± 0.03				
1990	$2.275 > R \geq 2.00$	470 ± 27	0.044 ± 0.008	0.80 ± 0.05				
	$2.60 > R \geq 2.275$	625 ± 34	0.021 ± 0.005	0.70 ± 0.04				
	$R \geq 2.60$	867 ± 40	0.023 ± 0.005	0.72 ± 0.03				
$C_-[c/s]$	Gaussian[a]			$\chi^{2\,b}_\nu$				
	t_c [s]	t_w [s]	Total Cnts [c]					
2611 ± 27	-4.54 ± 0.11	1.19 ± 0.25	476 ± 163	2.01				
3276 ± 26	-3.79 ± 0.04	0.57 ± 0.06	212 ± 26	1.17				
4255 ± 25	-1.84 ± 0.02	0.18 ± 0.02	81 ± 13	2.15				
4216 ± 30	-1.72 ± 0.02	0.15 ± 0.02	71 ± 13	1.44				
4152 ± 35	-1.90 ± 0.05	0.29 ± 0.05	92 ± 21	1.45				

a The gaussian function is represented by $N exp(-(t-t_c)^2/2t_w^2)$ with total counts $\sqrt{2\pi}Nt_w$.
b The degree of freedom in 1987 and 1990 are 185 and 121, respectively.

profile in the biggest shot is much (80 $\sim$ 90% in the Gaussian fits) broader than that in the smaller shots (see Table 6.7).

One can also notice that the biggest shot in 1990 have an asymmetric profile; the intensity gradually increases and rapidly decreases. This asymmetry is due to a difference of the decay profiles. Absolute intensities in the rise phase are much different between these shots, but their normalized shots have almost the same profiles (right panels of Fig. 6.9 and 6.10). On the other hand, absolute intensities in the decay phase, especially, after rapid decrease in intensity at $\sim$ 0.4 sec, are not so different each other, which is also recognized in the fitting parameter B_+, representing the tail emission component. B_+ of the biggest shot is only $\sim$20 % larger than that of the smallest one while the other intensity parameters, A_+, A_- and B_-, of the biggest shot are twice larger than those of the smallest one. After the rapid decrease, the intensity of the biggest shot remains constant for $\sim$ 0.8 sec in contrast to that of the smallest shot. Corresponding to this, τ_{b_+} of the biggest shot is about 37 % larger than that of the smallest shot.

We also note that Superposed shots accumulated at intervals of one day and divided by the peak intensity also show these tendencies.

As shown in Table 6.7, the total number of counts of the bumps in 1990 do not strongly depend on the peak intensities of the shots. The broad bumps in 1987, however, seem to depend

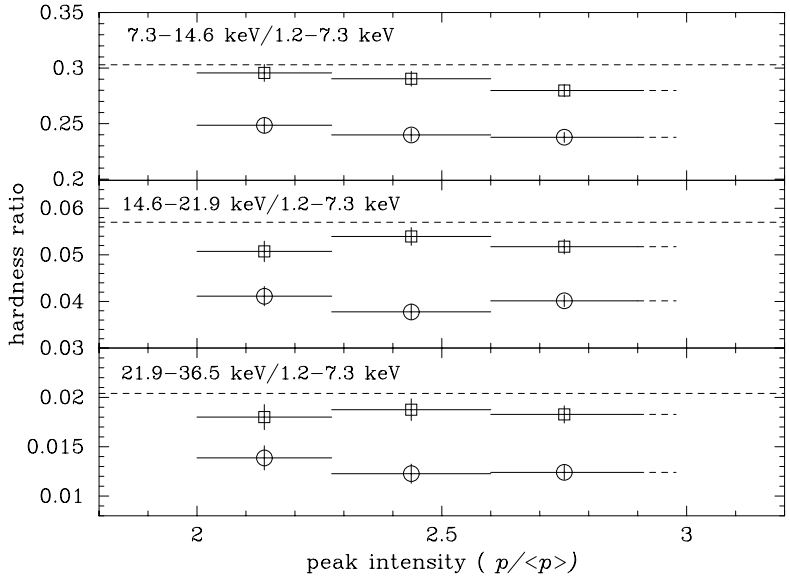

Figure 6.11: The dependence of hardness ratios of the excess shot components in the rise (circle) and decay (square) phase on the peak intensity (1990). The shots used are the superposed ones shown in Fig. 6.10. The dashed lines indicate average count ratios in all the X-rays.

on the magnitude of the shots.

Fig. 6.11 shows the dependence of hardness ratios of the superposed shot in the rise and decay phase on the peak intensity in the 1990 observation. The ratios are estimated from total counts of the excess shot component for 2 seconds before or after the peak. The ratios in the rise and decay phases are plotted by circles and squares, individually. The horizontal bars indicate the ranges of the peak intensities with which shots are superposed.

Note that all the ratios in the decay phase are larger than those in the rise phase, but lower than average count ratios in all the X-rays, indicated by the dashed lines in the figure. Also note that most of the ratios are independent of the peak intensities of the shots. Only the count ratios in (7.3-14.6 keV)/(1.2-7.3 keV), shown in the top panel, slightly indicate that the shots with smaller peak intensities have harder spectra than those with larger peak intensities. But, χ^2 fits with a constant value show at the 90 % confidence level that they are constant. These imply that, even if a number of smaller shots are summed up, its spectrum never approachs the average spectrum observed. Some other emission component with a harder spectrum than these shots is expected to exist.

Chapter 7

Comparison with Results of Other Timing Analyses

In studying the time variability of Cyg X-1, a power spectral density (PSD), an auto correlation function (ACF) and a variability coefficient function (VCF) have been utilized. They basically contain the same information on the variability. In this chapter, mainly using the data in 1990, the obtained properties of the superposed shots are compared with results of power spectrum analyses, and it is demonstrated that Fourier components below $\sim$ 1 Hz are well explained by the shot properties obtained. The cause of a high frequency component above 1 Hz will be discussed in §10.2.

7.1 Amplitude of a Power Spectrum

7.1.1 Profile

An ensemble-averaged PSD in 1.2-58.4 keV in 1990, normalized by the squared mean intensity (NPSD cf., Miyamoto et al. 1992), is shown by the points with 1 σ errors in the left panel (a) of Fig. 7.1. The white noise level due to the Poissonian statistics is subtracted, and the binning effect of the data (van der Klis 1989) is also corrected. At least 3 knees exist around 0.1, 1 and 10 Hz in the observed PSD. The approximate exponents of the PSD are 0.01$\pm$0.07 in $\nu \leq 0.1$ Hz, -0.90$\pm$0.01 in 0.1 Hz $< \nu \leq$ 1 Hz, -1.43$\pm$0.01 in 1 Hz $< \nu \leq$ 10 Hz, and -1.66$\pm$0.02 in 10 Hz $< \nu \leq$ 50 Hz. This PSD above $\sim$ 2 Hz is similar to that in 1987 (Makishima 1988; Kitamoto & Miyamoto 1989; Miyamoto et al. 1992).

A PSD of the superposed shot assumed to have a time symmetric profile is analytically

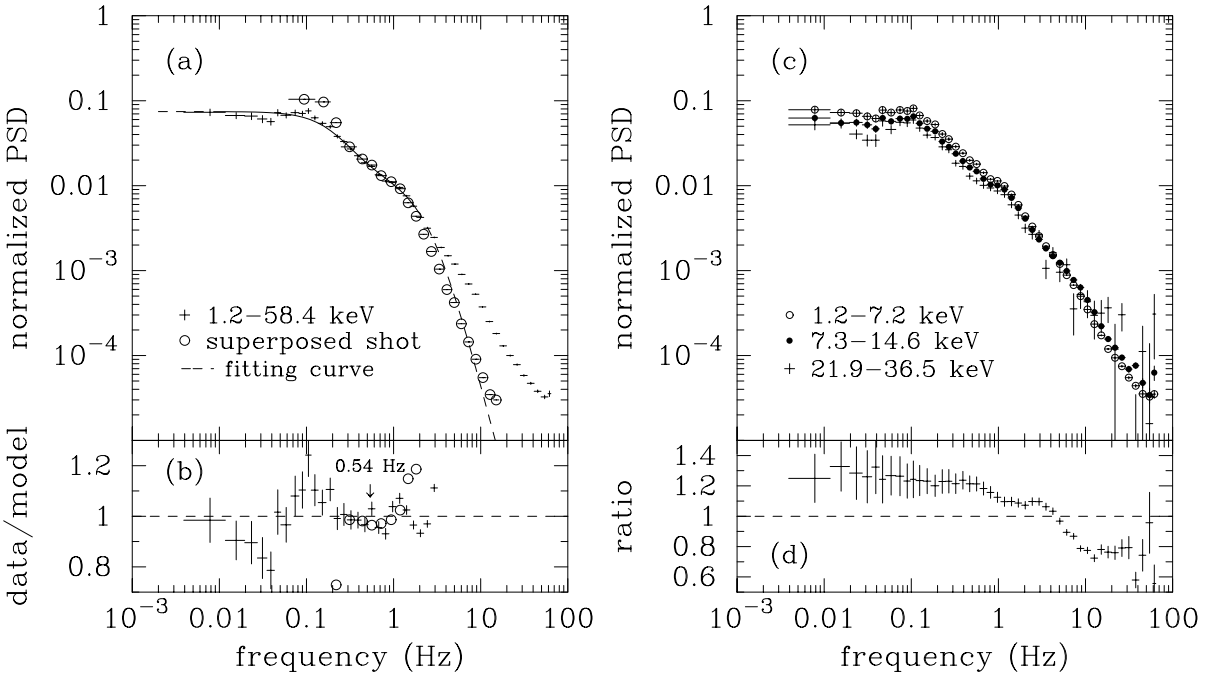

Figure 7.1: Observed NPSDs and PSDs of the superposed shot in the 1990 observation. (a) An ensemble-averaged observed NPSD (points with 1 σ errors) and a PSD directly computed by Fourier transforming the profile of the superposed shot (opened circles) are shown. The best-fitting model with a function deduced from the profile of the superposed shot is also indicated by the solid line. The best-fitting model out of the fitting ranges ($\nu \leq 0.01$ Hz, $\nu \geq 2$ Hz) is also shown by the dashed lines. (b) The ratios of the observed NPSD to the best-fitting model (points with 1 σ errors) and to the PSD directly obtained from the superposed shot profile (opened circles) (c) The observed NPSDs in different energy bands. (d) The ratio of the NPSD in the 1.2-7.3 keV band to that in the 7.3-14.6 keV band.

calculated from the sum of two exponentials, Eq. (5.1). The calculated model PSD is

$$PSD(\nu) = 4 \times \left(\frac{A\tau_a + B\tau_b + (A\tau_b + B\tau_a)\frac{\nu^2}{\nu_{a,kn}\nu_{b,kn}}}{\left(1 + (\frac{\nu}{\nu_{a,kn}})^2\right)\left(1 + (\frac{\nu}{\nu_{b,kn}})^2\right)} \right)^2 ; \ \nu_{a,kn} \equiv \frac{1}{2\pi\tau_a}, \ \nu_{b,kn} \equiv \frac{1}{2\pi\tau_b}. \quad (7.1)$$

This function has two knees around $\nu_{a,kn}$ and $\nu_{b,kn}(< \nu_{a,kn})$, and shows flat-top spectra (ν^0) below $\nu_{b,kn}$, and rapidly falls as proportional to ν^{-4} above $\nu_{a,kn}$. This model PSD roughly represents the above structures of the observed PSD in the frequencies of 0.01 to 2 Hz (the solid and dashed line in the same figure), and gives the best-fitting parameters, $\tau_a = 0.062 \pm 0.002$, $\tau_b = 0.64 \pm 0.03$ and $A/B = 6.7 \pm 0.3$.

Ratios of the observed PSD to the best-fitting model PSD are plotted in the panel (b) of Fig. 7.1 by the points with 1 σ errors. The ratio shows significant large structures around 0.04, 0.1 and 1 Hz and a sharp one at 0.5-0.6 Hz.

Next, a PSD of the superposed shot is directly computed by means of Fourier transforming the profile of the superposed shot, and plotted by the opened circles in the left panel (a) of Fig. 7.1. The normalization of the PSD is arbitrary and the PSD is plotted so as to have the same values as the observed one at 1 Hz. Though it has the limited frequency range and no certain errors, this PSD has very similar structures to the model one as expected. Moreover, the ratio of the observed PSD to this PSD (opened circles in (b)) shows no clear structures at 0.5-0.6 Hz and around 1 Hz, indicating that the superposed shot maintains structures unable to be represented by the fitting model, Eq. 7.1, equally by the sum of two exponentials (Eq. 5.1) in the real time space.

The most plausible candidates of these structures are the sub-structures, the small bump at the relative time -1.85 sec and the structures before and after $\sim$ 1 sec from the peak, described in §6.2.1. If these time periods are corresponding to Fourier periods, the corresponding frequencies are 0.54 Hz (indicated by the arrow in (b)) and $\sim$ 1 Hz, both of which give good agreements with the frequencies of the structures in the observed PSD. In the same sense, the increase in intensity by the shots and the decrease in intensity before/after 3 $\sim$ 5 sec from the peak recognized in the superposed shots (6.2.1) could correspond to the maximum and minimum of cosine waves with Fourier periods 6 $\sim$ 10 sec ($\simeq$ 0.1 $\sim$ 0.17 Hz). Thus, the decrease in intensity may explain the large differences between the observed PSD and the PSDs of the superposed shots at around 0.1 Hz.

A PSD in 1987 below $\sim$ 2 Hz is also roughly represented by the model PSD (Eq. 7.1). Residual structures in the fits are large, broad data excess at frequencies 0.05-0.15 Hz and slight, broad data excess around 0.8 Hz. However, a structure corresponding to the broad bump of the superposed shot at the relative time -3.7 sec is not recognized around 0.3-0.4 Hz.

There is no explanation for the large differences between the observed PSDs and the model (or directly computed) PSDs above 1–2 Hz. If a Lorenzian, $\propto 1/(1+(\nu/\nu_{Lz,kn})^2)$, is provided with the fitting model, the model function roughly represents the observed PSD to the frequencies $\sim$ 10 Hz. In this case, we obtain $\tau_a = 0.084 \pm 0.002$, $\tau_b = 0.69 \pm 0.03$, $A/B = 5.6 \pm 0.2$ and $\nu_{Lz,kn} = 5.4 \pm 0.2$ Hz. Fitting the PSD in 1987 with the same model gives $\tau_a = 0.146 \pm 0.007$, $\tau_b = 1.14 \pm 0.07$, $A/B = 4.4 \pm 0.3$ and $\nu_{Lz,kn} = 3.1 \pm 0.1$ Hz. Note that most of these time constants are in well agreements with those of the superposed shots in 1987 and 1990, and that the tendency that the ratio A/B in 1990 is larger than that in 1987 is also consistent with the superposed shots. Further detailed comparison of the fitting results with the superposed shots depends on the fitting model (representation of the sub-structures around 1 Hz and the

high frequency component).

A pair of very similar two time constants of two exponentials and a similar intensity ratio of the exponentials are obtained by completely independent methods, the superposition of the shots and the PSD, though the representation of the high frequency component has room to debate (§10.2). Against many crimes for the shot noise models, this is the first evidence that *the X-ray time variability in Cyg X-1 is characterized by the X-ray shots just like the superposed one obtained here.*

Finally, I emphasize again that the representation of the shots with the two exponentials is not so important. A PSD of the fractal function (Eq. 6.1) is difficult to show analytically. However, a PSD of the function describing the rise (or decay) phase has similar properties to a PSD of an exponential. The PSD of the fractal function is proportional to $\nu^{-2(1-\alpha_-)} (\simeq \nu^{\sim 0})$ at $\nu \ll 1/\tau_{f\_}$, and ν^{-2} at $\nu \gg 1/\tau_{f\_}$.

7.1.2 Energy Dependence

The soft energy spectrum of the shots is also consistent with the NPSD. It can be found from the right panels (c,d) of Fig. 7.1 that the observed NPSD of the softer energy band is larger than that of the hard energy band in the frequencies below 5 Hz. Especially, in the frequencies below 0.4 Hz, the NPSD in the 1.2-7.3 keV band is 25±3 % larger than that in the 7.3-14.6 keV band. This means that soft X-ray variability is relatively larger than hard one in the low ($\nu \leq$ 5 Hz) frequency range. In other words, the shots of which PSD dominates the observed PSD below 1 Hz have a soft energy spectrum.

From this fact, we obtain the following relation that $NPSD_L/NPSD_H$ ($\nu < 0.4$ Hz) (= 1.25±0.03) $\simeq [(F_{shot,L}/F_{all,L})/(F_{shot,H}/F_{all,H})]^2 = (\textit{hardness-ratio}_{all}/\textit{hardness-ratio}_{shot})^2$, where $F_{shot/all,L/H}$ means the flux of (the excess shot)/(all the) component in the (1.2-7.3 keV/7.3-14.6 keV) band. Together with $\textit{hardness-ratio}_{all} = 0.304$, these relations imply $\textit{hardness-ratio}_{shot} = 0.27 \pm 0.01$, which is well consistent with the average hardness ratio of the excess shot component, 0.26 ± 0.01 (Fig. 6.11). Thus, it can be concluded that the soft energy spectrum of the shot is consistent with the values of the NPSD quantitatively.

These results were also confirmed by means of the ACF and VCF (or variation functions). The VCF is, however, newly defined by

$$VCF(t_b) \equiv \frac{\sqrt{\sigma^2 - \overline{\sigma^2_{t_b}}}}{\overline{x} - x_{BG}}, \tag{7.2}$$

where σ and σ_{t_b} in the numerator are a variance of the data binned into a bin width of t_b and a

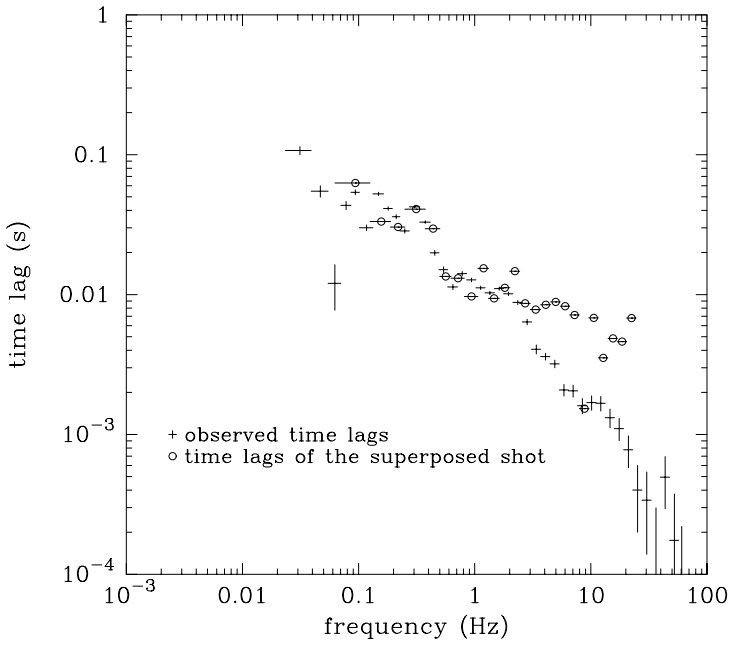

Figure 7.2: Time lags between the hard X-rays (7.3–14.6 keV) and the soft X-rays (1.2-7.3 keV) in the 1990 observation. Observed time lags and those of the superposed shot are denoted by points with 1 σ errors and opened circles, respectively. All these points indicate hard X-ray lags.

variance due to the statistical count fluctuations, respectively. Note that the latter variance is evaluated taking account of dead time of the detectors and other instrumental effects (Mitsuda & Dotani 1989) instead of $\sqrt{x}$ expected from the Poisson statistics (Oda et al. 1976; Ogawara et al. 1977; Kitamoto and Miyamoto 1989). The x and x_{BG} in the denominator indicate an observed X-ray counting rate in the bin-width t_b and a background counting rate, respectively. The soft energy spectrum of the shots was first pointed out by Ogawara et al. (1977) using a VCF. The above VCF shows that in any bin width ($\geq$ 7.8 ms) variability in a lower energy band is larger than that in a higher energy band. Even in the highest energy band (36.5-58.4 keV), VCF values do not significantly exceed those in a lower energy band.

7.2 Phase of a Power Spectrum

Time lags (a cross spectrum) between the curves in different energy bands are shown in Fig. 7.2. The hard X-ray variability lags behind the soft one by 30–50 ms in the frequencies of 0.03 to 0.5 Hz, and by $\sim$ 10 ms in the frequencies of 0.5 to 2 Hz. Time lags in further lower frequencies (at least to 5×10^3 Hz) were computed but no certain values were obtained. This stairs-like structure in the time lags is identical to a doubled peaked structure in the phase lags

found by Miyamoto et al. (1988, 1992). ($Time\text{-}Lag\ (\nu) = (T/2\pi) \times (Phase\ Lag\ (T))$, where T is a Fourier period, $= 1/\nu$.)

It is rather complicated to obtain an analytic formula of time lags of a superposed shot because the time symmetric approximation is impossible in this calculation. Approximate calculations show that time lags arise not only from different time constants in different energy bands, corresponding to the continuous spectral harding observed after the peak intensity (c.f., Miyamoto & Kitamoto (1989)), but also from the discrepancy between peak intensities in the rise and decay phases, corresponding to the rapid spectral hardening at the peak intensity.

Here, time lags of the superposed shot are directly computed from the profile, and plotted by opened circles in Fig. 7.2. The time lags of the superposed shot show similar values and similar stairs-like structure to the observed one in the frequencies below $\sim$3 Hz, where the time variability due to the shots is dominant, though they scatter largely and their certain errors are unknown,

Note that the superposed shots in different energy bands have almost the same time constants in the rise or decay phase as shown in Table 6.5, but their time lags show extremely large values. Consequently, the structure in the time lags is though to be due to the spectral changes of the shots just like those of the superposed shot.

In the frequencies above 3 Hz, the time lags of the superposed shot slightly decrease, and have a certain peak near 5 Hz. The lags of the superposed shot in the frequencies above 10 Hz are less reliable because lags computed from some superposed shots, obtained from different set of data or different time resolutions, show much different values in those frequencies.

Chapter 8

Shot Fraction

Now, we have evidence that shot and the other components exist. In this chapter, a shot fraction, defined by a rate of the shot component to all the components (Sutherland et al. 1978), is estimated using the results in the previous chapters. Next, from the obtained shot fraction, an effect of the suppression of the shot appearance (§6.1.1) on the profiles of the superposed shots is investigated.

8.1 Shot Fraction

In the previous chapters, we find the following relations between a *net* peak count P (c/bin) of a shot and a total count of the shot s (c) (§6.2.1), and between P and its distribution f (bin/s/c) (§6.1.2),

$$P = p - a <p>, \tag{8.1}$$

$$s(P) = bP, \tag{8.2}$$

$$f(P) = c\,exp(-P/p_{decay}), \tag{8.3}$$

where a is an unknown constant in the range of 0 to 1, p is an observed peak count, and b (bin) is a constant evaluated from the superposed shots. Using N in §6.1.2 (normalized by effective accumulated time) and Eq. (8.1), c (bin/s/c) in Eq. (8.3) can be written as a function of a,

$$c(a) = N\,exp(-a <p>/p_{decay}). \tag{8.4}$$

Let's assume that the above relations are valid for all the shots with any peak intensity. From Eq. (8.2) and (8.3), a counting rate due to the shots with P can be expressed as sf (c/s), which shows that the shots with p_{decay} make the greatest contribution to the total counts.

Therefore, total counting rates of the shots with $P \geq \alpha p_{decay}$, $S(\alpha)$ (c/s), is found to be

$$\begin{aligned} S(\alpha) &= \int_{\alpha p_{decay}}^{\infty} s(P) f(P)\, dP \\ &= (\alpha + 1)\, exp(-\alpha)\, b\, N\, p_{decay}^2\, exp(-a <p> / p_{decay}). \end{aligned} \tag{8.5}$$

As $<p> \simeq 3 <p>_{decay}$ in this observation, α and n in defining $p \geq n <p>$ in this analyses has the following relation,

$$\alpha \simeq 3(n - a). \tag{8.6}$$

Here, the shot fraction $f_{shot}(\alpha)$ is defined by

$$f_{shot}(\alpha) \equiv \frac{S(\alpha)}{<p> / t_{bin}}, \tag{8.7}$$

where t_{bin} is a bin width used, and $<p> / t_{bin}$ represents an average counting rate (c/s) of the source. The unknown parameter a in Eq. (8.7) will be determined from the NPSD. At low frequencies ($\nu < \nu_b$), a PSD of a shot shown in Eq. (7.1) is $s(P)^2$ ($\simeq (A_- \tau_{a_-} + B_- \tau_{b_-} + A_+ \tau_{a_+} + B_+ \tau_{b_+})^2$). Thus, using Eq. (8.3) and (8.4), a PSD of the shots with $P \geq \alpha p_{decay}$, PSD_{shot}, can be represented by

$$\begin{aligned} PSD_{shot}(\alpha) &= \int_{\alpha p_{decay}}^{\infty} s(P)^2 f(P)\, dP \\ &= (\alpha^2 + 2\alpha + 2)\, exp(-\alpha)\, b^2\, N\, p_{decay}^3\, exp(-a <p> / p_{decay}). \end{aligned} \tag{8.8}$$

In this calculation, we assume that the shots occur randomly. This means that cross terms[1] of PSDs of different shots average out to zero, and a PSD of the superposition of randomly occurring shots is the sum of a PSD of each shot. In practice, this is guaranteed at low frequencies ($\ll \nu_b$) (§6.1.1). Dividing Eq. (8.8) by the square of the average counting rate $<p> / t_{bin}$ yields a NPSD of this PSD. From the resultant NPSD and Eq. (8.5) and (8.7), we obtain

$$f_{shot} = \frac{\alpha + 1}{\alpha^2 + 2\alpha + 2} \frac{<p>}{b\, p_{decay}\, t_{bin}}\, NPSD(\nu \ll \nu_b). \tag{8.9}$$

Note that the shot fraction f_{shot} is determined independently of a.

A rate of the shot occurrence h (1/s) is given by integrating Eq. (8.3) by P from αp_{decay} to infinity,

$$h = N\, p_{decay}\, exp(-a <p> / p_{decay})\, exp(-\alpha). \tag{8.10}$$

[1] If a_k and b_k is the Fourier transforms of independent time variations (shots) $x(t)$ and $y(t)$, respectively, the power spectrum of $x(t) + y(t)$ is $a_k + b_k$ (the superposition theorem). In this case, its PSD is expressed by $|a_k|^2 + |b_k|^2 +$ cross terms.

Table 8.1:
CYG X-1 SHOT PARAMETERS

α	1987			1990		
	f_{shot}	a	h (1/s)	f_{shot}	a	h (1/s)
0.0	0.29	1.17	1.13	0.23	1.04	1.64
2.0	0.17	1.00	0.23	0.14	0.91	0.33
4.0	0.11	0.56	0.09	0.09	0.55	0.13
6.0	0.08	-0.02	0.05	0.06	0.08	0.07

†Used parameters in 1987 are $b = 19$ (bin), $N = 0.37$ (bin/s/c), $p_{decay} = 47$ and $<p> = 110$ c/bin. Those in 1990 are $b = 13$ (bin), $N = 0.64$ (bin/s/c), $p_{decay} = 52$ and $<p> = 150$ c/bin. The values within the parentheses are most likely ones in the ranges.

The NPSD in 1987 and 1990 are estimated from the observed average ones at frequencies below 0.05 Hz (§7.1.1), and found to be 0.145 and 0.065, respectively. Using observed values of the data binned into 31.25 ms ($= t_{bin}$), the resultant shot parameters are summarized in Table 8.1. f_{shot} has uncertainties of 10–30 %, and a and h have uncertainties of 30–40 %. Note that a is over 1 if α is small (Table 8.1). This means that some of the assumptions (Eq. 8.1, 8.2, 8.3) are wrong, or that smaller shots ($\alpha \lesssim 2$) do not exit. This problem may be avoided if b or p_{decay} is small. If b is a half of the used values, the shot fractions are 2 times larger (Eq. 8.9) and a becomes much small (Eq. 8.5). However, the assumptions are confirmed for shots with larger peak intensities ($\alpha \gtrsim 4$). Consequently, shots with small peak intensities are unlikely to have almost the same profiles as the superposed shots. Comparing a with observed light curves, $\alpha =$ 3–4 is most likely. This conclusion suggest that the shots are somewhat special big events for the radiation process in this source. It should be also noted that the shot fractions with small uncertainty (Eq. 8.9) are relatively small (10–20%) in all the range permitted ($a < 1$), compared with ones in the shot noise models ($\sim 50\%$).

8.2 Effect of the Non-Random Temporal Distribution

There are two possibilities to bring about the observed non-random peak-interval distributions (§6.1.1). One is that the shot appearance in the low-frequency period is suppressed. The other is that intensity of another component decreases in the period, resulting in the decrease of peak counts of shots in the period. It is difficult to distinguish the real origin from these two possibilities. Here, we only consider the first possibility easy to estimate, and examine the effect on a profile of a superposed shot as follows.

To know how much intensity decreases, we must also know how much the shot appearance is suppressed. However, the shots have an extended structure so that a true occurrence rate near the shots is unable to be evaluated correctly. Here, we assume from Fig. 6.1 that the appearance of the shots with $p \geq n<p>$ is suppressed by 20 % through its low-frequency period independently of the peak intensity. If so, as the shot fraction is only 20–40 %, a rate of the intensity decrease in low-frequency period can be estimated to be only $4 \sim 8$ %.

Furthermore, putting a typical lower limit of the peak intensity of the shots suggested in the previous subsection at α_{low}, a rate of the shots with $p > n<p>$ ($\alpha \simeq 3(n-a)$) to all the shots with $P \geq \alpha_{low}$ is, from Eq. (8.5),

$$\frac{S(\alpha)}{S(\alpha_{low})} \simeq \frac{\alpha+1}{\alpha_{low}+1} exp\{-(\alpha-\alpha_{low})\}. \tag{8.11}$$

If $\alpha = 4.5$ ($n \simeq 2$, $a = 0.5$) and $\alpha_{low} = 3$ ($n \simeq 1.5$), then $S(\alpha)/S(\alpha_{low}) \simeq 0.3$. Thus, at the low-frequency period of the bigger shots, the intensity decreases by only $1 \sim 2$ %, and the other possibilities show smaller decreasing rate than this. This rate is consistent with that of the intensity decrease before the shots found in §6.2.1.

Chapter 9

Energy Spectrum

The analyses in the previous chapters show that the energy spectrum of Cyg X-1 consists of at least 3 components: a soft component of the shots in the rise phase, a slightly soft component of the shots in the decay phase, and a hard (steady) component. In this chapter, detailed spectral evolution during the shots is investigated using MPC 2 high-bit-rate mode data in 1987. After that, observed time averaged energy spectra in 1987 and 1990 are fitted not only with current single power law models but also with multi-component models which results of the spectral analysis of the shots require.

9.1 Energy Spectra of the Shots

9.1.1 Time Averaged Spectra

Fig. 9.1 illustrates the superposed shot obtained from data taken in MPC 2 high-bit-rate mode in 1987. First of all, a spectrum of a subtracted component, which is the component below the baseline counts (indicated by dashed line in the figure), and the time averaged spectrum in the same period are fitted with a power law with interstellar photoelectric absorption model[1] (Fig. 9.2). Their results are summarized in Table 9.1. For a comparison, a result of a fit to the time averaged spectrum in 1990 with the same model is also shown. The power law spectral model with a photon index α and normalization factor A [c/s/keV/LAC at 1 keV] is represented by

$$\frac{dN}{dE} = AE^{-\alpha}, \tag{9.1}$$

[1]In all spectral fits in this thesis, 1 % systematic errors, mainly coming from random errors of the ADC, are included for each energy channel.

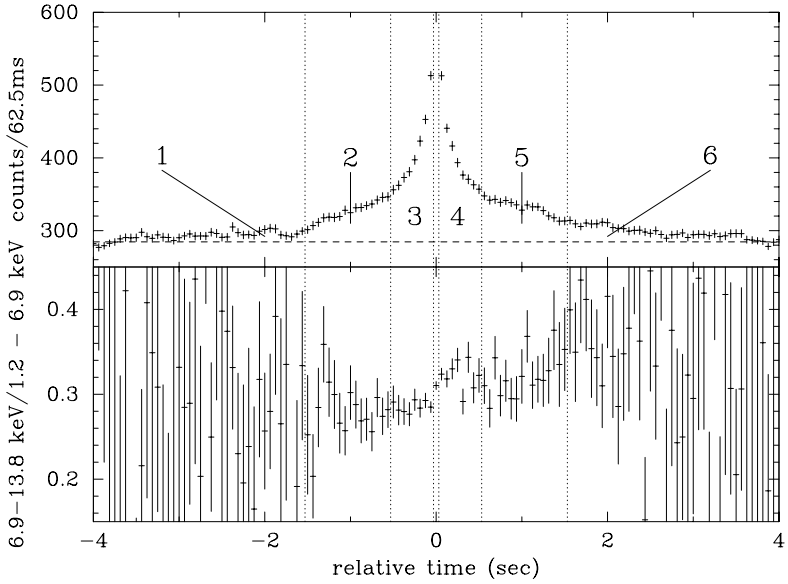

Figure 9.1: (*upper*) A superposed shot obtained from 345 shots with $p \geq 1.9 < p >$. (*lower*) Hardness ratios of the excess shot component of the superposed shot. They are picked up from the curves in MPC 2 high bit-rate mode data in 1987 Aug 5, under the peak criterion $T_p = 0.125$s. A baseline count defining the excess shot component is indicated by the dashed line in the upper panel. 6 energy spectra are made of the excess shot component divided by the dotted lines.

and the interstellar absorption model with equivalent hydrogen column density N_H [hydrogen atoms/cm^2], M_{abs}, is

$$M_{abs} = e^{-N_H \sigma(E)}, \tag{9.2}$$

where $\sigma(E)$ is the absorption cross section for interstellar matter calculated by Morison Mc-Cammom (1983).

The fitting results show that the photon index of the subtracted component is consistent

Table 9.1:
BEST-FITTING PARAMETERS TO THE TIME AVERAGED SPECTRUM AND THE SUBTRACTED COMPONENT WITH THE POWER LAW MODEL[a]

Data	A	α	$\log N_H$	χ^2_ν (d.o.f.)
average in 1987[b]	6176	1.557	< 20	11.0 (43)
subtracted component	6925 ± 165	1.562 ± 0.011	20.46 ± 0.64	4.27 (43)
average in 1990[b]	6403	1.568	< 20	8.67 (43)

a All uncertainties are quoted at the 90 % confidence level.
b Obtained errors in this fit are negligible small.

with that of the time averaged spectrum in 1987. A "PHA-ratio", pulse height analysis ratio of these spectra, also shows no significant structures at all the energies.

The remarkable points in this fits are as follows.

1. A line structure around 6.4 keV.

2. A broad edge-like structure at energies $7 \sim 20$ keV.

3. A high X-ray excess (hard X-ray bump) at the higher energies.

4. Much smaller column density of the interstellar absorption than that of the galactic interstellar absorption, $\log N_H = 21.85$, suggesting a soft X-ray excess.

For 3rd, fitting the spectra above 10 keV in 1987 and 1990 with a power law model yields smaller photon indices 1.421 ± 0.012 and 1.425 ± 0.015, respectively. These line and broad absorption features have been pointed out by many authors (Inoue 1989; Ebisawa 1991), and are very similar to spectra of AGNs (Pounds et al. 1990; Matsuoka et al. 1990). The lower absorption has been discussed relating with a soft excess component (Priedhorsky et al. 1979; Balucińska & Chlebowski 1988; Barr & van der Woerd 1990; Balucińska & Hasinger 1991).

The photon indices of the time averaged spectra are different from previously reported values 1.50 in 1987 and 1.52 in 1990 by Ebisawa (1991) who analyzed the same *Ginga* data. This seems to be because he used a different background in 1987, and made spectra of several set of data, some of which are not used in this thesis. (In the data on Aug 8 he used, soft X-ray absorption was recognized, and excluded in this study.)

9.1.2 Spectra of the Excess Shot Component

According to the spectral changes during the shot, the excess shot component in the decay phase are divided into 3 parts as shown in Fig. 9.1, and 3 energy spectra are made of them. The excess shot component in the rise phase are also divided into 3 parts just like in the decay phase though the hardness ratios in the rise phase hardly change. The resultant 6 spectra are numbered from 1 to 6 in order of time as shown Fig. 9.1. It should be noted that the spectra of the excess shot component are free from background X-ray counts. Fitting the spectra with the power law with interstellar absorption model gives far small column densities of the interstellar absorption ($\log N_H < 20$). Thus, the spectra are fitted with the only power law model. This small column densities mean that, in even the soft spectrum of the shots, a soft excess component is present. Spectra in the rise and decay phase (data No. 1+2+3 and 4+5+6 in Fig. 9.1) are also

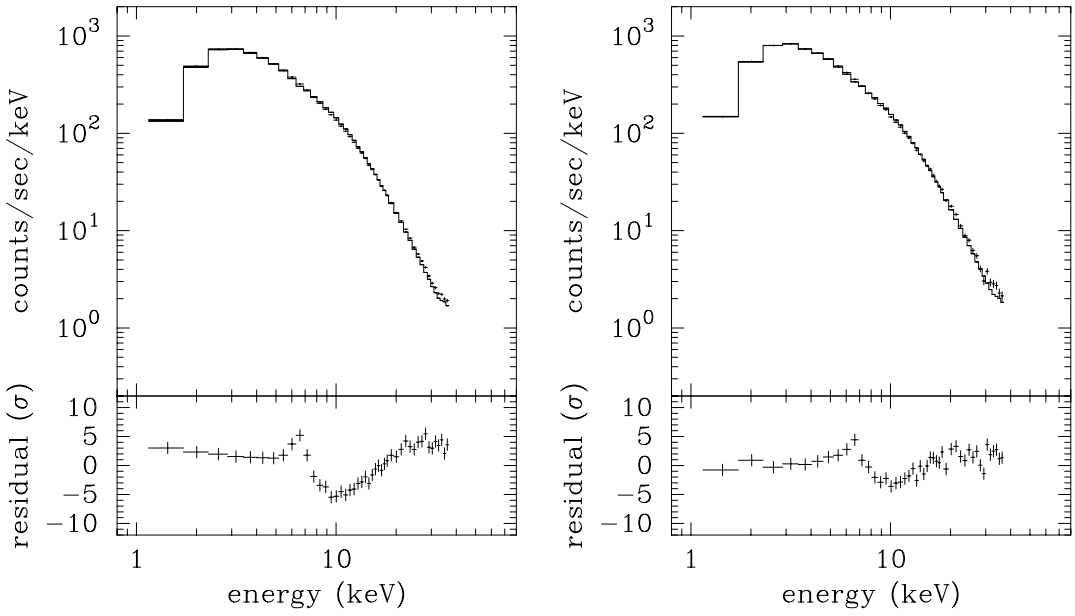

Figure 9.2: (*left*) The time averaged spectrum of Cyg X-1 taken in Aug 6. (*right*) The spectrum of the subtracted component (see text). The model spectrum shown is a power law with interstellar absorption model.

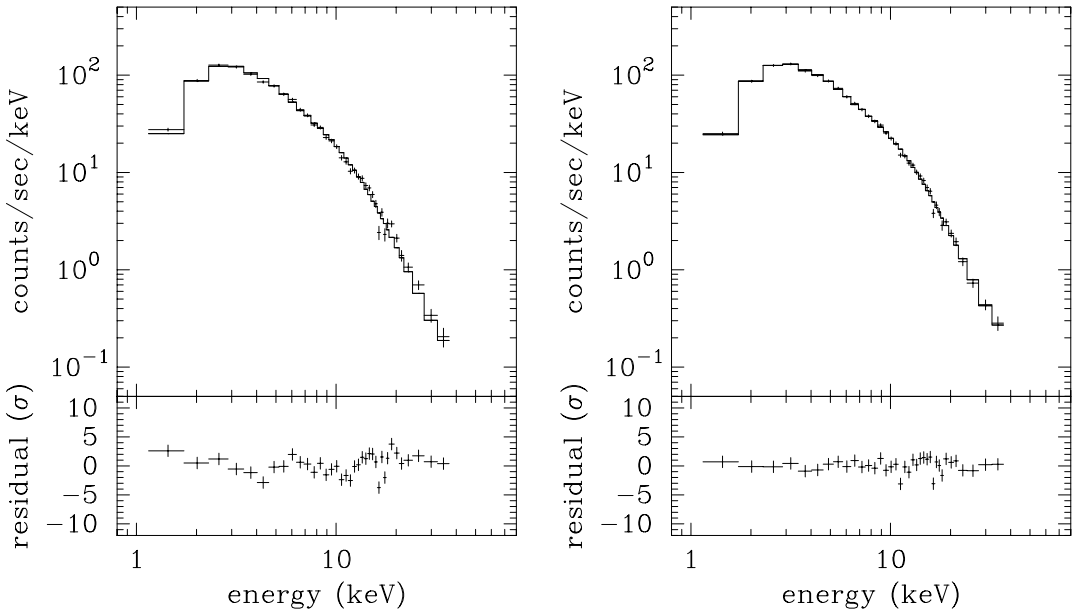

Figure 9.3: (*left*) The energy spectrum of the excess shot component in the rise phase. (*right*) That in the decay phase. The best-fitting power law model is also shown.

Table 9.2:
BEST-FITTING PARAMETERS TO THE SPECTRA OF
THE EXCESS SHOT COMPONENT WITH THE POWER LAW MODEL[a]

Relative Time[b] [sec]	Data No.[c]	A [c/s/keV]	α	$(\alpha^{d}_{E>10keV})$	χ^2_ν (d.o.f.)
(-8, -0.031]	1+2+3	1259 ± 42	1.749 ± 0.019	(1.50 ± 0.09)	2.88 (35)
(-8, -1.531]	1	353 ± 56	1.796 ± 0.092	(1.54 ± 0.12)	0.91 (18)
(-1.531, -0.531]	2	1276 ± 69	1.734 ± 0.030	(1.43 ± 0.15)	1.49 (26)
(-0.531, -0.031]	3	3952 ± 117	1.750 ± 0.016	(1.48 ± 0.08)	1.94 (32)
[0.031, 8)	4+5+6	1147 ± 35	1.624 ± 0.016	(1.58 ± 0.07)	1.20 (35)
[0.031, 0.531)	4	3140 ± 96	1.624 ± 0.016	(1.48 ± 0.07)	1.27 (32)
[0.531, 1.531)	5	1203 ± 58	1.614 ± 0.026	(1.53 ± 0.12)	0.82 (26)
[1.531, 8)	6	441 ± 44	1.636 ± 0.056	(1.85 ± 0.36)	1.20 (18)

a All uncertainties are quoted at the 90 % confidence level.
b For instance, $(t_a, t_b]$ means $t_a < t \leq t_b$ where t is the relative time in Fig. 9.1.
c see Fig. 9.1.
d Photo indices in fitting the spectra above 10 keV. Normalizations and reduced χ^2 values in those fits are not shown.

fitted separately with the same power law model (Fig. 9.3). All these results are summarized in Table 9.2. Obviously, the photon index varies from ~ 1.75 before the peak intensity to ~ 1.62 after it. Note that all the photon indices are larger than that of the time averaged spectrum (or the spectrum of the subtracted component). Adding a gaussian function at energy around 6.4 keV did not provide a significant improvement in χ^2 if FWHM of the gaussians were free.

Fig. 9.4 plots time evolution of the ("PHA") ratio of these spectra to a power law spectrum with the same photon index as the time averaged one, 1.56. (Normalizations are free.) The χ^2 values in the fits and this PHA ratios show that the spectra in the rise phase are worse described by this model than those in the decay phase, and exhibit a valley-like structure around 12 keV, which does not look like any absorption structure. This strange structure at energies $10 \sim 20$ keV in the rise phase is also recognized in energy spectra produced from the MPC 3 data with 12 energy bands in 1990.

We can also find from Fig. 9.4 and the photon indices at energies above 10 keV, $\alpha_{E>10keV}$, in Table 9.2 that the energy spectra above 10 keV do not tend to change though they have large uncertainties. This conflicts with the results of the hardness ratios obtained from the MPC 3 mode data (cf., (e, j) in Fig. 6.7). As the these spectra are free from the background X-ray counts and the MPC 3 mode data were obtained another day, this conflict may arise from the source activity. Thus, the following two possibilities arise.

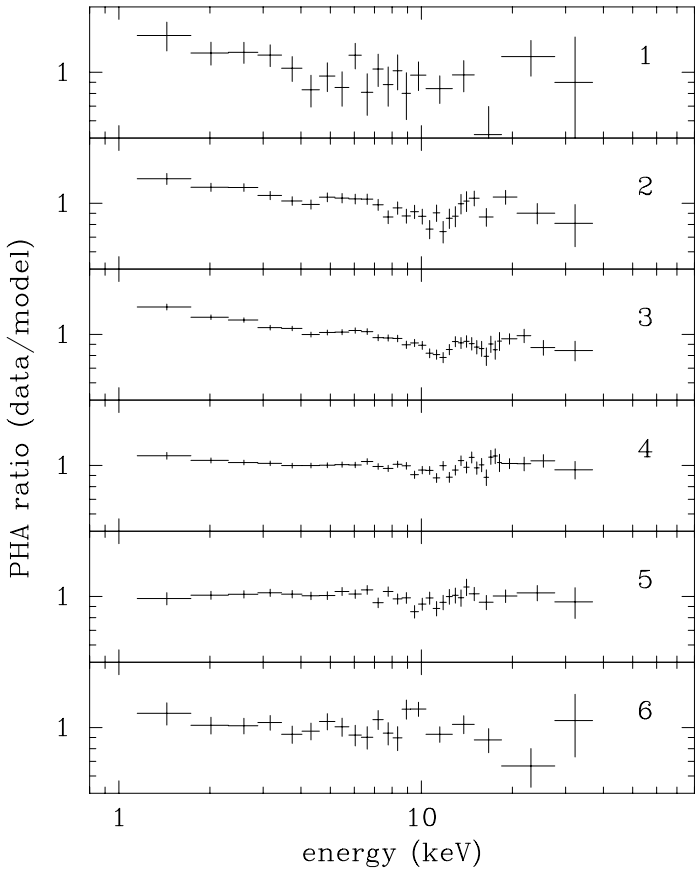

Figure 9.4: Time evolution of ratios of the spectra of the excess shot components to a power law spectrum with the photon index 1.56 and a free normalization. The integers in the panels represent time sequence numbers shown in Fig. 9.1.

(a) The shots have a soft energy spectrum at energies below $\sim$ 10 keV.

(b) The shots have a soft energy spectrum at all the energies (1.2–37(58) keV).

These spectra of the excess shot components were presumably produced by more simple physical process than the time averaged one. Thus, their physical parameters should be investigated. However, each spectrum does not have so good statistics that the only spectra within 0.5 sec from the peak intensity (data No. 3 and 4) are used in this study. The amount of the interstellar absorption has been well studied since the discovery of Cyg X-1 because it allows us to know the distance to the Cyg X-1 binary (see Oda 1977). Thus, hereafter the column density of the interstellar absorption will be fixed at log $N_H = 21.8$ predicted from optical reddening estimates (Margon et al. 1973; Bregman et al. 1973) though none of these spectra require such a large value.

Comptonized Blackbody Model

Both the spectra in the rise and decay phase are not represented by a single power law with the fixed interstellar absorption model at all because of a large soft excess (χ^2/d.o.f. = 221/44 for the rise phase, 160/44 for the decay phase). Instead of the power law model, a Comptonized blackbody model by Nishimura, Mitsuda, & Ito (1986) fits to the spectra, and provides significant reductions in χ^2 (Table 9.3). In this model, the soft excess component is represented by a (modified) blackbody component. In similar unsaturated Compton scattering models (Shapiro et al. 1976; cf., Sunyaev & Titarchuk 1980), the photon index depends on the Compton y parameter defined as $y = (4mc^2/kT_e)\mathrm{Max}(\tau, \tau^2)$. Thus, in this case, as keT_e exceeds the energy range of this fits and can not be determined uniquely, the resultant best-fitting electron temperature keT_e and optical depth τ are correlated. Thus, to know dependence of these two spectra on each parameter, some of these parameters are fixed at some values as χ^2 values in both the rise and decay phase should be small (Table 9.3). In this case, we can find that the electron temperature or optical depth of the hot plasma increases by 13 ± 4 keV or $0.16 \sim 0.09$ during the shots (~ 0.5 sec).

It should be also noted that the temperatures of the blackbody keT_{bb} are far below the energy range, which suggests that the blackbody components can be replaced by another thermal spectrum with a similar low temperature or a steep power law.

These spectra in the rise and decay phase are better described by a Comptonized blackbody plus power law model (Fig. 9.5). The addition of the power component results in a significant improvement in χ^2 for the spectrum in the decay phase, and a marginal one for the spectrum in the rise phase. The spectra in higher energies are represented by the hard power law, which results in decreasing keT_e and τ of the Comptonized blackbody. At $E \gtrsim keT_e$, an approximation in calculating the Comptonized blackbody model is not valid, and the model gives larger values than the considering situation (Nishimura et al. 1986). Thus, true photon indices in this model may be slightly smaller (harder) than the best-fitting parameters.

Note, however, that keT_e and τ of the Comptonized blackbody and α of the power law in the rise are consistent with those in the decay phase in spite of their different contribution to each of the spectra. This implies that the spectra of the shots can be solely represented by these two components. Hereafter, this model will be referred as a "Comptonization model". This model well describes the possibility (a) that the spectrum in the rise phase is soft at energies below $\sim$ 10 keV (Fig. 9.5). The Comptonized blackbody component exceeds the power law one at energies below $\sim$ 7 keV in the rise phase. While, in the spectrum in the decay phase, the power

Table 9.3:
BEST-FITTING PARAMETERS TO THE SPECTRA OF
THE EXCESS SHOT COMPONENT WITH THE COMPTONIZED BLACKBODY MODEL[a,b]

Data	Comptonized Blackbody				Power Law		χ^2_ν (d.o.f.)
	$Flux^c$	kT_{bb} [keV]	kT_e [keV]	τ	A	α	
Rise Phase	10.4 ± 4.7	0.219 ± 0.011	60 ± 4	0.65 ± 0.07	—	—	1.80 (30)
	10.0 ± 3.9	0.222 ± 0.010	60 (fixed)	0.66 ± 0.03	—	—	1.75 (31)
	9.9 ± 3.0	0.223 ± 0.008	59 ± 2	0.68 (fixed)	—	—	1.75 (31)
	8.1 ± 0.7	0.219 ± 0.002	46 ± 2	0.56 ± 0.03	1193 ± 75	1.488 ± 0.025	1.62 (28)
Decay Phase	8.4 ± 3.9	0.223 ± 0.012	68 ± 7	0.75 ± 0.09	—	—	1.38 (30)
	8.1 ± 3.8	0.235 ± 0.013	60 (fixed)	0.82 ± 0.09	—	—	1.38 (31)
	8.8 ± 2.7	0.213 ± 0.008	72 ± 3	0.68 (fixed)	—	—	1.33 (31)
	8.4 ± 12.5	0.176 ± 0.024	37 ± 12	0.42 ± 0.16	1793 ± 672	1.454 ± 0.091	1.15 (28)

a, b, c see Table 9.4.

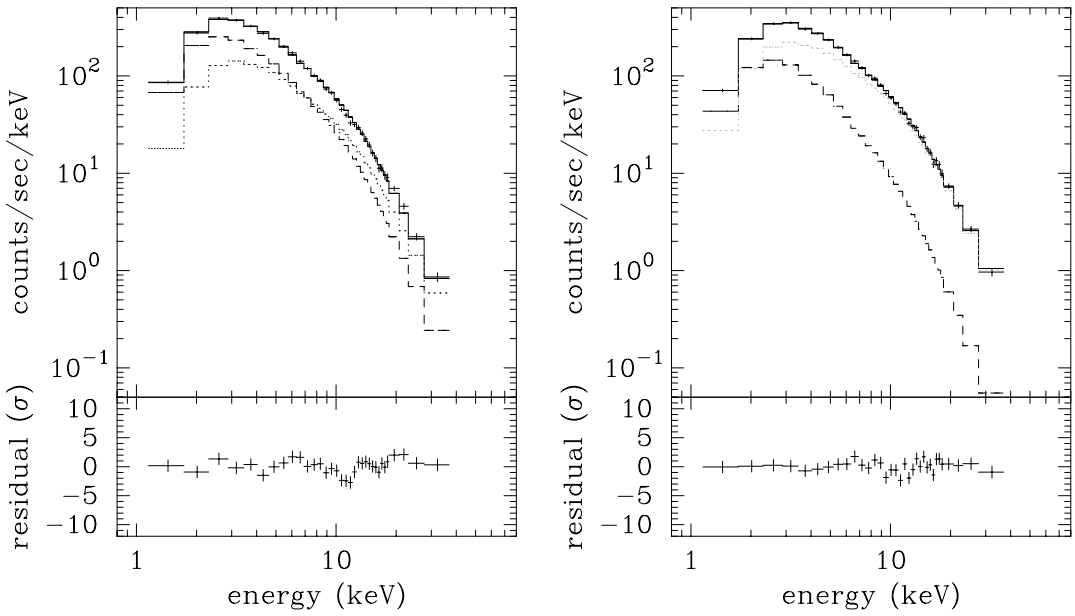

Figure 9.5: (*left*) The Spectrum in the rise phase, data No. 3. (*right*) That in the decay phase, No. 4. The best-fitting Comptonized blackbody plus power law model and model components, the Comptonized blackbody component and power law component, are shown by the solid lines, the dashed lines and dotted lines, respectively.

law component dominates over the Comptonized blackbody component at all the energies except below a few keV. In conclusion, this model implies that the soft energy spectrum of the shots arise from the Compton scattering of photons from a low temperature blackbody by optically thin hot plasma.

Power Law Model

A Comptonized blackbody model is approximately decomposed into a modified blackbody component and an unsaturated Compton scattering component by optically thin hot plasma. In $\tau < 1$ and $E \lesssim keT_e$, they can be approximately replaced by a blackbody model and a power law model, respectively. Thus, both the spectra in the rise and decay phase (No. 3 & 4) are fitted with this blackbody plus power law model (Table 9.4), and slight improvements in χ^2 are found. The temperature of the blackbody is a little higher than that of the Comptonized blackbody. This is because the blackbody component of the Comptonized blackbody model is a modified blackbody up-scattered by hot plasma, resulting in a higher color temperature than the effective temperature.

Adding one more power law function to the model, similar to the addition of a power law component to the modified blackbody model in the previous section, does not result in significant improvements in χ^2 in both the rise and decay phases (Table 9.4). Thus, this model is somewhat artificial. However, the best-fitting parameters of the two photon indices, α_1 and α_2, in the rise phase are consistent with those in the decay phase. As seen in Fig. Fig. 9.6, this model supports the possibility (b) that the spectrum in the rise phase is soft at all energies. The soft power law component (dotted line) dominates over the hard power law component (dashed-dotted line) at all the energies before the peak intensity. In the decay phase, the hard power law component comes to play an important role, especially at hard energies.

Note that this model is not suitable to these spectra compared with the Comptonized blackbody plus power law model. This conclusion, however, may be inapplicable to spectra obtained another day because the PHA ratios of the spectra taken in MPC 2 mode conflicts with the hardness ratios taken in MPC 3 mode as mentioned before. Thus, this two power law model is still a possible model, and will be referred as a "multi-power law model".

Table 9.4:
BEST-FITTING PARAMETERS TO THE SPECTRA OF
THE EXCESS SHOT COMPONENT WITH THE POWER LAW MODEL[a,b]

Data	Blackbody		Power Law		Power Law		χ^2_ν (d.o.f.)
	$Flux^c$	kT_{bb} [keV]	A_1	α_1	A_2	α_2	
Rise Phase	2.5 ± 2.9	0.270 ± 0.030	3975 ± 211	1.747 ± 0.026	—	—	1.74 (30)
	2.4 ± 0.7	0.276 ± 0.008	3837 ± 104	1.764 ± 0.016	133 ± 65	1.41 ± 0.20	1.84 (28)
Decay Phase	2.4 ± 1.0	0.253 ± 0.009	3292 ± 70	1.640 ± 0.011	—	—	1.36 (30)
	1.9 ± 0.8	0.269 ± 0.010	2388 ± 100	1.753 ± 0.026	992 ± 69	1.48 ± 0.03	1.35 (28)

a All uncertainties are quoted at the 90 % confidence level.
b The column density of the interstellar absorption is fixed at 6×10^{21}.
c Bolometric flux [10^{-9} erg/s/cm^2] is shown.

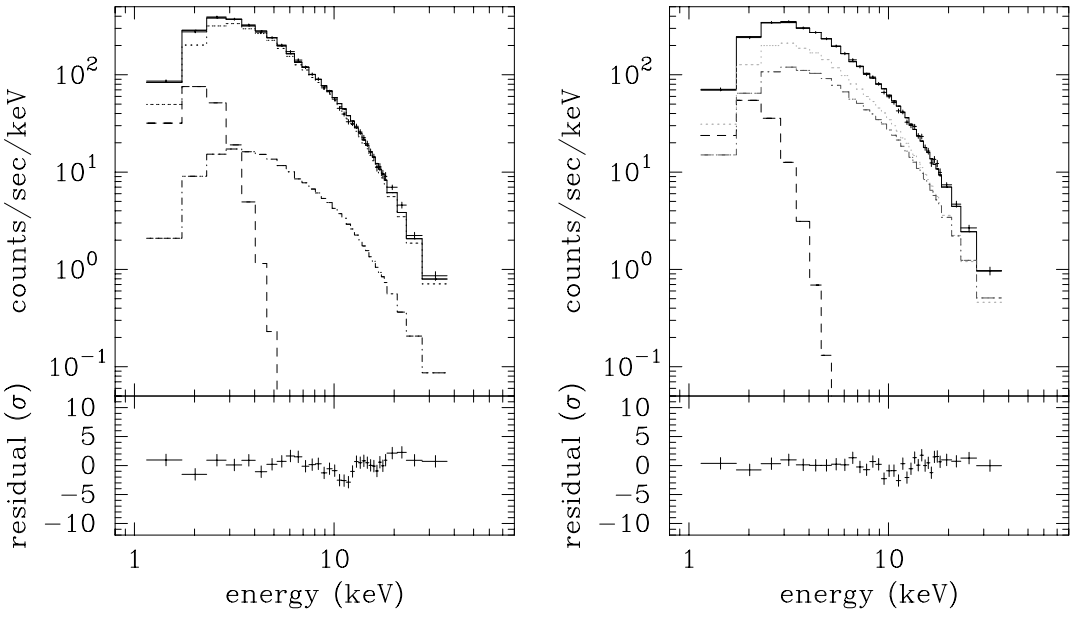

Figure 9.6: Fits to the same spectra in Fig. 9.5 with a blackbody plus two power law model, of which components are indicated by dashed lines, dotted lines (soft power) and dashed-dotted lines (hard power), respectively.

9.2 Time Averaged Spectra

9.2.1 Previous Models

A number of spectral models and their interpretations have been proposed for remarkable structures in the energy spectrum of Cyg X-1 in the low state. For instance, the broad absorption at energies 8–20 keV is reproduced by K-edge absorption of irons or smeared edge absorption (Ebisawa 1991), and a hard X-ray excess at higher energies is explained by partial absorption (partial covering of the source by cold absorber) (Done et al. 1992; Marshall et al. 1993) or reflected X-rays by cold matter (Done et al. 1992; Marshall et al. 1993).

Certainly, the time averaged spectra in 1987 and 1990 are substantially described by these models (Fig. 9.7, 9.8), and some of which yield acceptable fits. The K-edge absorption of He-like irons model with iron line centroid energy fixed at 6.4 keV gives a photon index $\alpha = 1.54$, $\log N_H < 20$ (χ^2/d.o.f. = 147/42) for the spectrum in 1987, and $\alpha = 1.55$, $\log N_H < 20$ (χ^2/d.o.f. = 149/36) for that in 1990. The smeared edge model yields slightly gently slopes $\alpha = 1.53$, $\log N_H < 20$ (χ^2/d.o.f. = 51/41, 1987), and $\alpha = 1.54$, $\log N_H < 20$ (χ^2/d.o.f. = 74/35, 1990), respectively. The partial absorption (covering) model including an gaussian function shows $\alpha = 1.58$, $E_{Fe} = 6.47 \pm 0.15$ keV, $\log N_H < 20$ (χ^2/d.o.f. = 144/40) for the 1987 spectrum, and $\alpha = 1.60$, $E_{Fe} = 6.3 \pm 0.3$ keV $\log N_H < 20$ (χ^2/d.o.f. = 143/34) for the 1990 one. The reflection model with the ionization parameter $\xi = 0.0$ or 0.02, coded by Kitamoto, gives the least χ^2 values at $\xi = 0.0$, and at that case $\alpha = 1.71$, $\log N_H = 21.2 \pm 0.1$ (χ^2/d.o.f. = 45/42, 1987) and $\alpha = 1.72$, $\log N_H = 21.2 \pm 0.2$ (χ^2/d.o.f. = 62/36, 1990). Note that all of the column densities in these fits are free, and the resultant column densities except those of the reflection model are much smaller than $\log N_H = 21.8$ expected from the galactic absorption. If the column density is fixed at $\log N_H = 21.8$, these models completely break down.

9.2.2 Multi-Continuum Model

The timing analyses in the previous chapters have demonstrate that the energy spectrum of Cyg X-1 do not consist of one continuum component. Thus, *we must not interpret the observed spectrum of Cyg X-1 by means of these models based on a single power law continuum.* Now, we know the parameters of the two models describing the spectrum of the shots in the previous subsection. Let's describe the time averaged spectra by models including the soft spectral component of the shots.

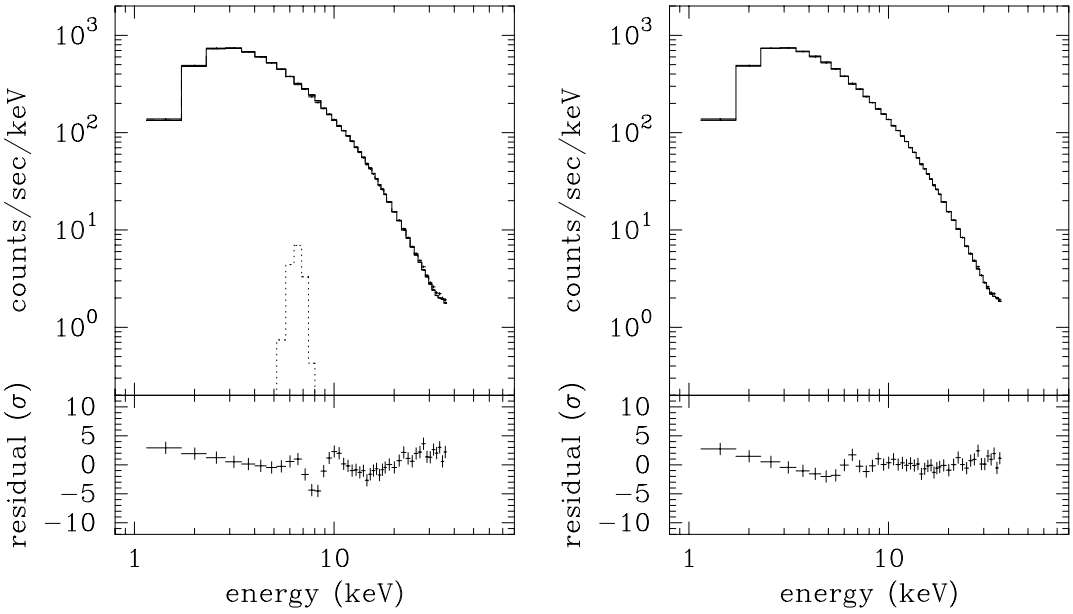

Figure 9.7: Fits of the time averaged spectrum in 1987 with previous fitting models. (*left*) The K-edge absorption model. (*right*) The smeared edge model by Ebisawa (1992).

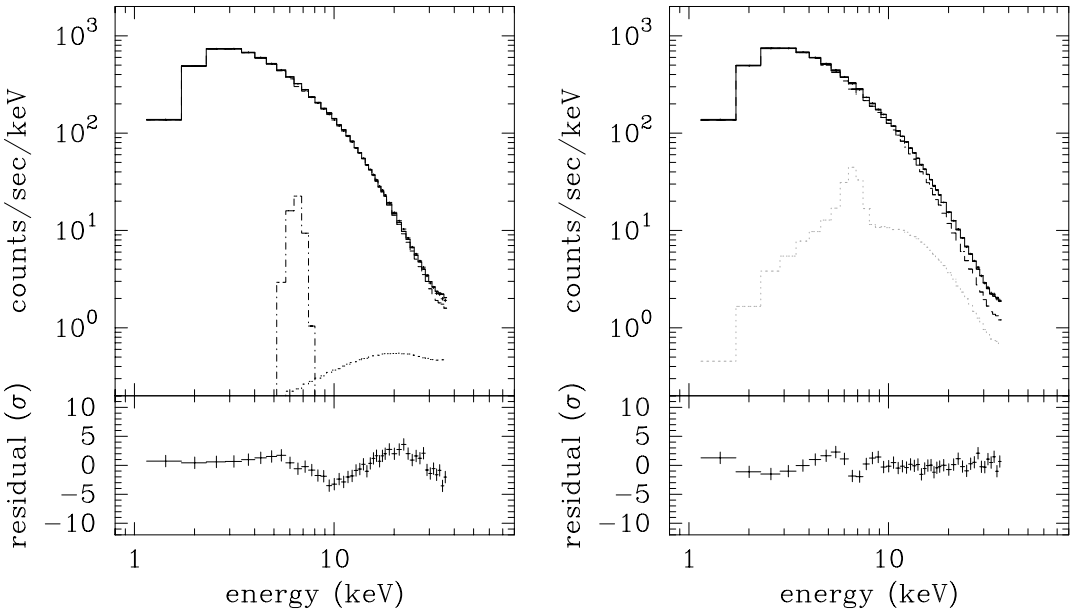

Figure 9.8: see Fig. 9.7. (*left*) The partial absorption (covering) model. (*right*) The reflection (albedo) model.

Comptonization Model

First, the two time averaged spectra are fitted with a Comptonized blackbody model with all free parameters except the column density of the interstellar absorption, and unacceptable results are obtained (χ^2/d.o.f. = 609.8/42 (1987) and χ^2/d.o.f. = 334.3/36 (1990)). In these fits, an iron line structure is recognized in the residuals between the observational spectra and the model spectra. If a gaussian model is provided with the model, significant improvements in χ^2 are found in both the fits (χ^2/d.o.f. = 532/40 (1987) and χ^2/d.o.f. = 188.3/34 (1990)), but large structures in the residuals still remain.

Next, the Comptonized blackbody plus power law model is applied to the spectra on the analogy of the fits to the spectra of the shots. In the fits to the spectrum in 1987, the parameters keT_{bb}, keT_e, and τ of the Comptonized blackbody and α of the power law are fixed at the values obtained in the fits to the spectra of the shots, and only normalization parameters are free. Though these parameters in 1990 are unknown, as a first step, the parameters of the Comptonized blackbody are fixed at the same values. In some cases, the addition of an iron line near 6.4 keV to the models results in significant improvements in χ^2. One of these results is shown in the left panel of Fig. 9.9. These best-fitting parameters are summarized in Table 9.5. As expected, if the parameters are fixed, the soft energy spectrum is substantially expressed by these models in spite of the fixed column density of the interstellar absorption, but large residuals remain at the high energies. One should remind that the timing analyses and hardness ratios require a hard spectral component. It should be noted that the edge-like structure at energy 8–20 keV changes to a large undulation if the photon index of the power law is free (right panel of Fig. 9.9).

There are two ways to go a next step (to obtain acceptable fits). One way is to thaw all the parameters. The obtained parameters of the shots are certainly typical values for the shots at those duration (0.5 sec before and after the peak intensity). As shown previously, however, these parameters vary in time. In addition, the parameters in 1990 may be different from those in 1987. The spectra are represented by this model with all the parameters free, and their results are shown in Fig. 9.10 and Table 9.5. Clearly, both the spectra in 1987 and 1990 are well represented by the model. In this model, however, the photon indices are so small that each component is unlikely to stand for the pure spectra of the shot in the rise and decay phase any longer. Note that the Comptonized blackbody component and the power law component are crossing at energy around 10 keV, resulting in the disappearance of the absorption features.

The other way to obtain acceptable fits reasonably is to leave the parameters fixed and add

Table 9.5:
BEST-FITTING PARAMETERS TO THE TIME AVERAGED SPECTRA
WITH THE COMPTONIZED BLACKBODY PLUS POWER LAW MODEL[a,b]

Data	Comptionized Blackbody					
	$Flux$[c]	kT_{bb} [keV]	kT_e [keV]	τ		
1987	8.4 ± 0.2	0.22 (fixed)	46 (fixed)	0.56 (fixed)		
	8.5 ± 0.2	0.22 (fixed)	46 (fixed)	0.56 (fixed)		
	11.9 ± 0.4	0.22 (fixed)	46 (fixed)	0.56 (fixed)		
	12.5 ± 0.2	0.22 (fixed)	46 (fixed)	0.56 (fixed)		
	2.0 ± 0.4	0.169 ± 0.003	49 ± 2	0.65 ± 0.04		
	2.1 ± 0.1	0.162 ± 0.001	45 ± 1	0.58 ± 0.01		
1990	16.6 ± 0.7	0.22 (fixed)	46 (fixed)	0.56 (fixed)		
	17.4 ± 0.6	0.22 (fixed)	46 (fixed)	0.56 (fixed)		
	2.0 ± 0.7	0.153 ± 0.006	43 ± 3	0.66 ± 0.08		
	1.7 ± 0.3	0.160 ± 0.001	41 ± 1	0.63 ± 0.01		
Power Law		Gaussian[d]			χ^2_ν	
A	α	$Intensity$ [c/s]	E_{cen} [keV]	$E.W.$ [eV]	(d.o.f.)	
4303 ± 34	1.49 (fixed)	—	—	—	11.1 (44)	
4286 ± 34	1.49 (fixed)	20 ± 155	6.26 ± 0.24	86 ± 670	11.2 (42)	
2951 ± 123	1.378 ± 0.012	—	—	—	7.03 (43)	
2664 ± 27	1.348 ± 0.003	35 ± 12	6.32 ± 0.05	156 ± 54	5.32 (41)	
530 ± 109	0.96 ± 0.05	—	—	—	2.84 (40)	
1065 ± 16	1.107 ± 0.005	40 ± 7	6.31 ± 0.03	388 ± 68	0.95 (38)	
1972 ± 159	1.28 ± 0.02	—	—	—	4.84 (37)	
1696 ± 141	1.23 ± 0.002	48 ± 10	6.39 ± 0.03	213 ± 45	3.27 (35)	
964 ± 196	1.09 ± 0.04	—	—	—	2.61 (34)	
1229 ± 22	1.133 ± 0.005	47 ± 22	6.46 ± 0.06	420 ± 196	1.36 (32)	

a All uncertainties are quoted at the 90 % confidence level.
b The column density of the interstellar absorption is fixed at 6×10^{21}.
c Bolometric flux [10^{-9} erg/s/cm^2] is shown.
d The width of the gaussian is assumed to be very narrow.

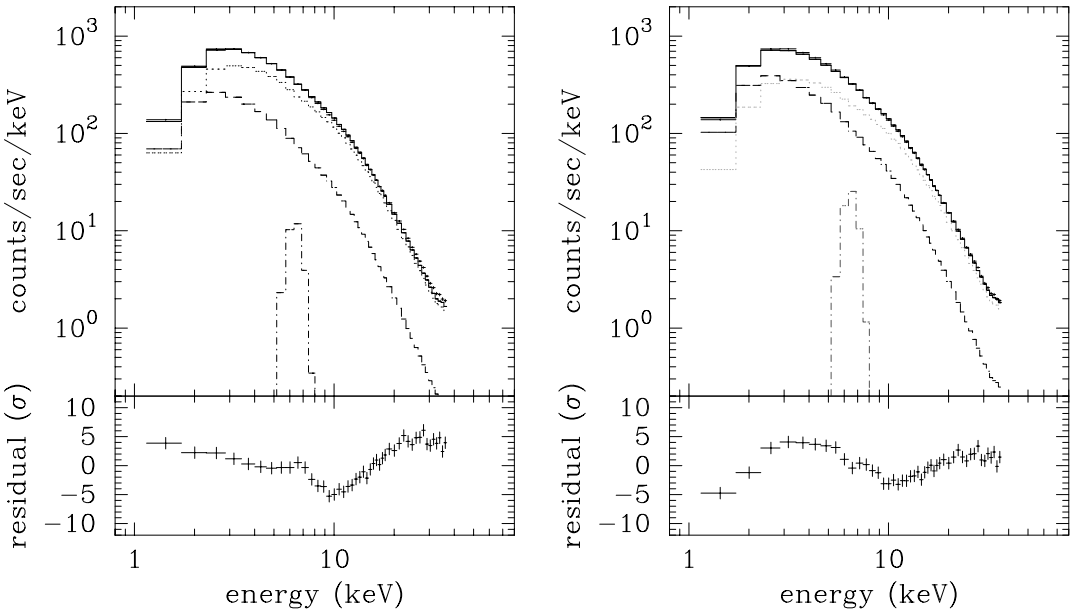

Figure 9.9: Results of the fits to the time averaged spectrum in 1987 with a Comptonized blackbody (dashed line) plus power law (dotted line) plus gaussian (dashed-dotted line) model. (*left*) keT_{bb}, keT_e, τ of the Comptonized blackbody and α of the power law are fixed at those obtained in the fits to he spectra of the shots. (*right*) The same of the left figure but α of the power law is free.

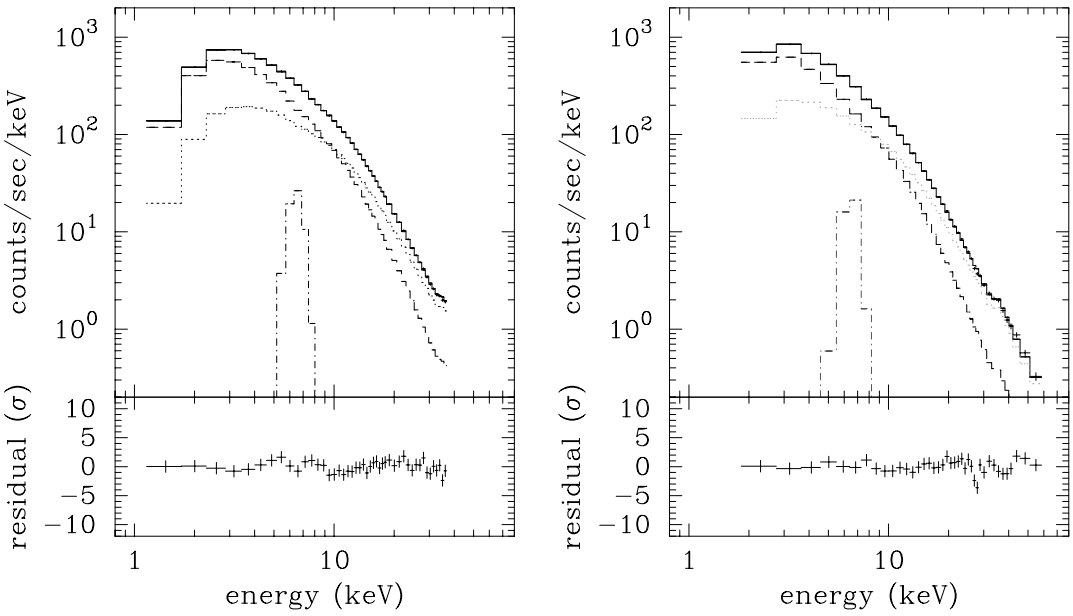

Figure 9.10: Results of the fits to the time averaged spectra in 1987 (*left*) and 1990 (*right*) with a Comptonized blackbody (dashed line) plus power law (dotted line) plus gaussian (dashed-dotted line) model with all the parameters free.

one more component, which have a hard spectral component. That is, each component purely represents each spectrum of the shots and the other (steady) component. If a hard power law spectrum is assumed as the hard component, fits with this model do not give acceptable fits. These results are shown in Fig. 9.11, and tabulated in Table 9.6. Note that the hard power law component (dashed-dotted lines) contributes to the higher spectra similar to the reflected power law component in the reflection model (Fig. 9.8). Acceptable fits are obtained if some of these parameters are free (Table 9.6), but this is not the first aim of this model. In all the fits, significant improvements in χ^2 are found by adding a gaussian function at energy around 6.4 keV.

Multi-Power Law Model

As shown previously, the energy spectrum of the shots can be also represented by the blackbody plus power law model. Fits to the spectra with the blackbody plus two power law with photon indices fixed at 1.75 and 1.49 do not give acceptable results at all. However, if only one photon index is fixed at 1.75 to represent the spectrum of the shots in the rise phase, the spectra are well described by this model. These results are plotted in the left panel of Fig. 9.12, and summarized in Table 9.7. The iron line is necessary to better fit the spectra in this case, too. The power law with the photon index 1.75 dominates the spectra at all the energies. This is not expected from the results in the previous chapters. Thus, this result is unlikely to present the real case.

If all the parameters are free, we obtain acceptable fits in both the spectra. These results are also shown in the right panel of Fig. 9.12 and in Table 9.7. In this case, unexpected photon indices, $\sim$ 1 and 2, are obtained, but the spectra are well represented by the only two powers. Especially, the broad absorption feature and the soft excess are completely expressed. (The blackbody component is not always necessary.) These models will be discussed in §10.3.1.

9.2.3 PHA Ratios

To summarize the results in this chapter, PHA ratios of the spectra to the models, which seem to be important, are shown in Fig. 9.13 in order of their appearance in this chapter. The PHA ratios clearly show residuals structures of these models. The spectra used in all the panels except the 3rd panel are the time averaged ones in 1987 and 1990. Each result is indicated by the opened circles and points, respectively. Note that they are very similar tendency in all the models. The models are the best-fitting ones shown previously, and written in the panels by

Table 9.6:
BEST-FITTING PARAMETERS TO THE TIME AVERAGED SPECTRA
WITH THE COMPTONIZED BLACKBODY PLUS TWO POWER LAW MODEL[a,b]

Data	Comptionized BB[d]	Power Law	
	Flux[c]	A_1	α_1
1987	10.5 ± 0.3	3721 ± 57	1.49 (fixed)
	7.5 ± 0.7	5284 ± 409	1.79 ± 0.04
1990	13.0 ± 0.7	3335 ± 178	1.49 (fixed)
	2.6 ± 3.5	8519 ± 1970	2.09 ± 0.14

Power Law		Gaussian[e]			χ^2_ν
A_2	α_2	*Intensity* [c/s]	E_{cen} [keV]	*E.W.* [eV]	(d.o.f.)
5.4 ± 1.7	0.01 ± 0.08	37 ± 7	6.30 ± 0.04	164 ± 31	2.95 (41)
371 ± 86	0.89 ± 0.05	37 ± 11	6.39 ± 0.04	168 ± 50	1.14 (39)
14 ± 11	0.23 ± 0.20	38 ± 10	6.41 ± 0.05	167 ± 44	1.97 (34)
131 ± 540	1.12 ± 0.10	36 ± 29	6.43 ± 0.30	251 ± 202	1.36 (33)

a, b, c see Table 9.5.
d The other parameters are fixed at $T_{bb} = 0.22$ keV, $T_e = 46$ keV, and $\tau = 0.56$.
e The width of the gaussian is assumed to be very narrow.

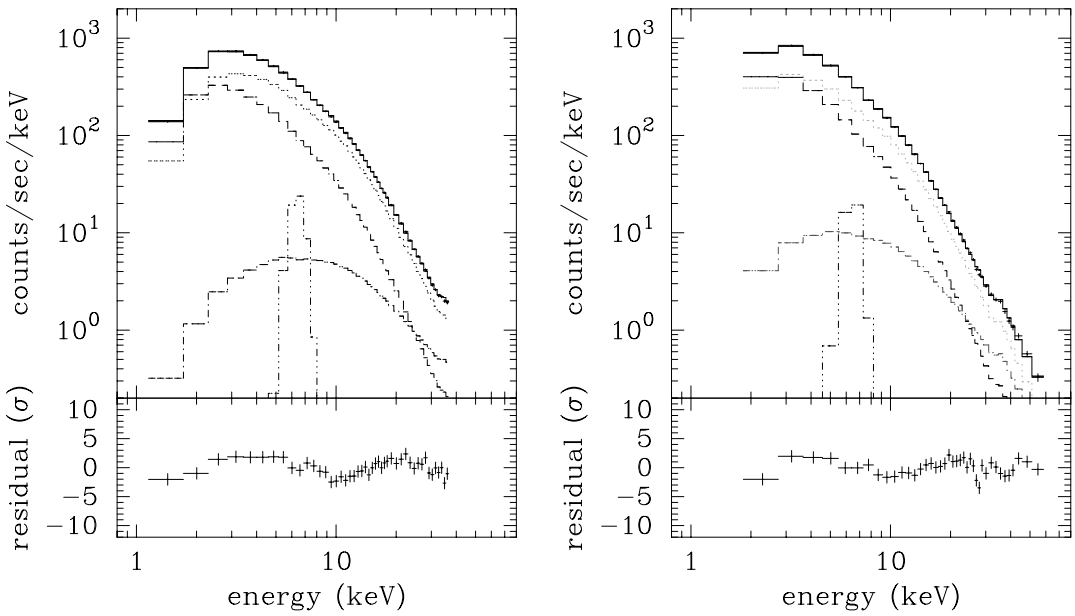

Figure 9.11: Fits to the spectra in 1987 (*left*) and 1990 (*right*) with the Comptonized blackbody (dashed lines) plus power law (dotted lines) plus gently power law (dashed-dotted lines) plus gaussian (dashed-dotted-dotted lines) model. Each component stands for the spectrum of the shots in the rise phase, that in the decay phase, a spectrum of the other (steady) component, and an iron line.

Table 9.7:
BEST-FITTING PARAMETERS
TO THE TIME AVERAGED SPECTRA WITH THE TWO POWER LAW MODEL[a,b]

Data	Blackbody		Power Law	
	$Flux^c$	kT_{bb} [keV]	A_1	α_1
1987	3.5 ± 3.2	0.241 ± 0.020	8048 ± 114	1.75 (fixed)
	3.8 ± 1.1	0.209 ± 0.005	8438 ± 102	2.050 ± 0.008
1990	1.4 ± 2.7	0.33 ± 0.04	8299 ± 89	1.75 (fixed)
	86 ± 102	0.136 ± 0.009	9430 ± 116	1.961 ± 0.007

Power Law		Gaussian[d]			χ^2_ν
A_2	α_2	*Intensity* [c/s]	E_{cen} [keV]	*E.W.* [eV]	(d.o.f.)
85 ± 20	0.57 ± 0.07	35 ± 8	6.31 ± 0.05	164 ± 31	1.44 (39)
1277 ± 18	1.152 ± 0.004	39 ± 12	6.39 ± 0.03	168 ± 50	1.05 (38)
59 ± 9	0.48 ± 0.04	35 ± 10	6.41 ± 0.05	167 ± 44	1.80 (33)
602 ± 14	0.981 ± 0.007	32 ± 16	6.58 ± 0.04	251 ± 202	1.44 (32)

a, b, c see Table 9.4.
d see Table 9.5.

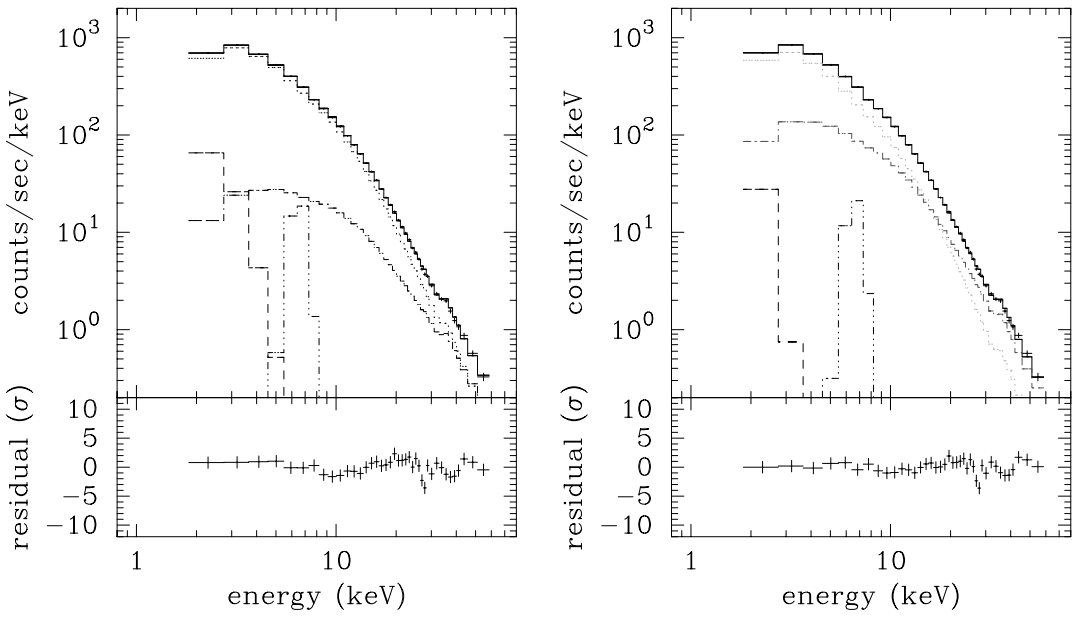

Figure 9.12: Fits to the time averaged spectrum in 1990 with the blackbody (dashed lines) plus two power law (dotted and dashed-dotted lines) plus gaussian (dashed-dotted-dotted lines) model. (*left*) The photon index of the steeper power law component is fixed at 1.75. (*right*) All the parameters are free.

the abbreviations, "*pow*" = power law, "*abs*" = interstellar absorption, "*cbb*" = Comptonized blackbody, "*gau*" = gaussian, and "*bbd*" = blackbody. Parameters in some model components are fixed at $keT_{bb} = 0.22$ keV, $keT_e = 46$ keV, $\tau = 0.56$ for the Comptonized blackbody model, $\alpha = 1.49$ for the power law model, and $\log N_H = 21.8$ for the interstellar absorption. These components with fixed parameters are indicated by the subscript, "*fx*", after the abbreviations.

The model spectrum used in the 2nd panel has not been shown before. This is the model that photon indices of the power law are fixed at the same values as those of the model in the first panel, but the column density in this fits are fixed at $\log N_H = 21.8$. Thus, if the column density expected from the distance to Cyg X-1 is valid, this is a true residual structure in fitting with a single power law. Note that the structure does not look like a broad edge-like structure, any longer.

The ratios in the 3rd panel are those of the spectra of the excess shot components in the rise and decay phases (No. 3 & 4 in §9.1.2) to a power law with the interstellar absorption ($\log N_H = 21.8$) model. The photon index of the power law is also fixed at the same value as that in the 1st panel. The results in the rise and decay phases are indicated by the opened circles (errors are omitted) and filled circles with 1 σ errors, respectively. Obviously, the ratios in the rise phase show large soft excess below $\sim$ 10 keV. This strongly suggests that the ignorance of this soft component leads the soft excess having appeared in previous observations in fitting spectra with a single power law.

We can find from the 4th panel that a high energy tail remains as expected if the spectra are represented by the only spectra of the shots (in this case, the Comptonized blackbody plus power law model with fixed parameters), implying that a high energy component is necessary. The lack of this hard component is filled if a very hard power law exists (6th panel), or if average spectra of the shot component and the other component are much more softer and/or harder than those obtained from the excess shot component (5th and 7th panels).

Thus, the existence of 2 or 3 components in the X-rays from Cyg X-1 is confirmed in the energy spectrum, too. These results will be discussed in §10.3.1.

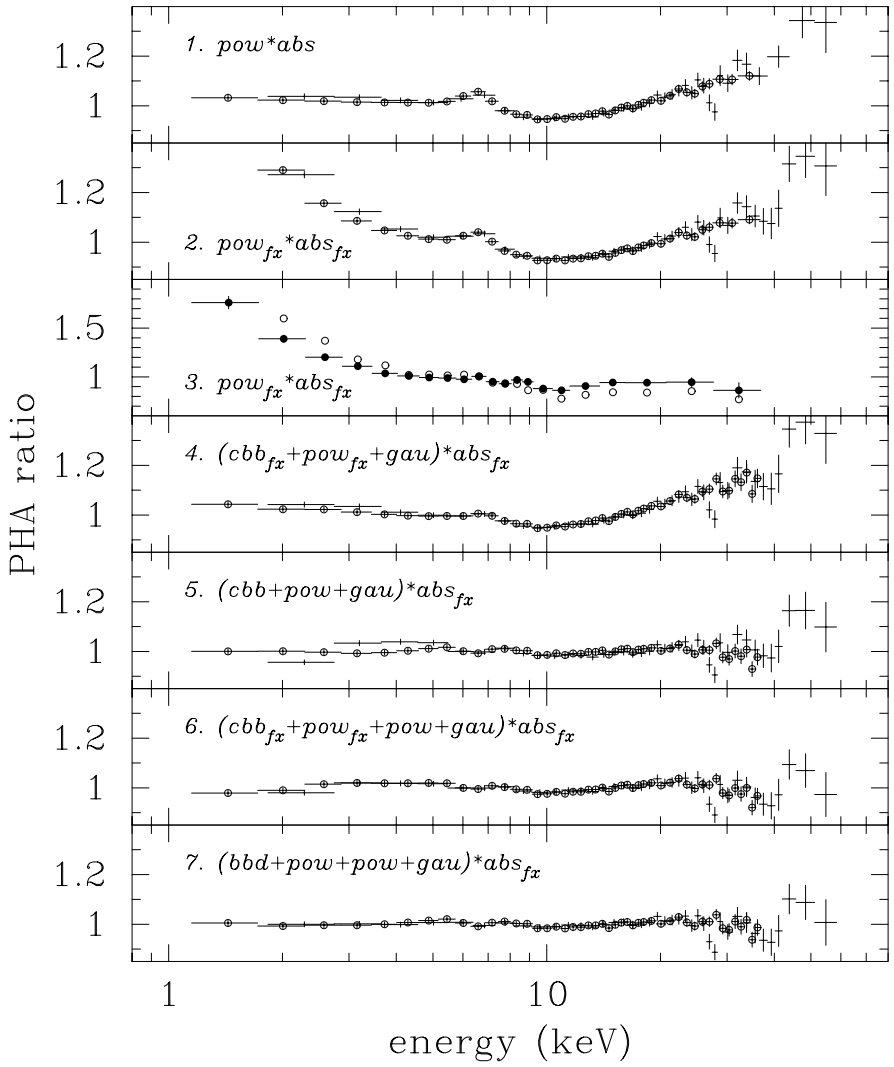

Figure 9.13: (*3*) PHA ratios of the spectra of the excess shot component in the rise (opened circles) and decay phases (filled circles with 1 σ errors) to power law spectra. (*the others*) PHA ratios of the time averaged spectra in 1987 and 1990 to model spectra. Ratios in 1987 are indicated by the opened circles. The abbreviations after the number in each panel means that "*pow*" = power law, "*abs*" = absorption, "*cbb*" = Comptonized blackbody, "*gau*" = gaussian, and "*bbd*" = blackbody. Their subscript, fx, indicates that all the parameters except the normalization are fixed (see text). Related figures are (*1*) Fig. 9.2 left, (*3*) cf., Fig. 9.4 (3,4), (*4*) Fig. 9.9, (*5*) Fig. 9.10, (*6*) Fig. 9.11, (*7*) Fig. 9.12.

Chapter 10

Discussion

The new analysis method, the superposition of X-ray shots, have revealed many properties of the X-ray shots, and those properties have been demonstrated to be consistent with the results of the power spectrum analyses. In this chapter, comparisons with previous reports, implications of those properties and remaining problems are described. Finally, physical interpretations of the shots are discussed.

10.1 Comparison with Results of Previous Timing Analyses

The properties of the superposed shots are average ones of shots we selected. The consistency with the results of the power spectrum analysis supports the fact that the superposed shots have all the average properties of the shots. In this respect, the superposed shots can be thought to be identical to shots which have been investigated in previous shot noise models (Lochner et al. 1991 and the references therein).

10.1.1 Comparison with Shot Noise Models

General Profile

The properties of the superposed shots are qualitatively consistent with those in previous shot noise models (§2.3.2), and further informative. For instance, the rise and/or decay of the shots have been *assumed* to be a single exponential in many previous shot models, but the superposed shots *show* that both are approximately represented by the sum of two exponentials. The difference between the observational data (ACF, or PSD) and model shots with a single exponential profile has been pointed out by Oda et al. (1976), Nolan et al. (1981), Meekins et al. (1984), and Miyamoto & Kitamoto (1989). Some of these authors showed the existence of two or more time constants in the time variability and attributed them to independent exponential

shots. But none of these authors demonstrate that the shots were represented by, for instance, the sum of the two exponentials.

The soft energy spectrum of the shots is consistent with a result of Ogawara et al. (1977) from a roket observation, but inconsistent with a result of Nolan et al. (1981) by *HEAO 1* observations. This conflict seems to arise from the difference of their observed energy bands. Further discussion will be done in relation to the energy spectrum in §10.3.1. Spectral hardening during the shots was first predicted by Miyamoto & Kitamoto (1989). However, they thought that it mainly occurred with increasing intensity. The superposed shots *show* that the spectral hardening rather takes place *at* and after the peak intensity.

The other fine structures and properties of the shots obtained here have not been predicted at all. This is mainly because the superposition method conserves not only the amplitude component in the power spectrum analysis and but also the phase component simultaneously. Therefore, the most superior point of the superposition method to these shot noise models is that *no assumption is required in the superposition method to make up the lack of the information* (§2.3.2).

Distribution of the Shot Duration

In some shot noise models, a power law distribution of a time constant of the shots were assumed (Meekins et al. 1984; Belloni & Hasinger 1990a; Lochner et al. 1992). Of course, as the superposed shot profile is an average one of shots, the time constant may be distributed, but not widely. To explain bends and/or slopes of PSDs in Cyg X-1, the previous authors assumed that each shot profile could be described by an exponential, of which a time constant was distributed between τ_a and τ_b corresponding to knee frequencies (the bends) in the PSDs. If so, a superposed shot should have an averaged time constant of them with a weight of their appearance rates, and never have the time constants, τ_a and τ_b. This completely conflicts with our results demonstrated in §7.1.1. Thus, the wide distribution model is ruled out. The stair-like structure in the diagram of hard X-ray time lags (Fig. 7.2) implying the existence of characteristic time constants also supports this conclusion (cf., Miyamoto & Kitamoto 1989).

Shot Parameters

The shot parameters have been described in terms of the shot noise model by Sutherland et al. (1978). Parameters in their exponential shot noise model are a rate of the shot occurrence λ, peak intensity h, time duration τ, and steady source C. Our analyses and recent results (ex.,

Belloni & Hasinger 1990a) requires at least the following 6 parameters: two time constants τ_a and τ_b, an intensity ratio of two exponentials A/B, peak distribution parameters D (1/sec) and p_{decay} (Negoro et al. 1994b), and steady source C. τ_a, τ_b, and A/B can be obtained from a PSD. D, p_{decay}, and C will be determined by a NPSD and others, but hard to get independently from current analysis methods unless some assumptions are made.

Fractal Phenomenon

It should be also noted that the existence of the characteristic time constants implies that the time variability in Cygnus X-1 is *not* a fractal phenomenon as sometimes discussed previously. This is also clear from the fact that these time constants hardly depend on the time resolution of data used (§6.2.1). (One of the most important characters of the fractal is the scale independence of events (Takayasu 1986).) Furthermore, it is demonstrated in §7.1.1 the PSD below $\sim$ 1 Hz contains certain 'signal', not '1/f noise' as the light curve of the quasar 3C273 (Press 1978). However, it is interesting to note that the rising profiles of the superposed shots are represented by the fractal function, $\propto 1/(\tau - t)^{\alpha}$. If $\alpha = 0.5$ (observed value $\simeq 0.7$), this function is the same one as Press deduced from a half-integral function of random noise to generate 1/f noise.

10.1.2 Time Variations of the Shot Profile

The characteristic time constants describing the shots seem to vary in different observations. The time constants of the superposed shot in 1987 are $\sim$ 50% larger than those in 1990. The intensity ratio of the two exponentials A/B in 1987 is 30 $\sim$ 40% smaller than that in 1990. This is consistent with the fact that, in the shot noise models, shot parameters in different observations are different (eg., Sutherland et al. 1978; Weisskopf et al. 1978; Nolan et al. 1981). We have demonstrated in §7.1.1 that these differences in the shot profiles result in larger NPSD values at frequencies below 0.2 Hz in 1987 than those in 1990 (cf. Miyamoto et al. 1992). From these facts, the variations of the break frequencies ($\nu_{b,kn}$ = 0.04-0.4 Hz and $\nu_{a,kn}$ = 1-6 Hz) in the *EXOSAT* observations (Belloni & Hasinger 1990a) seem to be due to the changes of the profile of the shots.

The sub-structures also vary in time. Especially, the broad bump at the relative time -3.7 sec in 1987 obviously appeared only for a few hours though the X-ray flux had not changed before and after the interval. While, the small bump at the relative time -1.85 sec in 1990 had been observed for three days. They may be different phenomena, but it is interesting

that both appeared near the beginning of the shots (or after the broad intensity decrease). A physical interpretation of the substrunctures will be discussed in §10.4.3. The effects of the sub-structures are also recognized in the observed PSD (§7.1.1). Belloni & Hasinger (1990b) reported from the *EXOSAT* observations that bumps in their PSDs appeared around 0.5 and 1.3 Hz on an occasion, and 0.9 and 2.0 Hz on another occasion. These frequencies are similar to those in 1990, 0.55 Hz and around 1 Hz. Thus, the bumps they found are likely to originate in the sub-structures of the shots.

10.2 High Frequency Component

The comparison of the profiles of the superposed shots with the observed power spectra leaves a problem, the existence of an unknown high frequency ($\gtrsim$ 1 Hz) component. Its features are summarized as follows: (a) In the PSD above 1 Hz, the observed PSD decreases roughly as $\nu^{-1.5}$, and slightly bends near 10 Hz (Kitamoto and Miyamoto 1989), while the PSD expected from the shot profile falls as ν^{-4}. (b) The total rms variability (Lewin, van Paradijs and van der Klis 1988) of this component in the 1990 observation is 16.4±1.0 % in the range 2.2 – 64 Hz, while that of all the component is 30.9 ± 2.4 % in the range 3.9×10^{-3} – 64 Hz (29.7 ± 2.4 % in 2.0×10^{-3} – 14 Hz). (c) The NPSD shows that the high frequency component has a relatively hard energy spectrum by contrast with the soft energy spectrum of the shots. (d) The time lags (cross spectrum) suggest that this hard energy spectrum has no clear time evolution. (e) The PSD model derived from the function representing a shot profile and an additional Lorenzian with $\nu_{Lz,kn} = 4.8 \pm 0.2$ roughly represents the observed PSD to the high frequencies at least 10 Hz.

Possibilities to produce a high frequency component are (1) the existence of additional one or two kinds of shots with short durations (< 0.1 sec, in this case, 33 ms $\simeq 1/2\pi\nu_{Lz,kn}$) (cf., Miyamoto & Kitamoto 1989), (2) peaks with power-law distributed durations (Meekins et al. 1984; Mineshige 1994b; cf., Press 1978) and (3) a component like a flat-top noise (FTN) in BHCs in the soft (very high) states, or a low frequency noise (LFN) in *Z* sources in the horizontal branch (van der Klis 1994). In addition, (4) sharp spikes such as millisecond bursts (Rothschild et al. 1974, 1977; Meekins et al. 1984), giving rise to many intensity gaps, may result in the high frequency component just like the Gibbs phenomenon that high frequency powers are necessary (but not enough) to represent a gap in a curve.

The possibility (3) may result from the other possibilities. But high frequency QPOs, which are often accompanied with the FTN or LFN (Dotani 1988; Hasinger & van der Klis 1989) were

not observed yet in the low (hard) state. Thus, the unknown high frequency component is unlikely to be identical to the FTN and/or LFN. For the possibilities (1), (2) and (4), previous and this analyzing methods can not answer this problem. One of the reasons is the difficulty in distinguishing the real source activities from the statistical count fluctuations.

It should be remained that the (steady) component with a harder spectrum is expected to exist from the soft energy spectrum of the shots (§6.3.1, 6.4). This component may be identical to the unknown high frequency component because both the components are expected to have a harder spectrum and smaller (and shorter) time variability than the shots.

10.3 Comparison with Results of Previous Spectral Analyses

10.3.1 Multi-Continuum Requirement

The spectrum of Cyg X-1 consists of at least 3 components. As shown in §6.3.1 and §9.1.2, the shots have a soft energy spectrum before the peak intensity (photon index $\alpha \simeq 1.75$ in power law fits), and the spectrum of the shots hardens just after the peak ($\alpha \simeq 1.62$). In addition, one hard spectral component is necessary for the lack of the hard component to produce the average spectrum. The observed time averaged spectra, however, could not be constructed by these components (§9.2.2). This seems to be because (1) the obtained parameters to describe the spectra of the shots are still approximate values for them, and/or because (2) the addition of a hard power law might not be appropriate. (Of course, there is no positive reason to support the power law model.)

Without the third component (hard power law), if the spectra were fitted with the multi-power law model (blackbody plus two power law plus gaussian model), in which all the parameters were free, gave acceptable fits in 95 % confidence (§9.2.2, Table 9.7). In those fits, the photon indices were around 2 and 1. These rather too large and small indices no longer present each spectral component of the shots, which means that the representation of these function is not supported by the observation. The simple Comptonization model (Comptonized blackbody plus power law plus gaussian model) with all the parameters free (§9.2.2, Table 9.5) also gave a photon index ~ 1.

Such a hard power law component has not been observed in higher energies ($E \gtrsim 100$ keV) band in all the BHCs. With the exception of a few case (Cyg X-1, Ling et al. 1987; 1E1740.7-2942. Sunyaev et al. 1990), most of spectra of BHCs exponentially decrease at higher energies (e.g., Sunyaev & Trumper 1979; Liang & Nolan 1984). Fortunately, SIGMA telescope on board

GRANAT, covered the energy range 35 keV – 1.3 MeV, also pointed at Cyg X-1 during 23–24 March 1990 (Salotti et al. 1992), almost 1 month before the second observation with *Ginga*. At that time, the photon index below 200 keV was ~ 1.94 (Salotti et al. 1992). Furthermore, the shot fraction in §8.1 shows that the soft component of the shots is not so much (~ 10 %), while the soft component in these multi-power law and simple Comptonization models dominates the spectrum below 10 keV. From these facts, these models are unlikely to represent the true spectrum of Cyg X-1 though they give acceptable fits.

The SIGMA observation reported that the shot noise behavior was not recognized above 115 keV (Salotti et al. 1992), suggesting that the steady component dominates over the other components at the high energies. Liang & Dermer (1988) and Liang (1990) also claimed that there had to be a very hot ($kT_e \sim$ 350–400 keV), pair-creation dominant region to produce a significant γ -ray bump discovered by *HEAO 3* (Ling et al. 1987) though this component was not present at all the time (Ling et al. 1987) Thus, from other observations, another hard component has been expected to exist.

From the above arguments, the results of the Comptonization model including a very hard component shown in Fig. 9.11 is most likely: a "soft component" which significantly contributes to the spectrum below ~ 10 keV especially at higher intensity, a "hard component" dominant at energies of ~ 10 keV to at least ~ 60 keV, and a "very hard component" probably dominant at further higher energies. The "steady component" in the previous chapters (sections) is presumably the hard and/or very hard component.

If so, Fig. 9.10 indicates that most of the radiative energy in the X-ray band is released as the hard component. The hardness ratios (§6.3.1, 6.3.2) suggest that those X-rays are emitted after the peak intensity of the shots. Thus, the shots may supply their energy to the hard X-ray emission region.

The above conclusion also suggests the existence of a pivoting point at the energy around 10 keV in the spectrum. Thus, at higher intensity (during a shot), the spectrum looks like being soft at energies where the soft component is dominant ($E \lesssim 10$ keV), while being hard at energies where the hard component is dominant ($E \gtrsim 10$ keV). This conjecture may explain the confliction discussed in §10.1.1. The rocket observation by Ogawara et al. (1977) and the *EINSTEIN* observation by Balucińska & Chlebowski (1988), and this observation indicate that the shots have a soft spectrum. While, the high energy observation with *HEAO I* (Nolan et al. 1981) showed an opposite result. These observation were certainly carried out in different epochs. However, the energy ranges covered by these experiments were also different; the energy

range of *Ginga* was 1.2–36 keV in 1987 and 1.2–58 keV in 1990, that of the roket was 1.5–25 keV, and that by *EINSTEIN* was 1.2–20 keV, while that by *HEAO I* was 10–140 keV. Future wide band observations with *XTE* and *Astro-E* will answer this question.

10.3.2 Soft X-ray Excess

A soft excess below a few keV (§2.3.1) is recognized in our observations if the column density of the interstellar absorption is fixed at 6×10^{21} atoms/cm^2, expected from the optical/UV measurements, and the spectrum is fitted with a single power law model. Kitamoto et al. (1989a) and Balucińska & Hasinger (1991) showed that the observed large amount of soft excess components could not be explained by the only dust scattering component.

The spectral analysis of the shots have demonstrated that the soft excess is not an additional component below a few keV, but the main "soft component" exhibiting highly time variability. The soft excess component could be described by a Comptonized blackbody model or a blackbody plus steep ($\alpha \simeq 2$) power law model. (Barr & van der Woerd (1990) regarded only a blackbody component as a soft excess component in the latter model.) Each temperature of the thermal components were about 0.22 keV and 0.27 keV. This difference comes from the discrepancy between the color and effective temperatures in the Comptonized blackbody model, as mentioned in §9.1.2.

A similar blackbody temperature ($\sim$ 0.25 keV) was reported by Balucińska & Hasinger 1991 from *EXOSAT/ME* observations. Barr & van der Woerd (1990) also showed that the soft excess component was described by a broad emission line at $\sim$ 0.7 keV, or optically thin thermal plasma with a temperature $\sim$ 0.26 keV. Probably, these are the same component. Balucińska & Hasinger (1991) argued that this low temperature component originated in the accretion disk with hot plasma. Terada et al. (1995) also speculated in their spectra analysis of a X-ray transient GS2000+25 that a very low temperature ($\sim$ 0.2 keV) of the Comptonized blackbody model indicated a temperature near the innermost radius of an accretion disk around a massive star (BH). Certainly, the maximum disk temperature of the optically thick disk is at $49r_{in}/36$, where r_{in} is the innermost radius of the accretion disk, and expressed as (Shakura & Sunyaev 1973)

$$\begin{aligned} kT_{max} &= k\left\{\frac{3GM\dot{M}}{8\pi\sigma(49r_{in}/36)^3}\left(1-\sqrt{\frac{r_{in}}{49r_{in}/36}}\right)\right\}^{\frac{1}{4}} \\ &= 0.17keV\left(\frac{M}{10M_\odot}\right)^{-\frac{1}{2}}\dot{M}_{17}^{\frac{1}{4}}, \end{aligned} \tag{10.1}$$

where $\dot{M}_{17} = \dot{M}/10^{17}$ g/sec. Thus, the disk origin is very likely. Furthermore, from the bolometric flux of the blackbody or Comptonized blackbody component, the luminosity of the component is found to be 10^{36}–10^{37} erg/s provided the distance to Cyg X-1 is 2.5 kpc, and the radius in assuming a circular emission region is $\sim 8 \times 10^6$ cm for the blackbody case, and $\sim 1.5 \times 10^7$ cm for the Comptonized blackbody case. It is surprising that the amount of the latter emission region is consistent with that of the inner part of the accretion disk around the central star with ~ 10 $M_\odot$ in spite of a minor contribution of the modified blackbody component to the spectrum. These results strongly suggest that seed photons of the shots originate from a low temperature disk. It can be concluded that the observed soft excess component can be interpreted by the disk component and its Comptonized component, which are the soft spectrum of the shots.

It should be noted that there is another soft excess component, which may be understood in terms of the interstellar dust scattering (for Cyg X-1 Kitamoto et al. 1989a; Balucińska and Hasinger 1991; for GS2023+338 Inoue 1992; see §2.3.1). Time variability of X-rays scattered in the halo will be smeared and lag behind that of X-rays observed directly over several hours (Kitamoto et al. 1989a). Thus, the scattering component is expected to show relatively small time variability. This is opposite to our results, indicating that most of the observed soft excess component is not due to the dust scattering.

10.3.3 Reflection Model

The observed spectral variation also constrains the application of reflection (albedo) models (Lightman & While 1988; Guilbert & Rees 1988). One must recall that the fundamental assumption of the reflection models is that incident X-rays to cold matter have a power law spectrum with a *constant* photon index (Lightman and White 1988). Under this assumption, the edge and high energy bump structures are reproduced.

This analyses, however, show that the spectrum of Cyg X-1 includes power law spectra with a variety of photon indices of ~ 1.75 to ~ 1.62 (1.49) (§9.1.2), and that some spectral models well reproduce the broad edge-like structure at energies 8–20 keV (§9.2.2), which will reduce the necessity of the reflected component.

The very hard power law component in the 3 component fits shown in Fig. 9.11 is similar to the reflection component shown in Fig. 9.8. Absorption features are always recognized in all the PHAs of the excess shot component (Fig. 9.13) though they do not look like an edge structure. If the very hard component in the spectrum is a reflection component, its ratio to the directly component at 6 keV (Marshall et al. 1994) is about 2%. While ratios in previous

reports are 7-8 % (from Fig. 3b of Done et al. 1990) and $8.7^{+8.9}_{-4.6}$ % (Marshall et al. 1993). Ratios in the same model in this observations (§9.2.1, Fig. 9.8) also show $\sim 5\%$. In this thesis, only one reflection model (Lightman & White model modified by Kitamoto) is examined, but a variety of models (Done et al. 1990; George & Fabian 1991; Matt, Perola, & Piro 1991) present similar ratios (Marshall et al. 1993).

Done et al. (1990) argued that the corresponding solid angle subtended by the reflecting material was $\Omega/2\pi = 0.57 \pm 0.07$. The small ratio at 6 keV in the multi-continuum model in this thesis indicates much smaller angle, $\Omega/2\pi = 0.1 \sim 0.3$. Taking account of the inclination angle of this binary system, $\sim 30^\circ$ (Gies & Bolton 1982), models are ruled out that show a large solid angle subtended by an optically thick disk from a major emitting region. For instance, in the coronal accretion disk models (e.g., Liang & Price 1977), a major emitting region must not be above the disk. In the geometrically thick accretion disk models (e.g., Paczinski & Wiita 1980), the optically thick torus must not have a large solid angle from the Earth.

The fact that the excess shot component does not have the very hard component (§9.1.2) also restricts the emitting region of the shots. If the reflected component of the shots is observed, it will lag behind the direct component as follows. γ-ray photons incident to cold matter reduce their energy through Compton recoils, and some of them appear from a disk surface as a hard X-ray bump. Incident X-rays near 10 keV are elastically scattered by electrons in the disk, and a small amount of them escape from the disk with almost the same energy. Thus, the time it takes for the hard X-ray bump to appear is characterized by time scales in which photons go to the interior of the disk, and random-walk from there to the surface. The latter (random-walk) time scale is called the thermal time scale, τ_{thrm}. In the cold matter (disk), the dominant pressure is thought to be gas pressure, and electron scattering is important for photons with $E \geq 10$ keV. Under these conditions, the thermal time scale is estimated as (c.f., Lightman 1974a)

$$\begin{aligned} \tau_{thrm} &\lesssim \frac{\kappa_{es}\Sigma h}{2c} \\ &= \frac{1}{c}\sqrt{\frac{\kappa_{es}\dot{M}}{3\pi\alpha\Omega}} \\ &= 0.19\,\mathrm{ms}\left(\frac{r}{3r_s}\right)^{\frac{3}{4}}\left(\frac{0.1}{\alpha}\right)\left(\frac{M}{10M_\odot}\right)\dot{M}_{17}^{\frac{1}{2}}, \end{aligned} \tag{10.2}$$

where κ_{es} ($= 0.40$ cm^2 g^{-1}) is electron scattering opacity, Σ and h are the surface density and half-thickness of the disk, respectively, α ($\lesssim 1$) is the viscosity parameter by Shakura & Sunyaev (1973), and Ω is the Keplerian angular frequency, not a solid angle here. Thus, even $r = 1000r_s$, $\tau_{thrm} \sim 10$ ms, which is shorter than the traveling time of incident photons from the center to

there, ~ 0.1 s. If so, the hard reflected photons must be observed during the shots. The failure of detecting hard X-ray component implies that X-rays of the shots do not reprocessed; the solid angle subtended by the reflecting material from an emitting region of the shots is very small.

To sum up, the observed absorption-like structure at energies 8–20 keV is though to be produced by a superposition of some spectra, and the role of the reflected component is less important than previously thought. This absorption-like structure shows a far different profile from that of an absorption edge of irons with a single temperature, and a smeared, broad profile (Ebisawa 1991). Done et al. (1992) also pointed out that a single temperature thermal Compton model was not well fit to a broad-band spectrum. These observational facts support this conclusion.

It should be noted that this conclusion may apply to spectra of AGNs. Because spectra of AGNs also vary with intensity (e.g., 3C120, Halpern 1985; NGC 4151, Lawrence et al. 1985). A Ginga-12 spectrum in Pounds et al. (1990) is a composite spectrum of power laws with photon indices of 1.63 to 2.1. Some of the AGNs (Mkn 335, MCG-6-30-15, NGC 4051, NGC 5548) show significant soft excess (Turner & Pounds 1989). A spectrum fit with a power law plus reflection model gives a ratio of the reflection component to the direct component ~ 8 % (Fig. 2 of Pounds et al. 1990). These are very similar to the case of Cyg X-1 discussed above. Matsuoka et al. (1990) carefully analyzed spectra of NGC 4051 and MCG-6-30-15 sorting by intensity to avoid the above argument. In that case, the reflection model also gave good fits to the spectra. However, their spectra were not produced from the excess component of the "large" shots. Thus, the observed reflected components in AGN spectra are still doubtful.

10.4 Physical Interpretation of the X-ray Shots

As none of theoretical models have predicted shot properties in detailed enough to be compared with the obtained ones (§2.4), first of all, we focus our discussion on the relationship between the magnitude (peak intensity) of the shots and the duration. It is established from this analyses that the time duration of the shots is almost independent of the peak intensity though they vary on time scales of years (or months).

10.4.1 Disk Instability Models

For the application of the disk instability models to observed time variability, some problems have been pointed out. Piran (1978) and Pringle (1981) warmed that disk instabilities might be a breakdown of the α disk model. Furthermore, the standard α disk model predicts

that a radiation pressure-dominanted region is formed at a high accretion rate, and instabilities set in (Thorne & Prince 1975). While, observations of some X-ray novae show that the inner radius of the optically thick disk, which is understood as the gas pressure-dominated disk in terms of the α disk model, is steady under the change of X-ray flux by two orders of magnitude (Tanaka 1989), and that large time variations occur at relatively lower X-ray flux (Inoue 1993, Terada 1994).

To the best of our knowledge, however, the disk instability models are undoubtedly one of the candidates to explain the observed time variations. That is why, we will compare them with the obtained shot properties. In the α viscosity models, it is known that the radiation pressure-dominanted region of an accretion disk is thermally and dynamically unstable (Pringle, Rees & Pacholczyk 1973; Lightman & Eardley 1974; Shibazaki & Hoshi 1975; Shakura & Sunyaev 1976; Piran 1978, see §2.4.1). According to Shakura & Sunyaev (1976) and Piran (1978), the instability arising from a perturbation with the radial length scale Λ grows with time, namely,

$$\frac{\delta Q^+}{Q_0^+} = exp\left(\frac{t}{\tau_{ins}}\right) sin\left(\frac{r}{\Lambda}\right) \tag{10.3}$$

where Q_0^+ is the energy production rate per unit surface area in the stationary disk, represented by $\frac{3}{8\pi}\frac{GM}{r^3}\left(1-\sqrt{\frac{r_{in}}{r}}\right)$ where r and r_{in} are the radial distance from the central star and the innermost radius of the accretion disk, respectively, and M is the mass of the central star (Shakura & Sunyaev 1973). The growing time constants τ_{ins} of the thermal and viscous instabilities, denoted by $\tau_{thrm.ins}$ and $\tau_{visc.ins}$ respectively, can be represented by

$$\tau_{thrm.ins} = f(\beta,\Lambda)\frac{1}{\alpha\Omega}, \tag{10.4}$$

$$\tau_{visc.ins} = g(\beta,\Lambda)\frac{1}{\alpha\Omega}\left(\frac{\Lambda}{h}\right)^2 \tag{10.5}$$

where f and g are functions of a pressure ratio β $(= p_{rad}/p)$ and Λ, or functions of only β for the large perturbations, e.g., $\Lambda/h \gg 1$. Note that these time scales strongly depend on the radius r where instabilities occur, $\tau_{ins} \propto r^{\frac{3}{2}}$. Furthermore, under the standing wave condition $r > \Lambda \geq 4h$, an exact calculation leads that $\tau_{visc.ins} \geq \tau_{thrm.ins}$.

An observed intensity fluctuation $\delta F(r,t)$ must reflect a fluctuation of the radiative cooling rate δQ^- which has the following relation, $\delta Q^- = c\delta Q^+$ where $c \leq 1$ ($c = 1$ in the case of the viscous instability). Using this relation and Eq. (10.3), $\delta F(r_p,t)$ due to a perturbation having the maximum at r_p $(= (\pi/2 + 2n\pi)\Lambda$, where n is an integer) can be roughly represented by

$$\delta F(r_p,t) \simeq \int_{r_p-\frac{\Lambda}{2}}^{r_p+\frac{\Lambda}{2}} \delta Q^- 2\pi r dr \propto \int_{r_p-\frac{\Lambda}{2}}^{r_p+\frac{\Lambda}{2}} \frac{1}{r^3}\left(1-\sqrt{\frac{r_{in}}{r}}\right) exp\left(\frac{t}{\tau_{ins}}\right) sin\left(\frac{r}{\Lambda}\right) r dr$$

$$\sim \frac{\Lambda}{r_p^2} exp\left(\frac{t}{\tau_{ins}}\right). \tag{10.6}$$

In the above approximation, it is assumed that the instability does not occur near the innermost radius, i.e, $r_p > r_{in}$ (cf. Abramowicz 1981), and $r_p \gg \Lambda$. From Eq. (10.6), the exponentially rising profiles of the superposed shots can be interpreted in terms of the intensity fluctuations due to the instabilities. It is also possible to take adequate values for r_p, Λ, and β so as to regard the obtained two constants, $\tau_{a\_}$ and $\tau_{b\_}$, of the superposed shots as the growing time constants of the thermal and viscous instabilities, $\tau_{thrm.ins}$ (Eq. 10.4) and $\tau_{visc.ins}$ (Eq. 10.5), respectively. However, it is very difficult to understand why the shots with different peak intensities have almost the same durations (§6.2.1). If peak intensities of two shots are different twice, Eq. 10.6 shows that the smaller shot occurs at a $\sqrt{2}$ times larger radius than the bigger one for the same Λ and β values, and the time constants of the smaller shot will be about 3 times larger than those of the bigger one (Eq. 10.4,10.5). It is also difficult to think that the disk is very locally unstable to understand this problem. If so, we must explain the reson why the instabilities arise so locally.

We have compared without specifying the cooling process of the disk. (If the disk is a two-temperature disk (Shapiro et al. 1976) or a coronal disk (Liang & Price 1977), the viscous instability is not expected (Piran 1978).) We thus come to the conclusion that in any disk situation, the problem about the constant time duration of the shots arise. Thus, it is unlikely that the shots are caused by these disk instabilities.

10.4.2 Magnetic Reconnection Models

Next, we will compare with magnetic field reconnection models. On the analogy of solar flares which exhibit intense X-ray fluctuations and non-thermal X-ray energy spectra, the shots in Cyg X-1 have been interpreted in terms of the magnetic reconnections above the disk surface, as well as the disk instabilities (§2.4.2). The solar flares are classified into a few types, and their time evolution are very complex. However, typical time duration of the magnetic reconnections in the case of Cyg X-1 is evaluated by two independent ways (Galeev, Rosner and Vaiana 1979; Pudritz and Fahlman 1982).

Galeev et al. (1979) estimated typical shot duration $\tau_{sol,rec}$ to be the reconnection time studied in the solar flares,

$$\tau_{sol,rec} \propto \frac{l}{v_A} \approx \frac{1}{\alpha^{1/3}\Omega} \tag{10.7}$$

where l is the typical length of the magnetic loop in the azimuthal direction and v_A is the Alfvén

speed at which magnetic disturbances propagate in the plasma and is of the order of the sound speed c_s. Here, we set $l \approx h/\alpha^{1/3}$ (Galeev et al. 1979) and $c_s \approx \Omega$ from vertical pressure balance of the accretion disk. Pudritz & Fahlman (1982) proposed that reconnection time $\tau_{exp,rec}$ and total energy flux of the flare $\int \delta F dt$ were estimated by model independent, scaled reconnection experiments, such as $\tau_{exp,rec} \propto l$ and $\int \delta F dt \propto b^2 l^3$ where b is the amplitude of the magnetic field fluctuation, and showed in the dynamo driven, gas pressure and electron scattering dominanted disk that

$$\tau_{exp,rec} \propto r, \tag{10.8}$$

$$\int \delta F dt \propto r^0. \tag{10.9}$$

These relation indicate that shots occurring at a larger radius have long durations and small peak intensities (or soft energy spectrum). Using Pudritz & Fahlman's parameters, Lochner et al. (1992) showed the distribution of shot durations was proportional to $\tau^{-\frac{3}{2}}$.

For X-ray time variability in AGN, taking account of the energy loss of electrons due to the inverse Compton scattering, de Vries & Kuijpers (1989) estimated flare time duration to be proportional to r^3.

None of these relations satisfies with the observed shot properties as discussed before. Spectral changes during the solar flares similar to those of the superposed shots have not been observed (Bai & Dennis 1985). Thus, the shots are unlikely to be the magnetic field reconnections themselves.

10.4.3 Aperiodic Mass Accretion Models

The above models describe local fluctuations in the accretion disk. Such local events presumably have time scales strongly depending on the radial distance, or more definitely on the local Kepler motion time scale ($= 1/\Omega$). This is against the observational fact that the time constants of the shots are independent of the peak intensity. Total energy per one biggest shot is $\sim 2 \times 10^{37}$ erg, most of which is radiated within 1 sec. This total energy is comparable to the total luminosity of the source and difficult to be stored in a local region. These facts strongly suggest that the shots do not arise from the local fluctuations but from some events occurring in a whole region where most of gravitational energy is released i.e., $r = 3 \sim 10\ r_s$.

One of such models is that clumps of accretion matter drift inward releasing the gravitational energy. This possibility has been suggested from time scale of the shots (Rothschild et al. 1974; Miyamoto et al. 1992), but hardly investigated theoretically because accretion matter

diffuses by share motion of the matter in the gas pressure-dominanted disk. In the radiation pressure-dominated disk, it may come true (Lightman and Eardley 1974; Lightman 1974a,b).

Leaving the problem why accretion matter clumps, an expected light curve from the matter indrifting to a black hole will be approximately estimated. First, one simple case will be shown. Assuming that the absolute radial velocity at a radius r, $|dr/dt|$, is proportional to the Kepler velocity at there (c.f., Lynden-Bell 1969; Pringle and Rees 1972),

$$\frac{dr}{dt} = -Cr^{-\frac{1}{2}}, \tag{10.10}$$

the position of the clumping matter at time t' (< 0) is obtained by integrating Eq. (10.10) from r ($t = t'$) to r_{in} ($t = 0$) where r_in is the innermost radius where these assumptions are valid. Thus,

$$r(t') = \left(r_{in}^{\frac{3}{2}} - \frac{3}{2} C t' \right)^{\frac{2}{3}}. \tag{10.11}$$

On the analogy of the Virial theorem, released emitted energy from the matter drifting from $r + \delta r$ to r is assumed to be equal to a decreasing rate of potential energy between the two radius. Using Eq. (10.11), an expected emitting rate from the matter with a mass m at time t, $F(t)$, can be expressed as

$$F(t) = \frac{GMm}{2r^2} \left(-\frac{dr}{dt} \right) = \frac{GMmC}{2} \frac{1}{\left(r_{in}^{\frac{3}{2}} - \frac{3}{2} Ct \right)^{\frac{5}{3}}}. \tag{10.12}$$

Thus, this is a kind of the fractal function introduced in §6.2.1. Comparing with Eq. (6.1), we find $\alpha_- = 5/3$ and $\tau_{f-} = 2r_{in}^{3/2}/3C$. Note that the increasing rate shown by this formula is independent of the peak intensity. If the radial velocity is assumed to be represented by a power of the radius, $|dr/dt| = Cr^{-\gamma}$, a more general formula can be obtained; $\alpha_- = 5/2(\gamma + 1)$.

Next, using *steady* state solutions of the α disk model (Shakura & Sunyaev 1973), the dependence of physical parameters on this formula will be investigated. Of course, the application of the steady state solutions for this non-steady problem may not be valid because some of equations used may not be hold in this situation. However, they will be available as approximate forms. Here we consider an intensity fluctuation $\delta F(t)$ due to a fluctuation of the accretion rate by $\delta \dot{m}$.

In the α disk model, using the mass conservation, the angular momentum conservation and the vertical pressure balance, the radial velocity is expressed as

$$\frac{dr}{dt} = -C\,\alpha \sqrt{\frac{GM}{r}} \left(\frac{h}{r} \right)^2 \left(1 - \sqrt{\frac{r_{in}}{r}} \right)^{-1}, \tag{10.13}$$

where C is a constant of the order of 1, and h is

$$h(r) = h_0 r^{\xi}. \tag{10.14}$$

The steady state solutions show that $\xi = 0$ in a radiation pressure-dominated region ($P_{rad} \gg P_{gas}$) and $\xi \simeq 1$ in a gas pressure-dominated region ($P_{gas} \gg P_{rad}$). A corresponding equation to Eq. (10.11) for $\xi \neq 7/4$ is

$$r(t') = (r_{in}^{\zeta} - \zeta\, C_1 \alpha \sqrt{GM} h_0^2 t')^{\frac{1}{\zeta}}, \quad \zeta \equiv \frac{7-4\xi}{2}. \tag{10.15}$$

(In the case of $\xi \neq 7/4$, $r(t')$ becomes an exponential function, which does not agree with the observational fact.) In the α disk model, the energy generation rate $E(r)$ per sec per gram per unit radial length (cm) is $E(r) = \frac{3}{2}\frac{GM}{r^2}\left(1 - \sqrt{\frac{r_{in}}{r}}\right)$. Here an additional assumption is imposed on the fluctuation of the accretion rate $\delta\dot{m}$, such as

$$\delta\dot{m} = \delta\dot{m}_0 r^{\eta}. \tag{10.16}$$

Under these assumptions, the intensity fluctuation $\delta F(t)$ can be written as follows.

$$\begin{aligned} \delta F(t) &= E(r)\,\delta\dot{m}\left(-\frac{dr}{dt}\right) \\ &= \frac{1}{2} C\alpha (GM)^{\frac{3}{2}} \delta\dot{m}_0 h_0^2 r^{\eta-\zeta-1} \\ &= \frac{A_-}{(\tau_{f_-} - t)^{\alpha_-}}, \end{aligned} \tag{10.17}$$

where

$$\begin{aligned} A_- &= \frac{3}{2}(C\alpha h_0^2)^{\frac{\eta-1}{\zeta}} (GM)^{\frac{\eta-1}{2\zeta}+1} \zeta^{\frac{\eta-1}{\zeta}-1} \delta\dot{m}_0 \\ &\simeq \begin{cases} 3^{\frac{\eta}{3}} \times 3 \times 10^{36}\ (\mathrm{erg/s}) \left\{ C\left(\frac{\alpha}{0.1}\right)\left(\frac{h_0}{0.1}\right)^2 \right\}^{\frac{2\eta-2}{3}} \left(\frac{M}{10M_\odot}\right)^{\frac{\eta+2}{3}} \left(\frac{\delta\dot{m}_0}{10^{17-7\eta}}\right) \\ \qquad\qquad ; \zeta = \frac{3}{2}\ (P_{gas} \gg P_{rad}) \\ 16^{\frac{\eta}{7}} \times 1.25 \times 10^{37}\ (\mathrm{erg/s}) \left\{ C\left(\frac{\alpha}{0.1}\right)\left(\frac{h_0}{10^6}\right)^2 \right\}^{\frac{2\eta-2}{7}} \left(\frac{M}{10M_\odot}\right)^{\frac{\eta+6}{7}} \left(\frac{\delta\dot{m}_0}{10^{17-7\eta}}\right) \\ \qquad\qquad ; \zeta = \frac{7}{2}(P_{rad} \gg P_{gas}), \end{cases} \end{aligned} \tag{10.18}$$

$$\begin{aligned} \tau_{f_-} &= \frac{r_{in}^{\zeta}}{\zeta C\alpha\sqrt{GM}h_0^2} \\ &\simeq \begin{cases} 0.5\ (\mathrm{s})\ \frac{1}{C}\left(\frac{r_{in}}{3r_s}\right)^{\frac{3}{2}} \left(\frac{\alpha}{0.1}\right)^{-1} \left(\frac{h_0}{0.1}\right)^{-2} \left(\frac{M}{10M_\odot}\right) & ; \zeta = \frac{3}{2}\ (P_{gas} \gg P_{rad}) \\ 0.15\ (\mathrm{s})\ \frac{1}{C}\left(\frac{r_{in}}{3r_s}\right)^{\frac{7}{2}} \left(\frac{\alpha}{0.1}\right)^{-1} \left(\frac{h_0}{10^6}\right)^{-2} \left(\frac{M}{10M_\odot}\right)^{3} & ; \zeta = \frac{7}{2}\ (P_{rad} \gg P_{gas}), \end{cases} \end{aligned} \tag{10.19}$$

and

$$\begin{aligned} \alpha_- &= 1 + \frac{1-\eta}{\zeta} \\ &\simeq \begin{cases} \dfrac{5-2\eta}{3} & ;\zeta = \dfrac{3}{2}\ (P_{gas} \gg P_{rad}) \\ \dfrac{9-2\eta}{7} & ;\zeta = \dfrac{7}{2}\ (P_{rad} \gg P_{gas}). \end{cases} \end{aligned} \tag{10.20}$$

These results are roughly consistent with the parameters obtained from the superposed shots though none of parameters can be uniquely determined. If the substructures, the bump and intensity decrease, are ignored, the obtained parameters are $\tau_{f_-} \simeq 0.025$ (1987) or 0.05 (1990), and $\alpha_- \simeq 0.7$ (1987, 1990) (Table 6.4 in §6.2.1). Thus, it is suggested from Eq. (10.19) that α and/or h_0 $(= h/r)$ are larger than the values shown, and it can be found from Eq. (10.20) that $\eta \simeq 1.45$ for $P_{gas} \gg P_{rad}$, and $\eta \simeq 2$ for $P_{rad} \gg P_{gas}$, both of which implies that the density fluctuation of the clumping matter decreases. However, one should not forget that these are approximate solutions.

Qualitatively, it can be found from these formulae that the smaller τ_{f_-} value in 1990 than that in 1987 implies that the disk in 1990 was thicker than that in 1987. This can be interpreted as follows. If the accretion rate becomes larger, the accretion flow becomes faster (and the disk thickness also becomes larger), resulting in a sharp profile of the shots. Certainly, average flux in 1990 was larger than that in 1987, but the profiles of the shots in 1987 were stable in spite of the increase of observed flux by ~ 30 % (§6.2.1). Thus, further observational and theoretical investigations into this problem are needed.

This model explains not only the rise profile of the shots independent of the peak intensity, but also the observed rapid spectral change at the peak intensity. The rapid spectral change and following intensity decrease can be interpreted as the disappearance of the emitting matter. If the drifting matter has an extension of $\sim 10^6$ $(\sim h)$ cm in the radial direction, it takes $\sim$ 10 ms for the matter to pass though the innermost radius prevented that the radial velocity at the radius is one hundredth of the Kepler velocity. If a hard surface just like a neutron star is present within the innermost radius, enhanced emission due to a shock wave is expected after the rapid spectral change because the accreting matter has a large amount of kinematic energy, $GM\dot{m}/2r_{in}^2 = mc^2/12$ (in the non-rotating black hole). Thus, *this model requires that the central object is a black hole.*

The soft energy spectrum of the shots before the peak intensity shows the decrease of electron temperature and/or scattering optical depth (§9.1.2). At higher intensity, the electron temperature will be decreased by radiating or scattering photons (Doi 1980). Taking account

of an effect of pair production in AGNs spectra, Lightman & Zdziarski (1987) also came to the same conclusion (Fig. 6 of Lightman & Zdziarski 1987). (The observed rapid spectral hardening at peak intensity can not be explained by their models because these authors considered much more simple cases.) However, it is difficult to explain the stability of the soft spectrum. More consideration is necessary. In the same sense, the harder spectrum after peak intensity suggests that those photons are not emitted so locally. (The emission does not exhaust there local energy.)

Recently, Mineshige et al. (1994a,b) considered numerous small reservoirs to store accreting matter (in self-organized critical (SOC) model), and showed that avalanches of the matter accumulated in some reservoirs occur *almost* randomly. These avalanches will be observed as shots. In their model, they speculated that the magnetic field prevented the matter from drifting inward, and that once a reconnection occurred, the angular momentum was transferred outward and matter started drifting. In accumulating matter in reservoirs, emission from the disk will be suppressed.

This scenario not only suggests the possibility of the density fluctuation, but also explains the observed suppression of the shot appearance (§6.1.1) and the resultant intensity decrease before the shots (§6.2.1). Furthermore, the small bump near the beginning of the shots may be due to the magnetic reconnection though it does not always appear (§6.2.1). Total energies of the bumps in 1987 and 1990 are $\sim 10^{36}$ and $\sim 10^{35}$ erg, respectively, which are consistent with expected energy released by a magnetic flare (Galeev et al. 1979). In addition, after a big shot event, it takes more time to fill accretion matter in the inner portion of the disk (Mineshige et al. 1994b). This also explains intensity decrease after the shots. It was also confirmed that this phenomenon was consistent with the simulation of the SOC model (Negoro et al. 1995).

In this aperiodic mass accretion model, one big problem remains; the excess emission after peak intensity. There are three possibilities to explain this emission.

(a) Emission by remaining, diffused clumping matter in the inner portion of the accretion disk.

(b) Emission by gravitational energy near the innermost radius transferred outward with the angular momentum.

(c) Unknown emission at region within the radius r_{in}.

The observed and model α_- values implies that significant clumping matter remains at the disk, which supports the possibility (a). Furthermore, both the time scales for accretion matter to drift by R (which is known as the radial drift time scale, Lightman 1974a) and for a disk annulus to spread over R (the diffusion time scale, Pringle 1981) are represented by

$\sim 1/\alpha\omega\, rR/h^2$. This may explain the observed symmetry profiles of the shots.

The possibility (b) comes from the fact that accretion matter must lose its angular momentum to drift inward. In transferring the angular momentum outward, the mechanical energy is also transported outward by the viscous stress (Novikov & Thorne 1973, p. 416; Shakura & Sunyaev 1973). The energy conservation at a local part in a non stational disk can be approximately described by the equation (Shakura & Sunyaev 1976)

$$\frac{\partial}{\partial t}\Sigma r\left(\frac{\Omega^2 r^2}{2}-\frac{GM}{r}\right)=-\frac{\partial}{\partial r}\left(\Sigma v_r r\left(\frac{\Omega^2 r^2}{2}-\frac{GM}{2}\right)\right)-\frac{\partial}{\partial r}\left(W_{r\phi}\Omega r^2\right)+W_{r\phi}r^2\frac{\partial\Omega}{\partial r}, \quad (10.21)$$

where Σ $(=2\rho h)$ is the surface density, v_r $(=dr/dt)$ is the radial velocity, and $W_{r\phi}$ is the viscous stress. The second and third terms of the right-hand side of this quation present the viscous torque and the energy dissipation rate, respectively. Using the continuity equation, $\partial\Omega/\partial t = 1/2\pi r\,\partial\dot{m}/\partial r$, we have the energy flux radiated from surface of the disk, Q^+,

$$Q^+ = -\frac{1}{2}W_{r\phi}r\frac{\partial\Omega}{\partial r}=\frac{\dot{m}\Omega^2}{8\pi}-\frac{1}{2r}\frac{\partial}{\partial r}(W_{r\phi}\Omega r^2). \quad (10.22)$$

Shakura & Sunyaev (1976) pointed out "*During radial motion half the liberated potential energy goes into increasing the kinetic energy, and the other half (corresponding the first term on the right-hand side of Eq. (10.22)) should go into heat and mechanical energy. As well as transferring angular momentum, viscous stress transfer mechanical energy. This process explains the second term on the right of Eq. (10.22)*". This explains why the energy flux Q^+ in the α disk model is three time larger than that expected from the Virial theory at large $r \gg r_{in}$. It should be noted that these arguments are free from the origin of the viscosity.

In the steady state, the viscous torque is represented by $W_{r\phi} = \dot{m}\Omega/2\pi(1-\sqrt{\frac{r_{in}}{r}})$. In this case, the second term becomes zero at the radius $r = 9r_{in}/4$, and the energy of $8GM\dot{m}/54r_{in}$, which corresponds to 8/27 of the total emitted energy in the accretion, is transferred from the inner radius to the outer radius. Even if the energy is really transferred in this non-stationary case, the amount of the transferred energy can not explain the total emission after peak intensity comparable to that before peak intensity.

It is easy to imagine the possibility (c) if the central object is not a black hole. Liang & Dermer (1988) and Liang (1990) proposed an accretion disk model that a γ-ray emitting region existed at an inner part ($r_s \lesssim r \lesssim 10r_s$) of a X-ray emitting region. Using their model, the model parameter r_{in} in Eq. (10.11) and Eq. (10.15) may be expressed as $r_{in} \simeq 10r_s$ or $20r_s$. However, their model does not present a general state of the disk (c.f., Ling et al. 1987), and the temperature of the γ-ray emission region is too high ($\sim$ 400 keV) to explain the observed hard power law component.

A hint of the problem, the excess component after peak intensity, is the spectrum at that time. The spectrum shows very similar to the time averaged spectrum. Taking account of the fact that the shot fraction is less than $10 \sim 20$ % (§8.1), this suggests that the excess shot component after peak intensity is radiated at the region where most of X-rays are emitted. The hard spectrum of the shots after the peak intensity also suggests that those X-rays are not local emission. Thus, the possibilities (a) and (b) are likely, and both of which can not be roled out. Furthermore, the observed time averaged spectrum with a small reflection component prefers a two-temperature type disk (Shapiro et al. 1976) to a coronal type disk (Liang & Price 1977) (§10.3.3). In this scenario, soft photons in the two-temperature region are provided by the shots as discussed in §10.3.2. This possibility may solve the fundamental problem, the origin of seed soft photons, in the two-temperature disk model (Liang & Nolan 1984). Note that there is no necessity that the X-ray emitting region must be the two temperature state by Shapiro et al. (1976).

In conclusion, the shots are caused by density fluctuations of accreting matter trapped by magnetic force near the outside, where a cool disk still remains, of the two temperature region. The clumping matter drifts inward diffusing and releasing the gravitational energy as a shot. After most of the clumping matter passes through the innermost radius (disappears to the black hole), hard X-rays are emitted from the two temperature region excited by the shots.

Chapter 11

Summary

We analyzed the data of Cyg X-1 obtained on 5–6 Aug 1987 and 9-11 May 1990, with the LAC on board *Ginga*. A new analysis method, the superposition of X-ray shots, revealed the following results.

(1) Both profiles of the superposed shots in 1987 and 1990 are almost symmetric rise and decay, each of which is roughly represented by a sum of two exponentials with time constants of about 0.1 and 1 s, and the rise profiles are also roughly described by a function proportional to $1/(\tau - t)^{\alpha}$ where t (< 0) is the relative time, τ ($\sim 0.02 - 0.05$ s) and α (~ 0.7) are constants. Ratios of total counts of the excess shot component in the rise phase to those in the decay phase are 0.96 ± 0.03 in 1987 and 0.92 ± 0.03 in 1990.

(2) In describing the profiles with the sum of two exponentials, they represent a sharp peak component and a wing component. A large difference between the profiles of the superposed shots in 1987 and 1990 is magnitude of the wing components. Count ratios of the peak components to the wing components are 0.30 ± 0.02 in 1987 and 0.41 ± 0.02 in 1990, and the time constants in 1987 are ~ 50 % larger than those in 1990. Both the rising profiles are steady on time scales of at least a few hours. On the other hand, the decaying profile in 1987 varies on time scales of a few hours or less, and that in 1990 slightly changes on a time scale of a day.

(3) Both the superposed shots in 1987 and 1990 have sub-structures unable to be represented by the sum of two exponentials. Substructures in the rise phase are a small bump before 3.7 s (1987) or 1.8 s (1990) from the peak and a slight decrease in intensity before the bump. Note that both the bumps in 1987 and 1990 appear near the beginning of the shots. The bump in 1987 was obviously observed for only a few hours, while that in 1990 was through 3 days. As the decaying profiles vary in time, obvious sub-structures can not be specified.

(4) The shots with larger peak intensities tend to have asymmetric profile; gradual rise and

rapid decay. The rise time constants of the exponentials are, however, independent of the peak intensity, while the large decay time constant of the shots with larger peak intensities is larger.

(5) Hardness ratios of these excess shot components before the peak intensity are steady and softer than the time averaged ratios of all the X-rays. The ratios suddenly harden at the peak intensity. In some energy bands, the ratios continue hardening with the intensity decrease for 0.2 – 0.3 s. The spectral hardening at the peak intensity may occur on time scales of milliseconds or less.

(6) Comparison of the above temporal and spectral properties of the superposed shots with observed NPSDs and time lags shows good consistency below ~ 1 Hz. Effects of the substructures in 1990 and the soft energy spectrum of the shots are also confirmed in the NPSDs. Weak energy dependence of the time constants of the shots implies that the time lags indicate not only the spectral hardening with the intensity decrease but also the rapid spectral hardening at the peak intensity.

(7) An unknown high frequency component which can not be explained by the superposed shots exists in the power spectrum at frequencies above 1 Hz. The NPSDs indicate that the component has a hard spectrum. The soft energy spectrum of the shots also implies the existence of a hard spectrum component. These hard components are expected to exhibit small and very short (< 0.1 sec) time variability.

(8) The shots do not occur at random, their appearance is suppressed for several seconds before and/or after one big events, which strongly suggests the existence of numerous reservoirs of accretion matter. It is also found that the peak intensity of the shots is exponentially distributed. From the shot profile and the peak-intensity distribution, the shot fraction, the rate of the shot component to the total components, is found to be 10–20 %, which is smaller than those in previous shot noise models.

(9) The energy spectrum of the shots can be represented by a Comptonized blackbody plus power law model. Each of the components dominates the spectrum before and after the peak intensity, respectively. The soft energy spectrum of the shots explains an observed soft excess component at energies below a few keV. The multi-continuum energy spectrum including an unknown hard spectrum also reproduces an edge-like structure at energies 7–20 keV and a hard bump at higher energies. As a result, an effect of a disk reflection is less important than previously thought.

(10) These obtained properties of the X-rays from Cygnus X-1 constrain disk geometry, emission regions and their mechanism. The profile of the shots independent of peak intensity

rules out previous shot occurrence models by disk instabilities and magnetic field reconnections, and strongly suggests that the shots arise from density fluctuations of accretion matter drifting into a black hole. Together with this conclusion, the small effect of the reflection component prefers a two-temperature type disk to a coronal type disk. The shots will provide soft photons and gravitational energy with the two temperature region where most of observed X-rays are emitted.

Acknowledgement

First of all, I am deeply grateful to Prof. Sigenori Miyamoto for his valuable discussions during my life in graduate school and comments on this work. He showed me the importance of the timing analysis, and gave me ideas to analyze the data. I am also grateful to Dr. H. Tsunemi for his advices for the study of a supernova remnant, Cas A, and other ASCA projects. I wish to thank to Dr. S. Kitamoto and Dr. K. Hayashida who supported my study many times, and discussed a variety of matters. Especially, Dr. Kitamoto taught me basic concepts of timing analyses, and Dr. Hayashida supported my work-station. I must also thank Mr. K. Kawashima, Mr. T. Suzuki, Mr. Y. Ohno, Mr. W. Egoshi, Mr. N. Miura and all of my laboratory members, who helped me in preparing this thesis.

I'd like to express my special thanks to Dr. S. Mineshige at Kyoto university. He discussed problems between observational and theoretical results of the accretion disks with me so many times.

I appreciate all the member of *Ginga* team, who gave me a chance to analyze very excellent data, also those who operated the observations. Finally, I'd like to thank my family, old friends of mines and Ms. Chikako Maruyama for encouraging and supporting me in various ways.

Appendix A

Increased Counts of Peak Bins of Superposed Shots due to the Count Fluctuations

A.1 Single Bin Case

We estimate systematically increased counts of peak bins of superposed shots due to the count fluctuations. Imagine a number of shots, of which peak counts is distributed obeying the Poisson statistics, and have an average count n. Of these shots, the shots with peak count P ($m \leq P < l$) are selected. An expected average excess count of these shots from n, $f(n,m,l)$, is

$$f(n,m,l) = \frac{\sum_{P=m}^{l-1} P\frac{n^P e^{-n}}{P!}}{\sum_{P=m}^{l-1} \frac{n^P e^{-n}}{P!}} - n. \tag{A.1}$$

For large n $\gg 1$, Eq. (A.1) can be replaced by

$$f(n,m,l) = \frac{\frac{1}{\sqrt{2\pi}\sigma}\int_m^{l-1} Pe^{\frac{(P-n)^2}{2\sigma^2}}dP}{\frac{1}{\sqrt{2\pi}\sigma}\int_m^{l-1} e^{\frac{(P-n)^2}{2\sigma^2}}dP} - n. \tag{A.2}$$

where $\sigma = \sqrt{n}$. If $t_m = (m-n)/\sqrt{2}\sigma$, $t_l = (l-1-n)/\sqrt{2}\sigma$, then

$$\begin{aligned} f(n,m,l) &= \sqrt{2}\sigma\frac{\int_{t_m}^{t_l} te^{t^2}dt}{\int_{t_m}^{t_l} e^{t^2}dt} \\ &= \frac{\sigma}{\sqrt{2\pi}}\frac{e^{-t_m^2} - e^{-t_l^2}}{P_{reg}(n,m,l)}, \end{aligned} \tag{A.3}$$

where $P_{reg}(n,m,l)$ is a probability that peak counts of those shots are in the region $(m \leq P < l)$,

$$P_{reg}(n,m,l) = \begin{cases} |\Gamma(1/2,t_l^2) - \Gamma(1/2,t_m^2)|/2 & t_m \times t_l \geq 0 \\ \{2 - \Gamma(1/2,t_l^2) - \Gamma(1/2,t_m^2)\}/2 & t_m \times t_l < 0. \end{cases} \tag{A.4}$$

In this formula, $\Gamma(a,x)$ $(a > 0)$ is the incomplete gamma function defined by

$$\Gamma(a,x) \equiv \frac{1}{\Gamma(a)} \int_x^\infty e^{-t} t^{a-1} dt. \tag{A.5}$$

Finally, a rate of these shots with the average peak count n to all the shots must be known. If the peak intensities of the shots is exponentially distributed, the rate $P_{dis}(n)$ is

$$P_{dis}(n) = \frac{e^{-\frac{n}{p_{decay}}}}{p_{decay}}, \tag{A.6}$$

where p_{decay} is a decay constant of the peak intensity distribution. Thus, an expected excess count of a peak bin of a superposed shot, $C(m,l)$, is

$$\begin{aligned} C(m,l) &= \frac{\sum_{n=0}^{\infty} f(n,m,l)\, P_{reg}(n,m,l)\, P_{dis}(n)}{\sum_{n=0}^{\infty} P_{reg}(n,m,l)\, P_{dis}(n)} \\ &= \frac{\sigma}{\sqrt{2\pi}} \frac{\sum_{n=0}^{\infty} (e^{-\frac{(m-n)^2}{2n}} - e^{-\frac{(l-n)^2}{2n}})\, e^{-\frac{n}{p_{decay}}}}{\sum_{n=0}^{\infty} P_{reg}(n,m,l)\, e^{-\frac{n}{p_{decay}}}}. \end{aligned} \tag{A.7}$$

Using this formula, we can instantaneously obtain an excess count of a peak bin of a superposed shot. In this model, however, an effect of neighboring bins of the peak bin is not taken into account. Thus, this model can be adapted to the only case that counts of peak bins of shots are always much larger than those of the neighboring bins.

References

Abramowicz, M. A. 1981, Nature, 294, 235
Abramowicz, M. A., Czerny, B., Lasota, J. P., & Szuszkiewicz, E. 1988 ApJ, 322, 646
Abramowicz, M. A., Bao, G., Lanza, A., & Zhang, X. H. 1989, in Proc. 23rd ESLAB Symposium (ESA SP-296), ed. J. Hunt & B. Battrick (Noordwijk: ESA), Vol. 2, 1069
Abramowicz, M. A., Lanza, A., Spiegel, E. A., & Szuszkiewicz, E. 1992, Nature, 356, 41
Avni, Y., & Bahcall, J. N. 1975, ApJ, 197, 675
Awaki, H., Koyama, K., Kunieda, H., & Tawara, Y. 1990, Nature, 346, 544
Bai, T., & Dennis, B. 1985, ApJ, 292, 699
Barr, P., & van der Woerd, H. 1991, ApJ, 352, L41
Belloni, T., & Hasinger, G., 1990a, A&A, 227, L33
1990b, A&A, 230, 103
Balucińska, M., & Chlebowski., T. 1988, Adv. Space Res., 8, 2, 197
Balucińska, M., & Hasinger, G. 1991, A&A, 241, 439
Bisnovatyi-Kogan, G. S., & Blinnikov, S. I. 1977, A&A, 59, 111
Bolton, C. T. 1975, ApJ, 200, 269
Bregman, J., Butler, D., Kemper, E., Koski, A., Kraft, R.P., Stone, R. P. S. ApJ, 185, L117
Canizares, C. R., & Oda, M. 1977, ApJ, 214, L119
Casares, J., Charles, P. A., & Naylor, T. 1992, Nature, 355, 13
Cowly, A. P., 1983, ApJ, 272, 118
Czerny, B., Czerny, M., & Grindlay, J. 1986, ApJ, 311, 241
de Vries, M & Kuipers, J. 1989, in Proc. 23rd ESLAB Symposium (ESA SP-296), ed. J. Hunt & B. Battrick (Noordwijk: ESA), Vol. 2, 1069
Doi, K. 1980, Nature, 287, 210
Done, C., Mulchaey, J. S., Mushotzky, R. F., & Arnaud, K., A. 1992, ApJ, 395, 275
Dotani, T. 1988, Doctoral Thesis, University of Tokyo (ISAS RN, 418)
Eardley, D. M., & Lightman, A. P. 1975, ApJ, 200, 187
Eardley, D. M., Lightman, A. P., & Shapiro, S. L. 1975, ApJ, 199, L153
Ebisawa, K. 1991, Doctoral Thesis, University of Tokyo
Egoshi, W. 1995, Master Thesis, Osaka University
Galeev, A. A., Rosner, R., & Vaiana, G. S. 1979, ApJ, 229, 318
George, I., & Fabian, A. 1991, MNRAS, 249, 352
Green, A. R., McHardy., I. M., & Lehto, H. J. 1993, M.N.R.A.S., 265, 664
Guilbert, P., & Rees, M. J. 1988, M.N.R.A.S., 233, 475
Halpern, J. 1985, ApJ, 290, 130
Harmes, R. J. et al. 1994, ApJ, 435, L35
Harmon, B. A. et al. 1992, proceedings.
Hasinger, G., & van der Klis, M. 1989, A&A, 225, 79
Hayashida, K. 1989, Doctoral Thesis, University of Tokyo.
Hawking, S. W. 1973, in Black Holes, ed. C. DeWitt & B. DeWitt (New York: Gordon & Breach), p.1
Hoshi, R., & Inoue, H. 1988, PASJ, 40, 421
Hutching, J. B., Crampton, D., & Cowley, A. P. 1983, ApJ, 275, L43

Ilovaisky, S. A., Chevalier, C., Motch, C., Chiappetti, L. 1986, A&A, 164, 67
Inoue, H., & Hoshi, R. 1987, ApJ, 322, 320
Inoue, H. 1989, in Proc. 23rd ESLAB Symposium (ESA SP-296), ed. J. Hunt & B. Battrick (Noordwijk: ESA), Vol. 2, 783
Inoue, H. 1992, in Frontiers of X-ray Astronomy, ed. Y. Tanaka & K. Koyama (Tokyo: Universal Academy Press), 291
Inoue, H. 1993 in Accretion Disks in Compact Stellar Systems, ed. J. C. Wheeler (New Jersey: World Scientific), 303
in't Zand, J., Pan, H., Bleeker, J., Skinner, G., Gilfanov, M., and Sunyaev, R. 1992, A&A, 266, 283
Kitamoto, S., Miyamoto, S., Tanaka, S., Ohashi, T., Kondo, T., Tawara, Y., Nakagawa, M. 1984, PASJ, 36, 731
Kitamoto, S., et al. 1984, PASJ, 36, 799
Kitamoto, S., Miyamoto, S., & Yamamoto, T. 1989a, Publs. Astr. Soc. Japan, 41, 81
Kitamoto, S., Tsunemi, H., Miyamoto, S., Yamashita, K., Mizobuchi, S., Nakagawa, M., Dotani, T., & Makino, F. 1989b, Nature, 342, 518
Kitamoto, S., & Miyamoto, S. 1989 in Timing Neutron Stars, ed. H. Ogelman & E. P. J. van den Heuvel, NATO ASI Series, C, 262, 27
Kitamoto, S., Tsunemi, H., Pedersen, H., Ilovaisky, S. A., & van der Klis, M. 1990, ApJ, 361, 590
Kitamoto, S., Tsunemi, H., Miyamoto, S., & Hayashida, K. 1992, ApJ, 394, 609
Kitamoto, S. 1993, in Proc. Fourth International Conference on Plasma Physics and Controlled Nuclear Fusion, Toki, Japan, p.297
Kruper, J. S., Urry, C. M., & Canizares, C. R. 1990, ApJ. Sup, 74, 347
Kusunose, M., & Mineshige, S. 1992, ApJ, 392, 653
Lawrence, A., Watson, M., Pounds, K., & Elvis, M. 1985, M.N.R.A.S., 217, 685
— 1987, Nature, 325, 694
Lawrence, A., & Paradakis, I. 1993, ApJ, 414, L85
Lehto, H. J. 1989, in Proc. 23rd ESLAB Symposium (ESA SP-296), ed. J. Hunt & B. Battrick (Noordwijk: ESA), Vol. 1, 499
Leibwitz, E. M. 1984, M.N.R.A.S., 210, 279
Lewin, W. H. G., van Paradijs, J., van der Klis, M. 1988, Space Sci. Rev., 46, 273
Liang, E. P., & Price, R. H. 1977, ApJ, 218, 247
Liang, E. P., & Nolan, P. L. 1984, Space Scien. Rev., 38, 353
Liang, E. P., & Dermer, C. D. 1988, ApJ, 325, L39
Liang, E. P. 1990, A&A, 227, 447
Lightman, A. P. 1974a, ApJ, 194, 419
— 1974b, ApJ, 194, 429
Lightman, A. P., & Eardley, D. M. 1974, ApJ, 187, L1
Lightman, A. P., & White, T. R. 1988, ApJ, 335, 57
Lightman, A. P., & Zdziaksy, A. A. 1987, ApJ, 319, 643
Ling, J. C., Mahoney, W. A., Wheaton, W. A., & Jacobson, A. S. 1987, ApJ, 321, L117
Lochner, J. C., Swank, J. H., & Szymkowiak, A. E. 1991, ApJ, 375, 295
Lynden-Bell, D. 1969, Nature, 223, 690
Maejima, Y., Makishima, K., Matsuoka, M., Ogawara, Y., Oda, M., Tawara, Y., & Doi, K. 1984, ApJ, 285, 712
Makino, F., & Astro-C team, 1987, Astrophys. Letters Commun., 25, 223
Makino, F., & Ginga Team, 1988, IAU Circl, No4571
Makishima, K., Maejima, Y., Mitsuda, K., Bradt, H. V., Remillard, R. A., Tuohy, I. R., Hoshi, R., & Nakagawa, M. 1986, ApJ, 308, 635
Makishima, K. 1988, in Physics of Neutron Stars and Black Holes, ed. Y. Tanaka (Tokyo: Universal Academy Press), 175
Marchall, F. E., Mushotzky, R. F., Petre, R., Serlemitsos, P. J. 1993, ApJ, 419, 301
Margon, B., Bowyer, S., Stone, R. P. S. 1973, ApJ, 185, L113

Mason, K., Hawkins, F., Sanford, P., Murdin, P., & Savage, A. 1974, ApJ, 192, L65
Matt, G., Costa, E., Perola, G. C., & Piro, L. 1989, in Proc. 23rd ESLAB Symposium (ESA SP-296), ed. J. Hunt & B. Battrick (Noordwijk: ESA), Vol. 2, 991
Matt, G., Perola, G. & Piro, L. 1991, A&A, 247, 25
Matsuoka, M., Piro, L., Yamauchi, M., & Murakami, Y. 1990, ApJ, 361, 440
McClintock, J. E., & Remilard, R. A. 1986, ApJ, 308, 110
McHardy, I., & Crerny, B. 1987, Nature, 325, 696
McHardy, I, in Proc. 23rd ESLAB Symposium (ESA SP-296), ed. J. Hunt & B. Battrick (Noordwijk: ESA), Vol. 2, 1111
Meekins, J. F., Wood, K. S., Hedler, R. L., Byram, E. T., Yentis, D. J., Chubb, T. A., & Friedman, H. 1984, ApJ, 278, 288
Mereghetti, S. 1993, A&A Supl., 97, 249
Mineshige, S., & Kusunose, M. 1993 in Accretion Disks in Compact Stellar Systems, ed. J. C. Wheeler (New Jersey: World Scientific), 370
Mineshige, S., Ouchi, N. B., & Nishimori, H. 1994a, Publs. Astr. Soc. Japan, 46, 97
Mineshige, S, Takeuchi, M., Nishimori, H. 1994b, ApJ, 435, L125
Mitsuda, K., Inoue, H., Koyama, K., Makishima, K., Matsuoka, M., Ogawara, Y., Shibazaki, N., Suzuki, K., Tanaka, Y., Hirano, T. 1984, PASJ, 36, 741
Mitsuda, K., & Dotani, T. 1989, Publs. Astr. Soc. Japan, 41, 557
Mitsuda, K. 1992, in Proc. Ginga memorial symposium, ed. F. Makino & F. Nagase ISAS symposium on Astrophysics 1992, p.11
Miyamoto, S., Kitamoto, S., Mitsuda, K., & Dotani, T. 1988, Nature, 336, 450
Miyamoto, S., & Kitamoto, S. 1989, Nature, 342, 773
Miyamoto, S., Kimura, K., Kitamoto, S., Dotani, T., & Ebisawa, K. 1991, ApJ, 383, 784
Miyamoto, S., Kitamoto, S., Iga, S., Negoro, H., & Terada, K. 1992, ApJ, 391, L21
Miyamoto, S., Iga, S., Kitamoto, S., & Kamado, Y. 1993, ApJ, 403, L39
Miyamoto, S., Kitamoto, S., Iga, S., Hayashida, K., & Terada, K. 1994, ApJ,
Miyamoto, S., Kitamoto, S., Hayashida, K., & Egoshi, W. 1995, ApJ, in printing
Miyoshi, M., Moran, J., Hernstein, J., Greenhill, L., Nakai, N., Diamond, P., & Iuoue, M. 1995, Nature, 373, 127
Morini, M., Lipani, N. A., & Molteni, D. 1987, ApJ, 317, 145
Murakami, T., Fujii, M., Hayashida, K., Itoh, M., Nishimura, J., Yamaguchi, T., Yoshida, A., Conner, J., Evans, W., Fenimore, E., Klevesadel, R., Spencer, K., Murakami, H., Kawai, N., Kondo, I., Katoh, M. 1989, PASJ, 41, 405
Nandra, K., & Pounds, K. A. 1994, M.N.R.A.S., 268, 405
Negoro, H., Miyamoto, S., & Kitamoto, S. 1994, ApJ, 423, L127
Negoro, H., Kitamoto, S., Takeuchi, M., & Mineshige, S. 1995, ApJ, Letters (in submitted)
Nishimura, J., Mitsuda, K., & Itoh, M. 1986, PASJ, 38, 819
Nolan, P. L., Gruber, D. E., Matteson, J. L., Peterson, L. E., Rothschild, R. E., Doty, J. P., Levine, A. M., Lewin, W. H. G., & Primini, F. A. 1981, ApJ, 246, 494
Novikov, I. D., & Thorne, K., S. 1973, in Black Holes, ed. C. DeWitt & B. DeWitt (New York: Gordon & Breach), p. 343
Nowak, M. A. 1994, ApJ, 422, 688
Oda, M., Gorenstein, P., Gursky, H., Kellogg, E., Schreier, E., Tananbaum, H., and Giacconi, R. 1971, ApJ, 166, L1
Oda, M., Doi, K., Ogawara, Y., Takagishi, K., & Wada, M. 1976, Ap & Space Scien., 42, 223
Oda, M. 1977, Space Scien. Rev., 20, 757
Ogawara, Y., Doi, K., Matsuoka, M., Miyamoto, S., & Oda, M. 1977, Nature, 270, 154
Pacholczyk, A. G. & Stoeger, S.J., W. R. 1994, ApJ, 434, 435
Paczynski, B., & Wiita, P. 1980, A&A, 88, 23
Page, C. G., 1985, Space Scien. Rev., 40, 387
Piran, T. 1978, ApJ, 221, 652

Pounds, K. A., & Mchardy, I. M. 1988, in Physics of Neutron Stars and Black Holes, ed. Y. Tanaka (Tokyo: Universal Academy Press), 285
Pounds, K. A., Nandra, K., Stewart, G. C., George., I. M., & Fabian, A. C. 1990, Nature, 344, 132
Press, W., H. 1978, Comments Ap., 7, 4, 103
Pringle, J. E., & Rees, M. J. 1972, Astro. Ap., 21, 1
Pringle, J. E., Rees, M. J., Pacholczyk, A. G. 1973, A&A, 29, 179
Pringle, J. E. 1981, Ann. Rev. Astro. Ap., 19, 137
Priedhorsky, W., Garmire, G. P., Rothschild, R., Boldt, E., Serlemitsos, P., & Holt, S. 1979, ApJ, 233, 350
Pudritz, R. E. 1981a, M.N.R.A.S., 195, 881
— 1981b, M.N.R.A.S., 195, 897
Pudritz, R. E. & Fahlman, G. G. 1982, MNRAS, 198, 689
Remillard, R. A., McClintock, J. E., & Bailyn, C. D. 1992, ApJ, 399, L145
Rothschild, R. E., Boldt, E. A., Holt, S. S., & Serlemitsos, P. J. 1974, ApJ, 189, L13
— 1977, ApJ, 213, 818
Rybicki, G. B., & Lightman, A. P. 1979, in Radiative Processes in Astrophysics, (New York: A Wiley-Interscience Pub.)
Salotti, L., Ballet, J., Cordier, B., Lambert, A., Bonazzola, S., Mereghetti, S., Mandrou, P., Roques, J. P., Sunyaev, R., Gilfanov, M., Churazov, E., Chulkov, I., Kuznetsov, I., Dyachkov, A., Khavenson, N., Novikov, B. 1992, A&A, 253, 145
Samimi, J., Share, G. H., Wood, K., Yentis, D., Meekins, J., Evans, W., Shulman, S., Byram, E., Chubb, T., & Friedman, H. 1979, Nature, 278, 434
Shakura, N. I., & Sunyaev, R. A. 1973, Astr. Ap., 24, 337
Shakura, N. I., & Sunyaev, R. A. 1976, MNRAS, 175, 613
Shapiro, S. L., Lightman, A. P., & Eardley, D. M. 1976, ApJ, 204, 187
Shapiro, S. L., & Teukolsky, S. A. 1983, in Black Holes, White Dwarfs, and Neutron Stars, (New York: A Wiley-Interscience Publication)
Shibazaki, N., & Hoshi, R. 1975, Prog. Theor. Phys., 54, 706
Shibata, K., Tajima, T., & Matsumoto, R. 1990, ApJ, 350, 295
Singh, K. P., Westergaard, N. J., Schnopper, H. W., Awaki, H., & Tawara, Y. 1990, ApJ, 363, 131
Stoeger, W. R., S.J. 1980, ApJ, 235, 216
Sunyaev, R. A., & Trumper, J. 1979, Nature, 279, 506
Sunyaev, R. A., & Titarchuk, L. G. 1980, A&A, 86, 121
Sunyaev, R. A., Churazov, E., Gilfanov, M., Pavlinsky, M., Grevenev, S., Babalyan, B., Dekohanv, I., Khavenson, M., Bouchet, L., Mandrou, P., Roques, J.P., Vedrenne, G., Cordier, B., Goldwurm, A., Lebrum, F., Paul, J. 1990, ApJ, 383, L49
Sunyaev, R. A., et al. 1992, ApJ, 389, L75
Sutherland, P. G., Weisskopf, M. C., & Kahn, S. M. 1978, ApJ, 219, 1029
Takayasu, H. 1986, in Fractal, (Tokyo: Asakura-shorten) in Japanese
Tanaka, Y. 1989, in Proc. 23rd ESLAB Symposium (ESA SP-296), ed. J. Hunt & B. Battrick (Noordwijk: ESA), Vol. 1, 3
Tanaka, Y. 1992, in Proc. Ginga memorial symposium, ed. F. Makino & F. Nagase ISAS symposium on Astrophysics 1992, p.19
Tashiro, M. 1991, Doctoral Thesis, University of Tokyo.
Terada, K. 1994, Doctoral Thesis, Osaka University.
Terrell, N. J., & Olsen, K. H. 1970, ApJ, 161, 399
Terrell, N. J. 1972, ApJ, 174, L35
Thorne, K. S., & Price, R. H. 1975, ApJ, 195, L101
Tout, C. A., & Pringle, J. E. 1992, M.N.R.A.S., 259, 604
Tsunemi, H., Kitamoto, S., Manabe, M., Miyamoto, S., & Yamashita, K. 1989a, PASJ, 41, 391
Tsunemi, H., Kitamoto, S., Okamura, S., & Roussel-Dupre, D. 1989b, ApJ, 337, L81
Turner, T. J., & Pounds, K. A. 1988, M.N.R.A.S., 232, 463

Turner, T. J., & Pounds, K. A. 1989, M.N.R.A.S., 240, 833
Turner, M. J. L. et al. 1989, Publs. Astr. Soc. Japan, 41, 345
Ueda, Y., Ebisawa, K., & Done, C. 1994, Publs. Astr. Soc. Japan, 46, 107
van der Klis, M., Hasinger, G., Stella, L., Langmeier, A., van Paradijs, J., & Lewin, W. H. G., 1987, ApJ, 319, L13
van der Klis, M., 1989 in Timing Neutron Stars, ed. H. Ogelman & E. P. J. van den Heuvel, NATO ASI Series, C, 262, 27
van der Klis, M., 1994, A&A, 283, 469
Volwerk, M., van Oss, R. F., & Kuijpers, J. 1993, A&A, 270, 265
Weisskopf, M. C., Kahn, S., & Sutherland, P. G. 1975, ApJ, 199, L147
Weisskopf, M. C., Sutherland, P. G., Katz, J. I. & Canizares, C. R. 1978, ApJ, 233, L17
Wheeler, J. C. 1977, ApJ, 214, 560
White, N. E. 1989, A&A Rev., 1, 85